CHALMERS
UNIVERSITY OF TECHNOLOGY

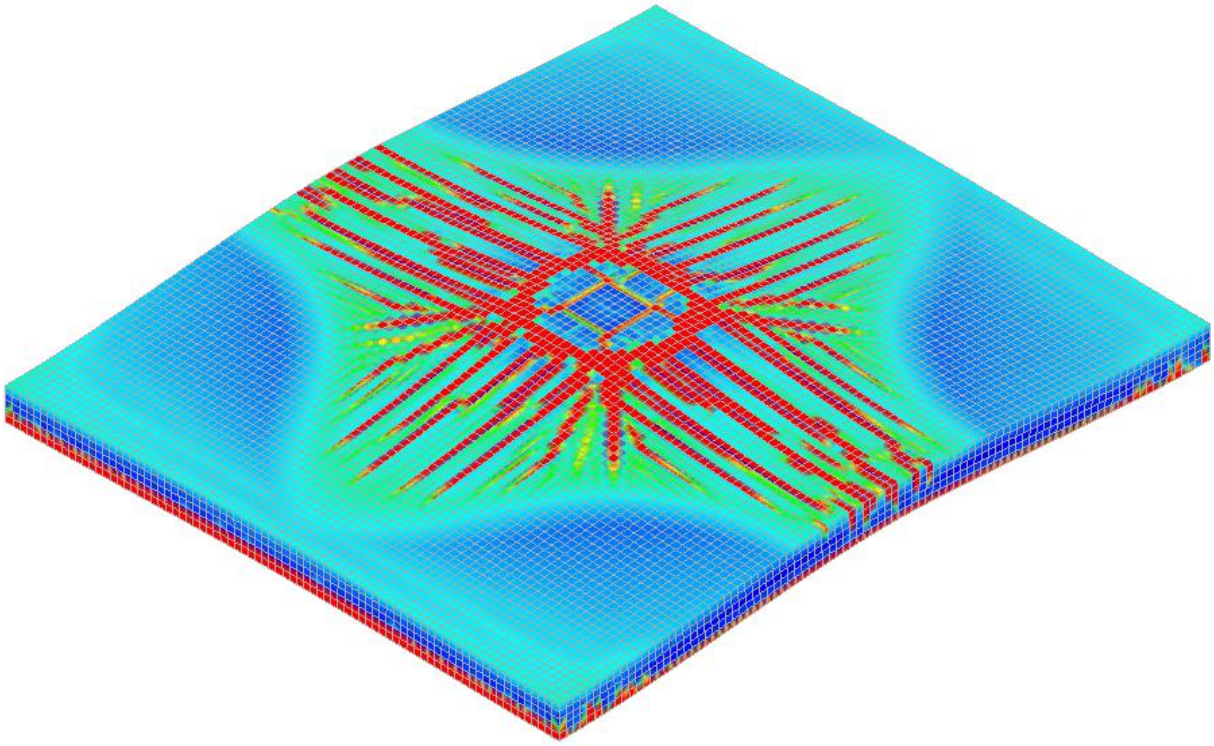

Structural Behaviour of Steel Fibre Concrete Floors

Master of Science Thesis in the Master's Programme Structural Engineering and Building Technology

AHMAD ARAFAT
AMIR KHORSANDI

Department of Civil and Environmental Engineering
Division of Structural Engineering
Concrete Structures
CHALMERS UNIVERSITY OF TECHNOLOGY
Gothenburg, Sweden 2019
Master's Thesis ACEX30-19-57

MASTER'S THESIS ACEX30-19-57

Structural Behaviour of Steel Fibre Concrete Floors

Master of Science Thesis in the Master's Programme Structural Engineering and Building Technology

AHMAD ARAFAT

AMIR KHORSANDI

Department of Civil and Environmental Engineering
Division of Structural Engineering
Concrete Structures
CHALMERS UNIVERSITY OF TECHNOLOGY
Gothenburg, Sweden 2019

Structural Behaviour of Steel Fibre Concrete Floors

Master of Science Thesis in the Master's Programme Structural Engineering and Building Technology

AHMAD ARAFAT

AMIR KHORSANDI

Supervisors: Ingemar Löfgren, Structural Engineering, Chalmers
David Fall, Structural Engineering, NCC
Examiner: Ingemar Löfgren, Structural Engineering, Chalmers

Technical report no. ACEX30-19-57
Department of Civil and Environmental Engineering
Division of Structural Engineering
Concrete Structures
Chalmers University of Technology
SE-41296 Gothenburg
Sweden
Telephone: +46 (0)31-772 1000

Cover: Three-dimensional view of the crack pattern in the studied pile supports slab under uniformly distributed load.

Chalmers Reproservice / Department of Civil and Environmental Engineering

Structural Behaviour of Steel Fibre Concrete Floors
Master of Science Thesis in the Master's Programme Structural Engineering and Building Technology
AHMAD ARAFAT, AMIR KHORSANDI
Department of Civil and Environmental Engineering
Division of Structural Engineering
Concrete Structures
Chalmers University of Technology

Abstract

Concrete as a heterogeneous material is a suitable choice for resisting high compressive stresses, whereas it exhibits a low resistance toward tensile stresses as well as a very brittle behaviour. Various alternatives have been introduced to enhance the tensile behaviour of concrete, such as conventional reinforced concrete and steel fibre reinforced concrete (SFRC). Steel fibre reinforced concrete benefits the construction process by reducing the labour effort that decreases the construction time and thus may be beneficial for the construction economical cost. Furthermore, several kinds of research have shown that SFRC enhances toughness and other properties of concrete, a fact that makes SFRC an attractive choice from a structural behaviour point of view. One of the promising applications of SFRC is for pile-supported slabs. Nevertheless, the use of SFRC is still limited, since various challenges shall be considered, such as cracking, which can be due to shrinkage, load and temperature.

Although there are several available codes for design of conventional and steel fibre reinforced concrete, and they are accurate for many structural elements, these codes are still incapable of determining the actual structural behaviour when the structural element has specific boundary conditions such as continuous slabs, since a significant discrepancy has been recognized between experimental results and proposed design methods. For instance, in continuous slabs, the difference could stem from factors such as arching action phenomenon. This phenomenon is dependent on the boundary conditions of the structure, whereas it is independent of the used material. In other words, the arching action phenomenon can arise from the presence of special boundary conditions, regardless of what the used material is. The effect of arching action is favourable, but meanwhile, including this effect in the design procedure could make it intricate. Therefore, this master's thesis has been directed toward investigating the structural behaviour of SFRC and how the boundary conditions could impact this behaviour. To carry out this investigation, a set of numerical analyses has been implemented. The first numerical analysis was for notched three-point bending beam, which has been used as a tool to verify the tensile response of SFRC. The second one is a numerical analysis of round indeterminate panel test, which is by the purpose of evaluating the influence of frictional contact zone on the structural behaviour of the round panel, where the frictional contact zone is between the round panel and its continuous support. The last one was a numerical analysis of a full-scale pile supported slab to investigate the impact of arching action phenomenon on its structural behaviour.

As expected, the use of SFRC increases the ductility of concrete and could result in hardening deflection. Additionally, the numerical analysis of the notched beam indicates that adaptive inverse analysis (AIA) is a good representative for the tensile response of SFRC. Moreover, the results of round indeterminate panel test exhibit that the friction forces between the round panel and its continuous support increase the post-cracking capacity and therefore, these forces will cause an overestimation in the evaluation of post-cracking capacity. Finally, the numerical analysis of pile supports slab displays that arching action phenomenon increases the capacity of an interior panel while it is subjected to uniformly distributed load or point load. The effect of arching action is favourable and could be utilized to perform a more economic design.

Keywords: Steel fibre reinforced concrete (SFRC), Non-linear finite element analysis, DIANA, Arching action phenomenon, Inverse analysis, Post-cracking behaviour of SFRC, Frictional contact zone, Crack pattern

Preface

This project aims to investigate the structural behaviour and failure mechanism in a pile-supported slab using 3D non-linear finite element analysis. The project was carried out at the division of Structural Engineering at Chalmers University of Technology in collaboration with Thomas Concrete Group and NCC.
The non-linear finite element analyses were performed on resources at Chalmers Centre for Computational Science and Engineering (C3SE) provided by the Swedish National Infrastructure for Computing (SNIC).

The Report includes capacity and crack evaluation of pile-supported floors made by steel fibre reinforced concrete (SFRC) to have a better understanding of SFRC pile-supported floors. Additionally, it assesses the effect of the friction coefficient on the structural behaviour of a round panel test.

This master's thesis was performed, between January 2019 and June 2019, at the Department of Structural engineering and building technology, Chalmers University of Technology, Göteborg, Sweden.

We would like to have our special thank for our examiner and supervisor PhD Ingemar Löfgren and supervisor PhD David Fall, at NCC, for their continuous support and guidance throughout the entire project period. We are also grateful to postdoc Carlos Gil Berrocal and PhD student Mattias Blomfors for their kind supports and feedbacks.

Finally, this master's thesis is dedicated to Björn Engström's soul, the professor who has taught us the meaning of structural engineering.

Ahmad Arafat and Amir Khorsandi, Gothenburg, June 2019

Contents

List of Figures

List of Tables

Notations

Upper case letters

$CMOD_j$	Crack mouth opening displacement at stage j
F_j	Load corresponding to $CMOD = CMOD_j$
E_c	Modulus of elasticity
E_{fcm}	Mean secant modulus of elasticity
W_E	External work
W_l	Internal work
$P_{ult.RP}$	Ultimate point load in case of round panel
$M_{p,RP}$	Moment capacity of round panel
R	Radius of round panel
M_{el}	Elastic moment capacity
L_{sp}	Span length
$M^-_{Py1,SD}$	Negative and positive moment capacity in y-direction in case of slab under uniformly distributed load
$M^+_{Py,SD}$	Positive moment capacity in y-direction in case of slab under uniformly distributed load
L_{rx}	Span length in x-direction
$M^-_{Px,SD}$	Negative and positive moment capacity in x-direction in case of slab under uniformly distributed load
$M^+_{Px,SD}$	Positive moment capacity in x-direction in case of slab under uniformly distributed load
L_{rx}	Span length in y-direction
$M^-_{P,SP}$	Negative and positive moment capacity in case of slab under point load
$M^+_{P,SP}$	Positive and positive moment capacity in case of slab under point load
R_{SP}	Radius of fan pattern
$P_{ult,SP}$	Ultimate point load in case of slab under point load
K_0	Tangential stiffness matrix

A_{el}	Area of one element
V_{el}	Volume of one element

Lower case letters

h_{sp}	Distance from the tip of the notch to the top of the beam
l	Length of beam
b	Width of beam
$f_{R,j}$	Tensile flexural strength corresponding to $F = F_j$
a	Height of notch
f_{FTu}	Ultimate post-cracking strength
f_{FTs}	Post-cracking strength for the serviceability limit state
f_{R1}	Flexural tensile stress corresponding to $CMOD_1 = 0.5$ mm
f_{R2}	Flexural tensile stress corresponding to $CMOD_2 = 1.5$ mm
f_{R3}	Flexural tensile stress corresponding to $CMOD_3 = 2.5$ mm
f_{R4}	Flexural tensile stress corresponding to $CMOD_3 = 3.5$ mm
w_u	Maximum crack width
w_{cmod}	Crack mouth opening
w_{cod}	Crack opening displacement
f_{fck}	Characteristic cylinder compressive strength
$f_{fctm,fl}$	Mean flexural tensile strength
$f_{fctk,fl}$	Characteristic flexural tensile strength
d	Effective depth or thickness of structural element
a	Radius of loading plate that acts on round panel
q	Uniformly distributed load
$x_{0,SD}$	Segment length

$q_{ult,SD}$	Ultimate distributed load
a_{SP}	Radius of loading plate that acts on slab
u_0	Initial displacement
$x_{0,i}$	Initial estimation
r_i	True root
h_i	Number measures how far the initial estimation is from the truth
$x_{1,i}$	First improved estimation
$x_{2,i}$	Second improved estimation
l_{cs}	Structural characteristic length

Greek letters

σ_i	Stress at stage i
ε_i	Strain at stage i
κ_h	Size factor
δ	Deflection in case or round panel
θ	Rotation in case of round panel
$\alpha_{m.c}$	Moment coefficient
δ_{SD}	Deflection in case of slab under uniformly distributed load
$\theta_{1,SD}$	Rotation of segment one in case of slab under uniformly distributed load
θ_{SP}	Rotation in case of slab under point load
ε_c	Strain at maximum stress

Abbreviations

FRC	Fibre Reinforced Concrete
SFRC	Steel Fibre Reinforced Concrete
FE	Finite element
FEA	Finite element analysis
UUT	Uniaxial tensile test
3PBT	Three-point Bending Test
4PBT	Four-point Bending Test
WST	Wedge-splitting Test
LOP	Limit of proportionality
CMOD	Crack Mouth Opening Displacement
AIA	Adaptive inverse analysis
ULS	Ultimate limit state
SLS	Serviceability limit state
YLT	Yield line theory
BFGS	Broyden-Fletcher-Goldfarb-Shanno
DOF's	Degrees of freedom
2D	Two-dimensional
3D	Three-dimensional

1 Introduction

1.1 Background

There are different structural materials available for relevant purposes such as concrete, steel, timber etc. Among all materials that are suitable for structural purposes, concrete and steel have the widest use. Steel has the same capacity in tension and compression, but for concrete, this is not the case as the tensile capacity is significantly lower than the compressive one. Furthermore, concrete is a brittle material, and thus, most structural elements need to become more ductile by use in combination with different additional materials. Several methods have been proposed and used to improve properties of concrete such as adding conventional reinforcement to the concrete, as well as fibre reinforced concrete (FRC) that are used to enhance the tensile properties of concrete and its ductility.

Considering fibre reinforced concrete, the fibres can be organic fibres, carbon fibres, polymeric fibres as well as steel fibres. The real use of steel fibre reinforced concrete (SFRC) started five decades ago (from 1960) and is now mostly used for industrial floors and sprayed concrete linings. SFRC has the advantage of high ductility in comparison to plane concrete, which arises from two different mechanisms. The first one is known as "micro-cracks arrest mechanism" and the second one is "crack bridging mechanism" (Oikonomou-Mpegetis, 2013). In the former mechanism, steel fibres suppress micro-cracks propagation to macro-cracks. On the other hand, in the latter mechanism, steel fibres act as stress bridges, which resist the additional crack opening, i.e. the tensile failure will be postponed (Oikonomou-Mpegetis, 2013).

Additionally, SFRC may be more economical due to that it is less time-consuming in comparison to concrete with conventional reinforcement as it decreases the need for labour. Another advantage, which makes it more attractive is that SFRC is highly suitable for special architectural models since it can be cast by any shape, either simple or complex. In other words, the architectural freedom can be increased, using SFRC (Fall, 2014). Based on all the advantages that have been described above, this material seems to be a good fit for pile-supported slabs, but on the other hand, a lot of challenges remain controlled such as cracking due to shrinkage, load and temperature. In addition, the effect on the material properties, which is significantly dependent on fibre content, distribution and orientation have to be considered. Although there are several design codes available for SFRC such as: fib model code 2010 (fib, 2013); RILEM design guideline (RILEM-TC-162-TDF, 2003); Danish design guideline (Kasper, et al., 2014); German design code (DBV, 2001) and Spanish design code (EHE-08, 2008), in case of SFRC without conventional reinforcement, some limitations are applied by those available codes, which decreases the use of SFRC to an extent.

Furthermore, these mentioned codes are remarkably conservative for evaluation of the post-cracking capacity for both SFRC and conventional reinforced concrete. This conservativity arises mainly from ignoring the arching action effect, which indeed results in higher load capacity for both SFRC and reinforced concrete structures. Arching action is a boundary condition dependent phenomenon that will be involved when a restraining exists, but by including the effect of it in the design guidelines, the guidelines will be more sophisticated, i.e. in order to keep the calculation simplicity, available design guidelines ignored the effect of arching action. This thesis is examining the influence of arching action and compare finite element analysis with current simplified methods to give a better understanding of SFRC.

1.2 Aim

The main outcome of this master thesis was to enrich the knowledge about SFRC pile supported slab by:

- Evaluating the post-cracking capacity as well as examination of failure mechanisms for a round indeterminate panel and a pile-supported slab.
- Investigating the effect of arching action phenomenon in a pile-supported slab.
- Assessing design methods of SFRC structures, as well as a more realistic understanding of previously designed or built structures.

On the other hand, for testing SFRC, a decisive factor that needs to be considered is the friction coefficient, which plays a significant role in the evaluation of the post-cracking capacity. Therefore, the effect of different friction coefficients on the structural behaviour of a round indeterminate panel was investigated.

1.3 Limitations

Although it has been attempted to cover several aspects, which are related to SFRC floors, few factors that have not been considered, such as:

- Effect of shrinkage and temperature, such as additional stresses and cracking.
- Long-term effects, such as creep.
- Resistance to abrasion.
- Effect of fibre orientation.
- Effect of fibres on compressive behaviour of SFRC.
- Safety-related issues with respect to design (i.e. characteristic material properties and safety factors for materials and loads).

Furthermore, all the calculations and analyses were for a specific slab as well as a specific SFRC mix without conventional reinforcement.

1.4 Methodology

In the beginning of this master thesis, two major phases of literature studies were performed, an initial phase for several aspects that are related to mechanical properties of SFRC as well as a second phase that considers the behaviour of SFRC round panel test as well as SFRC slabs. The initial phase of the literature study consists of basic knowledge about SFRC, including fibre classification as well as the effect of steel fibres. Moreover, a description of some related test methods has been covered in the literature study. Thereafter, the flexural, tensile and compressive response of SFRC have been reviewed and, additionally, several approaches for determining the tensile behaviour of SFRC have been reviewed. In the second phase of the literature study, the potential effect of friction coefficient on flexural behaviour of the round panel test as well as the related failure mechanism were examined. Afterwards, failure mechanisms of the pile-supported slab and the phenomenon of ‘‘arcing action’’ were reviewed. This work was continued with numerical non-linear analyses of notched three-point bending beam test, round panel test as well as pile-supported slab, using the multi-purpose finite element (FE) software, DIANA. The numerical analysis of notched three-point bending beam test was executed to verify the material constitutive tensile model, which was based on the adaptive inverse analysis approach. Afterwards, the numerical analysis of round panel was

implemented considering a frictional contact zone with different friction coefficients between the round panel and its continuous support as well as a frictionless contact zone. This numerical analysis has been directed toward investigating the structural behaviour and the crack pattern of the round panel. Moreover, different approaches for implementation of the round panel model in the FE software DIANA were investigated and compared. At the last stage, a three-dimensional model of a pile-supported slab was analysed to investigate the effect of arcing action phenomenon on the structural behaviour of SFRC pile-supported slab. Additionally, the crack pattern as well as the failure mechanism were investigated.
At the end, results of finite element analysis (FEA) were compared with results from hand calculation according to fib model code 2010.

2 Literature review

2.1 General

Concrete itself is a heterogeneous material with high compressive strength, but low tensile strength as well as low ductility, i.e. it is a very brittle material. Concrete is mainly composed of hardened cement paste and aggregate. The weakness of concrete in tension springs form the fact that the interfacial transition zone around the aggregates could be weak. Since voids and some microcracks can pre-exist in the interfacial transition zone, the stress cannot transfer through the thickness effectively. This results in low energy dissipation in tension, thus low tensile load carrying capacity. There are several methods to overcome this problem, such as using conventional reinforcement, which is the most common way. Another historical method, which has been further developed in new designs, is to introduce fibres in the concrete mixture. In ancient times different types of natural fibres such as horsehair were used to enhance the integrity of the structure and reduce brittleness. Nowadays, different types of fibres such as steel, synthetics, glass, natural fibres etc. are common to use for this purpose (Abid & Franzén, 2011). The presence of fibres will not significantly affect the tensile strength of concrete, whereas it increases the ductility (more energy dissipation) substantially. As the fibres are randomly distributed, it makes them effective in controlling the cracks (Abid & Franzén, 2011). There are also some other advantages such as enhancing the durability of concrete, decrease bleeding in fresh concrete and reduce the air voids as well as water voids. Due to all advantages that mentioned before, this composite material has a wide use nowadays for different applications such as, aircraft runways and parking, pavements, industrial flooring, tunnel and canal linings, slope stabilization, thin shells and pipes (Kaur & Talwar, 2017).

2.2 Fibre classification

Fibre as a material, which is used in cementitious composite materials, varies in its physical, mechanical, and geometric properties. Therefore, it has been classified by (Naaman, 2003) based on several classification criteria, as presented in Table 2.1.

***Table 2.1**: Classification of fibres based on several criteria*

Classification criteria	Related properties (Naaman, 2003)
Physical properties	Density and surface roughness.
Origin of fibres	Natural organic, natural inorganic and man-made.
Mechanical properties	Specific gravity, tensile strength, Modulus of elasticity, ductility, stiffness and elongation to the failure.
Geometric properties	Diameter, length, cross sectional shape such as circular, rectangular, diamond, triangular, square, flat or polygonal. (Figure 2.1 and Figure 2.2).
Chemical properties	Reactivity or non-reactivity with cementitious paste, flammability.

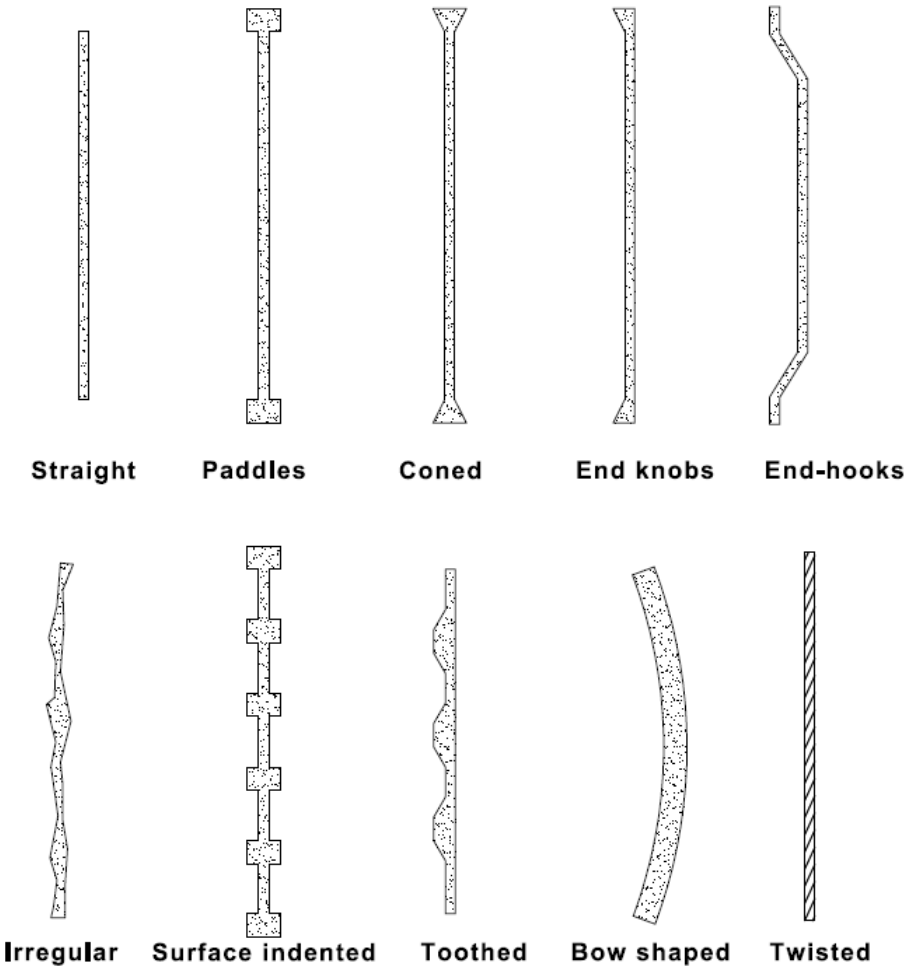

Figure 2.1: *Common fibre geometries. Recreated from (Löfgren, 2005)*

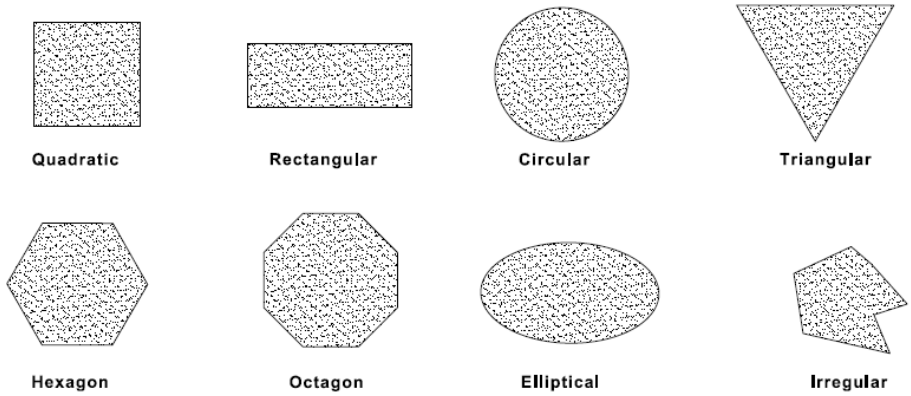

Figure 2.2: *Cross-sectional geometries of fibres. Recreated from (Löfgren, 2005)*

Since the aim of using any kind of fibre material is to strengthen the cementitious composite material, the metallic fibres have mainly been used. Steel fibres were the best choice in many applications since steel has high tensile strength in comparison to other materials. Hence, several scientific societies and standardisation organizations have aimed to classify and characterize the steel fibres. As an example, (EN 14889-1, 2006) has classified steel fibres based on used material for production (Table 2.2), whereas (EN 14889-2, 2006) has characterized steel fibres based on their aim of use (Table 2.3).

Table 2.2: *Classification of fibres based on the used material for production, (Löfgren, 2005), (EN 14889-1, 2006)*

Classification Group	Material of production
Group I	Cold-drown wire
Group II	Cut sheet
Group III	Melt extracted
Group IV	Shaved cold drawn wire
Group V	Milled from blocks

Table 2.3: *Classification of fibres based on the aim of use, (Löfgren, 2005), (EN 14889-2, 2006)*

Classification Group	Aim of use
Group I	Enhance the short-term plastic properties, control plastic shrinkage, reduce bleeding.
Group II	Enhance the durability, enhance the abrasion resistance, reduce the damage of freezing and thawing
Group III	Increase the residual strength.
Group IV	Enhance the fire resistance.

2.3 Steel fibres

The most commonly used fibres are steel, which have higher slenderness as well as more complex geometries (Löfgren, 2005). Although there are several geometries available for steel fibres, the most common are round fibres with a diameter range of 0.25 mm to 0.75 mm. The tensile strength of fibres alone is in range of 200-2600 MPa (Jansson, 2008), and the ultimate elongation varies between 0.5 and 5 per cent. It should be noticed that fibres with high yield capacity may have an adverse effect on reinforcing by causing spalling around the fibre exit point. Therefore, fibres with sufficient yield capacity shall be chosen properly to avoid fibre rupture (Jansson, 2008). All mentioned properties result in enhanced structural behaviour such as higher ductility (more energy dissipation) as well as crack resistance. SFRC can be made with different proportions (typically expressed as a volume fraction) of steel in concrete depending on the purpose of the material, which defines the required workability, strength etc. In SFRC the cement content as well as the fine to coarse aggregate ratio are usually higher than

in ordinary concrete, which means that mix compositions of ordinary concrete may not be valid for SFRC. Regarding the shape of fibres, straight fibres are not common, since they have weak bonding with concrete. But, brass-coated straight fibres, which have relatively strong bonding, are more common in some high-performance concretes (Kaur & Talwar, 2017). A concern regarding steel fibres is that they are susceptible to corrosion, which may result in lowered strength. However, experiments and studies have found that rust is mainly on/close to the surface of the concrete (Kaur & Talwar, 2017). Furthermore, the rust, which is close to the surface of concrete may weaken the fibres at mentioned location, but since the amount of fibres close to surface are not comparable with the total amount of fibres, the effect of corrosion on the total strength can be neglected, i.e. there is no effect on long-term strength (Berrocal, 2017).

2.4 Test methods

2.4.1 General

There are several test methods to assess the tensile behaviour of SFRC. One of them is a direct test method, which is the uniaxial tensile test (UUT) and the others are indirect test methods such as notched three-point bending test (3PBT), four-point bending test (4PBT), Japanese beam test, round determinate panel test (ASTM 1550), wedge-splitting test (WST), etc. Direct test method means that the tensile response can be determined directly from the test results, whereas indirect test method means that the test results must be transformed and interpreted to determine the tensile response. For instance, 3PBT determines the flexural behaviour of SFRC, which needs to be transformed into the constitutive law. Several approaches have been proposed to determine the tensile response of SFRC, which are depicted in 2.5.3. Considering 3PBT and 4PBT, the difference is that in 3PBT there is only one point-load acting on the beam with a notch in the middle (Figure 2.3), whereas in 4PBT there are two point-loads without a notch (Figure 2.4). The effect of the mentioned notch is that it forces the beam to fail at a specific location, i.e. the notch acts as a stress raiser and initiates the first crack only over the notch.

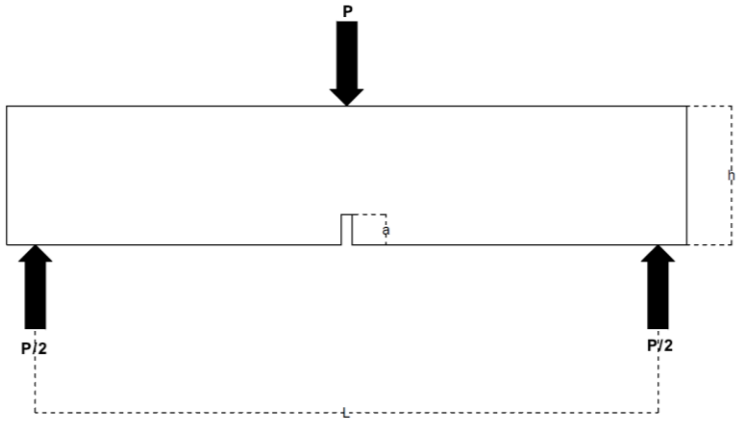

Figure 2.3: *Three-point bending test*

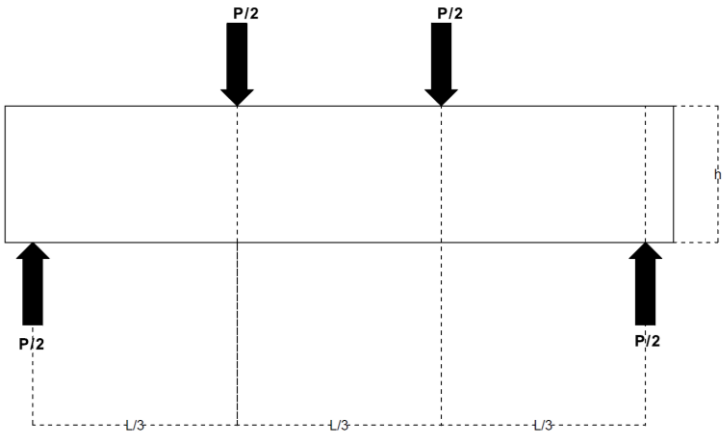

Figure 2.4: *Four-point bending test*

2.4.2 Notched three-point bending test

3PBT is an indirect test, and it measures the crack mouth opening displacement during the test. The main aim of 3PBT is to measure the limit of proportionality (LOP), which is the maximum flexural tensile stress where the so-called "crack mouth opening displacement (CMOD)" is in the range of 0 to 0.05 mm, as well as a set of residual flexural tensile strength values. The following residual flexural tensile stresses can be expressed as stated below:

$$f_{R,j} = \frac{3\,F_j\,l}{2\,b\,h_{sp}^2} \qquad (2.4.1)$$

Where F_j can be the load corresponding to $CMOD = CMOD_j$ (Figure 2.5), h_{sp} is the distance from the tip of the notch to the top of the beam, l is the length of beam and b is the width of the beam.

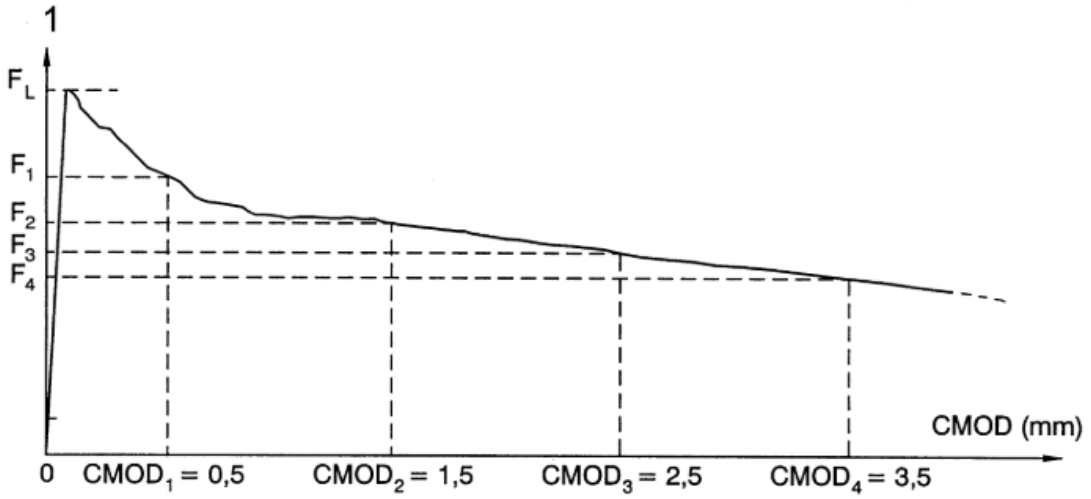

Figure 2.5: *Load vs. CMOD according to (EN 14651, 2005).*

Moreover, to perform 3PBT according to (EN 14651, 2005), the cross-sectional dimensions are specified to be 550 mm in length, 150 mm in width and 150 mm in height. Considering the notch, the width shall be 5 mm or less, and the height shall be 25 mm with a tolerance of 1 mm.

2.4.3 Round determinate panel test

Round determinate panel test (ASTM C 1550) is an indirect test, and it measures the load and deflection at the centre during the test. This test is a round panel with a thickness of 75 mm and a diameter of 800 mm and supported by three pivots (ASTM C1550-12a, 2012). These pivots are symmetrically arranged at 375 mm radius (ASTM C1550-12a, 2012). Additionally, the round panel is subjected to point load, which acts in the centre. The configuration of this test can be seen in Figure 2.6 and Figure 2.7. Moreover, it has been seen that the arrangement of the three pivots results in consistent failure mode, which leads to low batch variability, whereas this low batch variability cannot be achieved in 3PBT (ASTM C1550-12a, 2012). On the other hand, the effect of arching action arises in this test, where at the beginning, the load resistance is due to flexural resistance. But, when the deflection increases, the effect of arching action starts arising, which leads to a change in the load resistance mechanism (Oikonomou-Mpegetis, 2013).

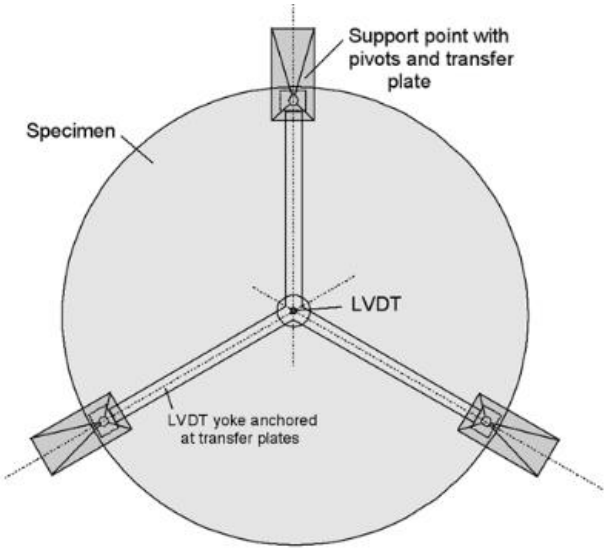

Figure 2.6: *Plan view of round determinate panel test (ASTM C 1550), (ASTM C1550-12a, 2012)*

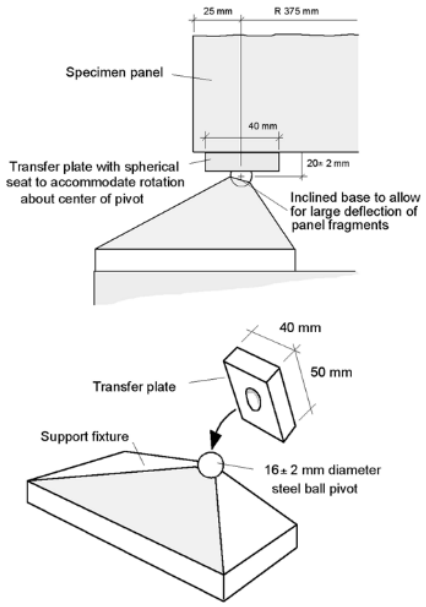

Figure 2.7: *Detail of the pivoted point supports, (ASTM C1550-12a, 2012)*

2.5 Material response

2.5.1 Flexural behaviour of SFRC

As mentioned before, the overwhelming majority of tests for SFRC are flexural tests, which are used to determine the tensile properties of SFRC. Therefore, the flexural behaviour of SFRC shall be investigated. The flexural response of concrete in the presence of fibre is highly affected in comparison to its tensile and compressive behaviours. Since the fibres have a high contribution to the flexural response of concrete, it can be concluded that fracture energy is also highly affected by the fibres, as shown in Figure 4.3.
The main reason behind this substantial impact of fibres is that as the load increases the tensile stress will increase as well until reaching its maximum value (in the outermost layer on tension side), which is the ultimate tensile strength. In this stage, which is named as "phase one" as illustrated in Figure 2.8, the concrete is still un-cracked. After this stage, the first crack (a micro-crack) will start to develop. Thereafter, the load goes toward the fibres, where a much more ductile behaviour is expected. Obviously, after the micro-cracks appear on the concrete, the neutral axis will be slightly shifted upward, and the micro-cracks will be bridged by a combination of steel fibres and aggregate interlocks (phase two). Phase two will be followed by crack propagation in the upward direction (phase three), through the concrete cross-section that results in bridging the cracks by steel fibres, which induces high stresses at the matrix-fibre interface. At the final stage (phase four), either fibre pull out or fibre fracture can lead to failure in steel fibre reinforced concrete, which cause a ductile or brittle failure respectively (Oikonomou-Mpegetis, 2013).

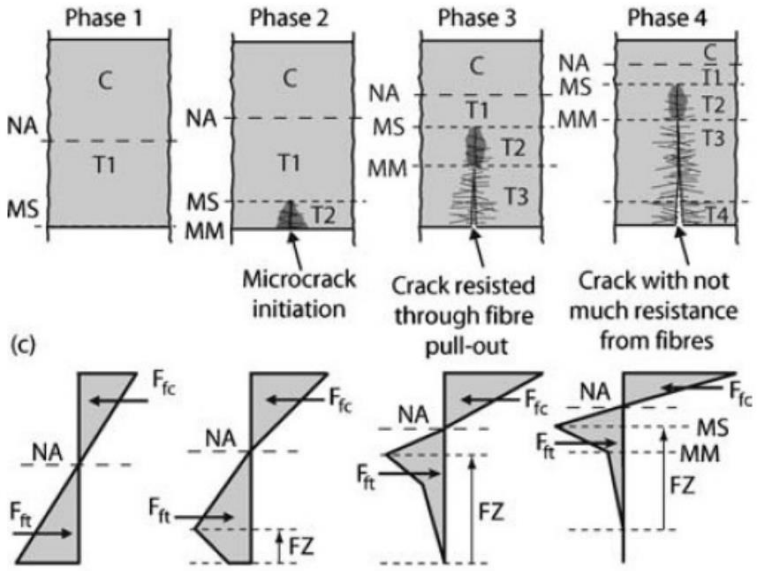

Figure 2.8: *Different stages of cracking in SFRC under bending, (Tlemat, et al., 2006)*

2.5.2 SFRC constitutive models

As described before, the main aim of using steel fibres in concrete is to increase the ductility in comparison to plain concrete by resisting crack propagation. This crack resistance arises from two mechanisms, which are the micro-cracks arrest mechanism as well as crack bridging mechanism. The former deals with micro-cracks by not letting them coalesce and propagate to macro cracks, which eventually leads to failure. The latter, however, deals with macro cracks by bridging them across the crack plane. The mentioned mechanisms impact mainly the tensile and flexural behaviour of concrete, whereas the effect on compressive behaviour is much smaller and can be neglected. Therefore, many studies have been directed toward proposing a constitutive model that can describe mainly the tensile and flexural behaviour of SFRC. One of those researches is (Maalej, et al., 1995), which proposed theoretical expressions to describe the flexural behaviour of SFRC based on the ratio of flexural to tensile strength as well as the geometry of the specimen. Standards such as (RILEM-TC-162-TDF, 2003) have been proposed with the aim of predicting the tensile behaviour of SFRC from 3PBT and how the tensile behaviour can be used for design in bending and shear. In the following sections, several constitutive models are present to describe the behaviour of SFRC.

2.5.2.1 Compressive model

As mentioned, the impact of steel fibres on compressive behaviour of concrete is much smaller than on tensile behaviour. However, to understand the impact of steel fibres, the behaviour of concrete shall be explained. It was observed that cracks due to compression, form as sliding in the interfacial transition zone, which is weak due to the presence of voids and microcracks. This sliding results in the formation of tensile cracks that propagate into the concrete simultaneously. By increasing the compressive load, the tensile cracks grow more. At the end, concrete crushing (failure) arises from the interaction of tensile cracks (Löfgren, 2005). In case of SFRC, tensile cracks due to compression are resisted more (Löfgren, 2005), and the compressive behaviour is more ductile (more energy dissipation) (Oikonomou-Mpegetis, 2013). On the other hand, another impact from steel fibres on the elastic modulus of concrete

has been observed, which can be explained in the way that the presence of steel fibres results in a slight reduction in modulus of elasticity (Oikonomou-Mpegetis, 2013). The reason behind this reduction springs from the fact of that larger number of small voids will be introduced due to the presence of steel fibres (Neves & Fernandes de Almeida, 2005). Although several empirical constitutive models have been proposed to represent the compressive behaviour of SFRC (Lee, et al., 2015), several research papers showed that the impact of steel fibres can be negligible if the steel fibres dosage is less than 1 %, i.e. concrete has normal compressive strength (Löfgren, 2005). Figure 2.9 shows the impact of steel fibres on the compressive behaviour of concrete.

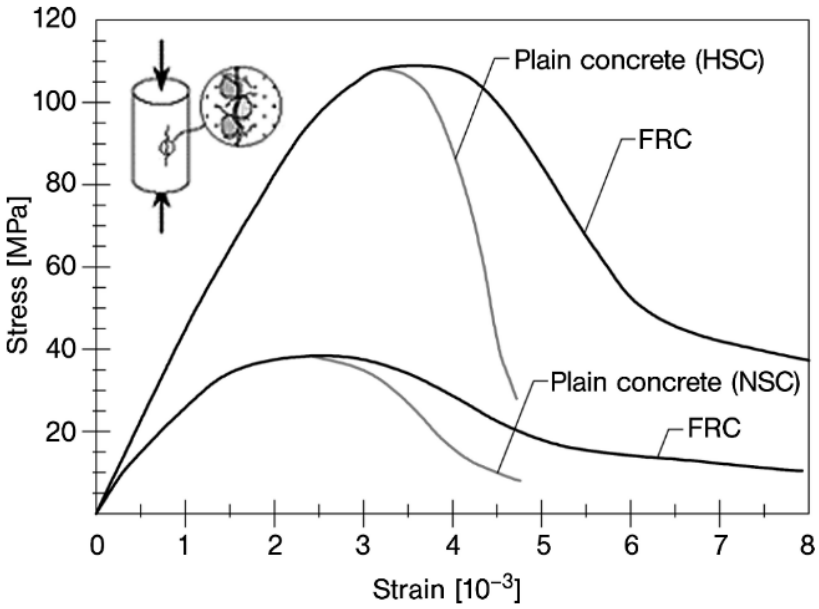

Figure 2.9: *Schematic compressive behaviour of FRC and concrete, (fib, 2013)*

2.5.2.2 Tensile model

Concrete as a brittle material is not intended to carry tensile stresses since it has low tensile capacity. This low tensile capacity springs from the fact that the interfacial transition zones around the aggregates are weak, hence they are highly prone to crack under tensile stresses. Therefore, when the stress in concrete reaches the tensile strength, concrete fails immediately with a negligible ductility. On the other hand, SFRC displays an ability to dissipate more energy after reaching the tensile strength, which results in a ductile behaviour.
The cause behind this ductile behaviour is that after cracking, the steel fibres start dissipating energy instead of the concrete and they carry the tensile stresses. Hence, the steel fibres, which are intersecting the cracks, start preventing the crack opening by two mechanisms, crack arrest and crack bridging mechanisms. The tensile response can be characterised by three phases (Oikonomou-Mpegetis, 2013). The first phase is the elastic phase, which represents the state before crack initiation. In this phase, both elastic modulus and the ultimate tensile strength determine the tensile response. The second phase is the micro-cracking phase, which represents the state of crack initiation. In this second phase, there are two different potential responses of SFRC, which are the so-called ‘‘tension softening response’’ and ‘‘strain hardening response’’. The former represents the case in which fibres are not capable of resisting additional stresses after the initial cracking, which results in a response dominated by a single crack (Figure 2.10).

Contrarily, in the latter response, the fibres resist the additional stresses, and multiple cracks form as illustrated in Figure 2.10. The final phase is the fibre pull-out (macro-cracking), which represents the state that fibres start being pulled-out from the concrete matrix. In this final phase, two responses can be observed; the so-called ‘‘ductile response’’ and ‘‘brittle response’’. The ductile response represents the case that the fibres become pulled-out progressively, whereas, the latter represents the case that the fibres are fractured under tensile stresses, which leads to brittle failure. The micro-cracking and fibre pull-out phases, represent the post-cracking response, can be affected by several factors such as fibre dosage, physical and chemical properties of fibre, fibre type and bond stresses.

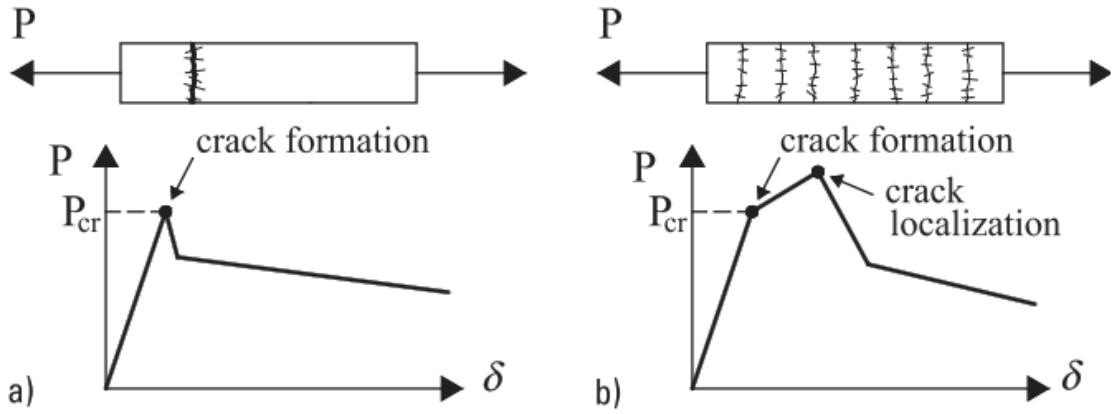

Figure 2.10: *Tensile response of SFRC: Tension softening response (a) and tension hardening response (b), (Di Prisco, et al., 2013)*

2.5.3 Approaches for determining the constitutive model of SFRC tensile response

2.5.3.1 General

For determining the constitutive model of SFRC tensile response, experimental data is required in almost all approaches. The type of required experimental data is dependent on the followed approach. Uniaxial tensile test (UUT) is the best direct representative of SFRC tensile response, but one of its disadvantages is that it is highly dependent on the fibre orientation, which makes it, to some extent, inaccurate if the fibre orientation has not been taken into account during the casting of concrete. Another disadvantage is that UTT is more expensive and more technical demanding than other tests. Therefore, the flexural test of beams has become the most common test for investigating the tensile behaviour of SFRC due to its ease of implementation. Three-point bending test (3PBT) is a test to determine the flexural tensile behaviour of SFRC, which can be used to derive its tensile behaviour by use of various inverse analysis approaches. However, some of these approaches are based on empirical equations such as Fib model code 2010 and σ-ε-design method, whereas the others are based on iterative methods such as adaptive inverse analysis approach (AIA).

2.5.3.2 Fictitious crack model

The proposed fictitious crack model by (Hillerborg, et al., 1976) considers that the propagation of any crack initiates when the stress of the crack tip reaches the tensile strength. After reaching the tensile strength, stress must not drop to zero immediately, but by a descending function.

Hence, the tension softening behaviour of concrete is modelled in terms of crack width. As illustrated in Figure 2.11, aggregate interlock as well as process zones represent the fictitious crack, which reflects the real behaviour of concrete. The main aim of the fictitious crack model is to display the tensile behaviour of concrete within the fracture zone. Therefore, the stress is related to crack opening displacement within the fracture zone, whereas it is related to elastic strain in the uncracked zone.

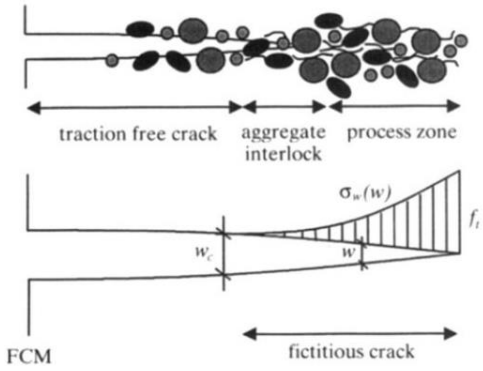

Figure 2.11: *Anatomy of a crack propagating through plain concrete, (RILEM-TC-162-TDF, 2002)*

On the other hand, in case of SFRC, two mechanisms can arise, crack arrest and crack bridging. Hence, the same concept was modified by (Hillerborg, 1980) to fit the behaviour of SFRC and that has been attained by considering the mentioned mechanisms as shown in Figure 2.12.

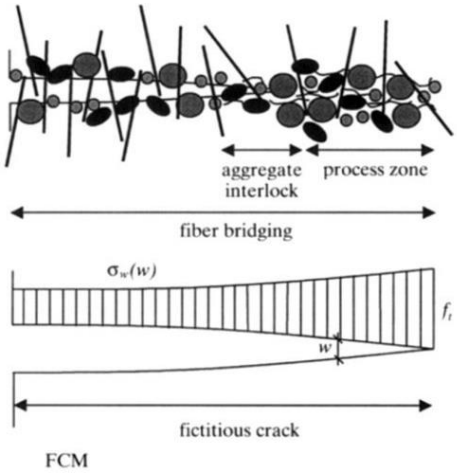

Figure 2.12: *Anatomy of a crack propagating through SFRC, (RILEM-TC-162-TDF, 2002)*

2.5.3.3 Fib model code 2010

The proposed constitutive model by (fib, 2013) is commonly used since it is simple and easy to be implemented. This constitutive model is based on the concept of the fictitious crack model, and it needs experimental data from the notched 3PBT. According to (fib, 2013), two simplified tensile constitutive models can be used, the rigid-plastic model as well as the linear model, which are represented in Figure 2.13.

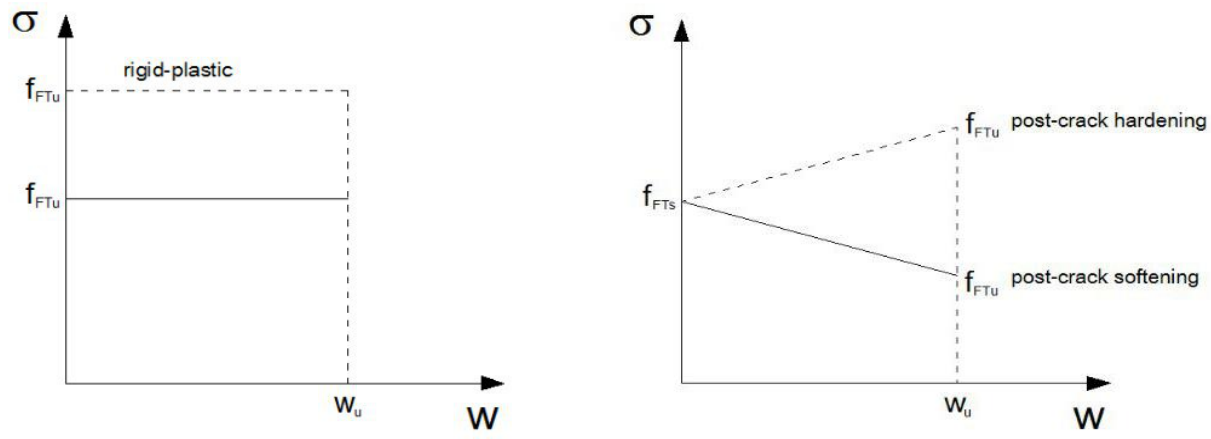

Figure 2.13: *Rigid-plastic (Left) and Linear (Right) constitutive models, (fib, 2013)*

In the rigid-plastic model, reference stress shall be defined, which can be considered as ultimate post-cracking strength. This reference stress is based on flexural tensile stress when the crack mouth opening width displacement (CMOD) is 2.5 mm. The ultimate post-cracking strength and the flexural tensile stress are obtained as follows:

$$f_{R,j} = \frac{3\,F_j\,l}{2\,b\,h_{sp}^2} \qquad (2.5.1)$$

$$h_{sp} = h - a \qquad (2.5.2)$$

Where, h is the height of beam, a is the height of notch, l is the length of beam, b is the width of beam and F_j is the load corresponding to $CMOD = CMOD_j$.

$$f_{FTu} = \frac{f_{R3}}{3} \qquad (2.5.3)$$

Where, f_{FTu} is the ultimate post-cracking strength.

Contrarily, in the linear post-cracking model, two reference stresses shall be defined. One of them (f_{FTs}) represents the post-cracking strength for the serviceability limit state, whereas the other (f_{FTu}) represents the post-cracking strength for the ultimate limit state. These two references can be defined as follows:

$$f_{FTs} = 0.45 f_{R1} \qquad (2.5.4)$$

$$f_{FTu} = f_{FTs} - \frac{w_u}{CMOD_3}\,(f_{FTs} - 0.5 f_{R3} + 0.2 f_{R1}) \qquad (2.5.5)$$

Where, f_{R1} and f_{R3} represents the flexural tensile stress corresponding to $CMOD_1 = 0.5$ mm and $CMOD_3 = 2.5$ mm, respectively and w_u is the maximum crack width.

In addition, to calculate the moment capacity, the following equation can be applied:

$$M_u = \frac{f_{FTu}\, b\, h^2}{2} \qquad (2.5.6)$$

According to (fib, 2013), w_u depends on the ductility and shall be less than 2.5 mm. Moreover, (fib, 2013) proposes more advanced constitutive models for numerical analysis.

2.5.3.4 Inverse analysis approach

Since SFRC is a complex material, and several factors can impact its behaviour, the tensile constitutive model cannot be determined accurately by means of empirical equations. Furthermore, the use of empirical constitutive models such as fib model code and σ-ε design method for FEA displayed some dissimilarities between the FEA results with experimental results. For instance, fib model code 2010 showed incapability of determining the post-cracking capacity in comparison with FEA and experimental capacities (Fall, et al., 2012). Additionally, fib model code 2010 displayed inaccurate capacities when the fibre content increases (Fall, et al., 2012). One reason behind these dissimilarities is that all the empirical constitutive models are either simple linear or bi-linear, which can be considered as a simplification of the real tensile behaviour of SFRC. Hence, several research papers such as (Stephen, et al., 2019) and (Østergaard, 2003) have been directed toward finding a numerical approach that can determine the tensile behaviour of SFRC. All these numerical approaches are iteration-based approaches and for determining a tensile behaviour that fits the experimental results by an inverse analysis approach. However, to attain a precise tensile constitutive model, a simple linear or bi-linear model is insufficient; thus, the multi-linearity is necessary to be applied. Therefore, the so-called ‘‘adaptive inverse analysis (AIA) method’’ was developed by (Jepsen, et al., 2018). This method is based on the fictitious crack model concept and can be considered as a powerful tool to determine the tensile behaviour of SFRC, since it generates a multi-linear tensile constitutive model. It is beneficial to mention that this method is verified on several fibre reinforced concrete composites as well as the studied SFRC mix. The mentioned method is based on non-linear least-square curve fitting process, which has been established by (Jepsen, et al., 2016) then it has been enhanced by coupling the model error to the crack mouth opening as well as the crack opening displacement relationship ($w_{cmod} - w_{cod}$). Moreover, the AIA (Jepsen, et al., 2018) has an enhancement in the curve fitting process, which results in improving the convergence rate.

2.5.3.5 σ-ε-design method

Another tensile constitutive model of SFRC is the stress-strain method, which is, to some extent, similar to stress-crack width approaches, but the crack width has been converted to the corresponding strain. This conversion can be obtained by dividing the crack width by a reference structural length. According to the σ-ε-design method (RILEM-TC-162-TDF, 2003), a bi-linear post-cracking constitutive model is assumed (Figure 2.14) (RILEM-TC-162-TDF, 2003). To evaluate this constitutive model, experimental data from the notched three-point

bending test (3PBT) is needed. According to (RILEM-TC-162-TDF, 2003), several tensile and flexural strengths are required, which can be obtained by the following equations:

$$f_{fctm,ax} = 0.3\,(f_{fck})^{\frac{2}{3}} \qquad (2.5.7)$$

$$f_{fctk,ax} = 0.7\,f_{fctm,ax} \qquad (2.5.8)$$

$$f_{fct,ax} = 0.6\,f_{fct,fl} \qquad (2.5.9)$$

$$f_{fctk,fl} = 0.7\,f_{fctm,fl} \qquad (2.5.10)$$

Table 2.4: *Strength classes for SFRC according to (RILEM-TC-162-TDF, 2003)*

Strength class of SFRC	**C20/25**	**C25/30**	**C30/37**	**C35/45**	**C40/50**
f_{fck} [MPa]	20	25	30	35	40
$f_{fctm,fl}$ [MPa]	3.7	4.3	4.8	5.3	5.8
E_{fcm} [MPa]	29	30.5	32	33.5	35

Where, f_{fck} is the characteristic cylinder compressive strength (Table 2.4), $f_{fctm,fl}$ and $f_{fctk,fl}$ are the mean and characteristic flexural tensile strength (Table 2.4), respectively and E_{fcm} is the mean secant modulus of elasticity (Table 2.4).

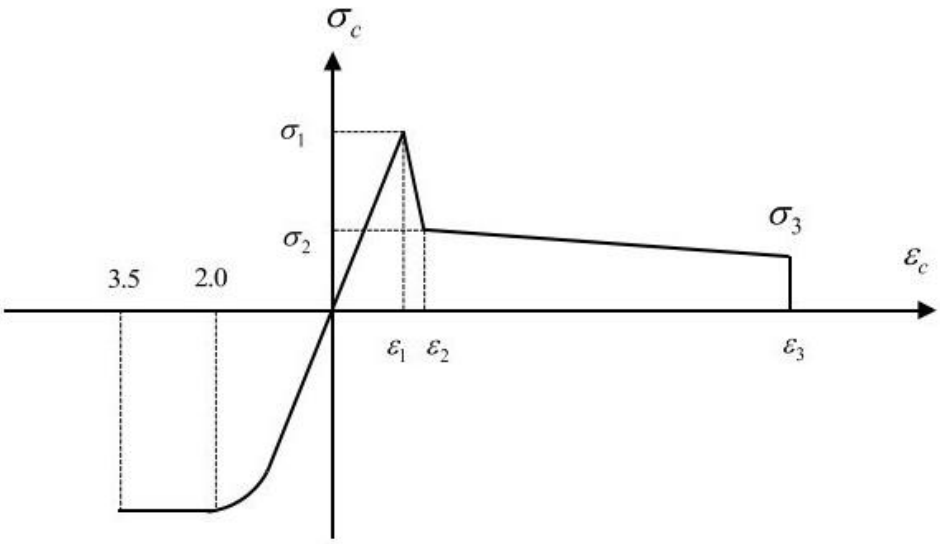

Figure 2.14: *Tensile post-cracking behaviour according to (RILEM-TC-162-TDF, 2003)*

(RILEM-TC-162-TDF, 2003) represents the tensile post-cracking behaviour based on residual flexural stresses, which are extracted from a notched three-point bending test (3PBT). The stress and strain points that form the tensile constitutive model are expressed below:

$$\sigma_1 = 0.7\, f_{fctm,fl}\ (1.6 - d) \qquad (2.5.11)$$

In case of SFRC with conventional reinforcement d is the effective depth in m, whereas in case of SFRC without conventional reinforcement, d is the thickness of the structural element in m.

$$\varepsilon_1 = \frac{\sigma_1}{E_c} \qquad (2.5.12)$$

$$E_c = 9500\left(f_{fck} + 8\right) \qquad (2.5.13)$$

$$\sigma_2 = 0.45\, f_{R1}\, \kappa_h \qquad (2.5.14)$$

$$\kappa_h = 1.0 - 0.6\, \frac{h - 12.5}{47.5}\ |12.5 \le h \le 60 \qquad (2.5.15)$$

$$\varepsilon_2 = \varepsilon_1 + 0.01\% \qquad (2.5.16)$$

$$\sigma_3 = 0.37\, f_{R4}\, \kappa_h \qquad (2.5.17)$$

$$\varepsilon_3 = 2.5\% \qquad (2.5.18)$$

Where, f_{R1} and f_{R4} represent the flexural tensile stress corresponding to $CMOD_1 = 0.5$ mm and $CMOD_3 = 3.5$ mm, respectively, and κ_h is the size factor.
It is beneficial to mention that the tensile constitutive model according to (RILEM-TC-162-TDF, 2003) is not applicable for slabs on grade, and cases with enhanced resistance to plastic shrinkage, abrasion as well as impact, i.e. it is applicable for cases in which steel fibres are used for structural purposes only.

2.6 Round indeterminate panel test

2.6.1 General

The use of sprayed (shotcrete) SFRC is a common method to line rock tunnels due to its advanced properties. To design SFRC as a lining layer, the structural behaviour of the rock and the lining layer needs to be described. The rock gives rise to a gravity load (a loose block can be considered as uniform load) that is supported by a continuous slab, which is the lining layer. This slab is supported by the rock bolts, which can be considered as columns; hence every column and the surrounded area can be analogized to a circular slab with continuous support under point load (Nilsson, 2001). From this concept, which is illustrated in Figure 2.15, the test of the round panel with continuous support has been developed.

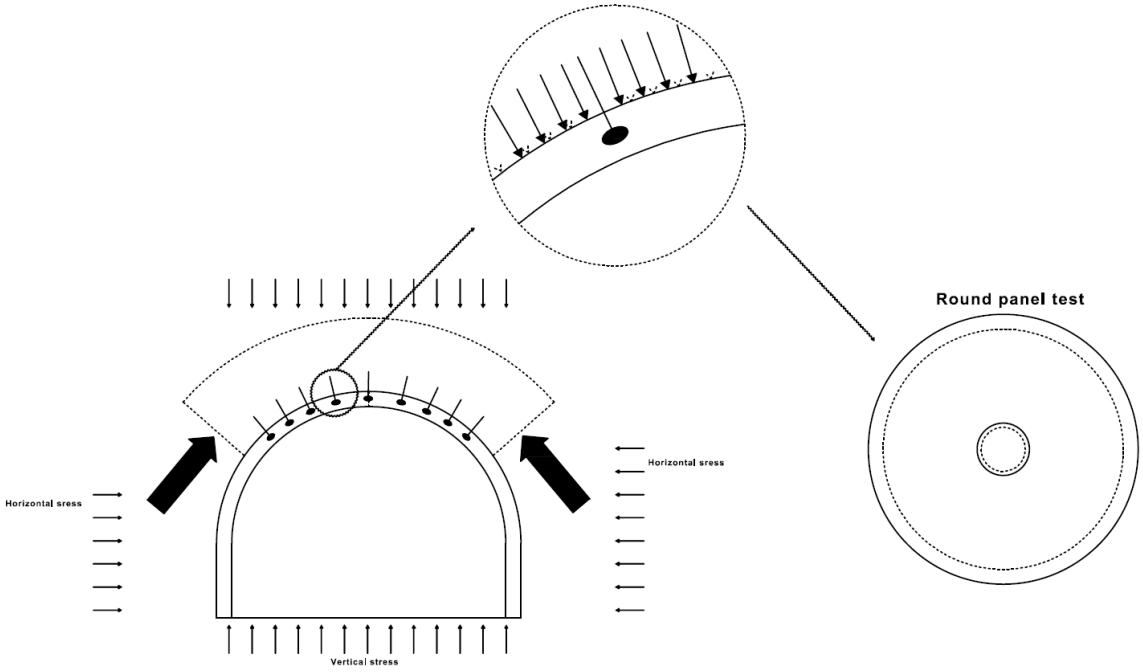

Figure 2.15: *Analogy between a bolted tunnel lining and test simulation. Recreated from (Vandervalle, 1991)*

The round panel test with continuous support has been implemented in the Norwegian standards to investigate the post-cracking capacity of fibre reinforced sprayed concrete under point load (Bernard, 2000) (Bjøntegaard, 2010). This test is critical in determining if the mix is suitable for lining the tunnels or not. However, the effect of boundary conditions and the way of carrying out the round panel test have been widely questioned, since the friction between the round panel and the support can impact the post-cracking capacity. In this work, the effect of different friction coefficients has been investigated to see how the friction influences the post-cracking capacity.

2.6.2 Effect of friction

The aim of this investigation is to study the effect of friction between the round panel and its continuous support on the post-cracking capacity. Several experimental results of round panel tests exhibit a higher capacity than when it is evaluated based on simple flexural theory. Since the effect of friction has been neglected in the calculation of post-cracking capacity of SFRC elements, this difference has become noticeable. To understand the effect of friction between the panel and its support, the movement of the panel under loading shall be analysed in each direction. Under point load, while the central part moves downwards, the contact zone between the round panel and the support moves in both radial and tangential directions Figure 2.16. It must be emphasised that this movement springs from the fact that the crack edges slide radially and tangentially (Bjøntegaard, 2010). In the presence of any kind of friction between the contact zone of the panel and its support, the movement will be resisted by the friction forces. Thereby, this friction acts as an external force; hence, the external work increases. Many approaches for evaluating the post-cracking capacity of the round panel are simplified. Due to this simplification, the friction forces have been ignored, which causes a discrepancy between simplified calculation results and experimental results (Bjøntegaard, 2010).

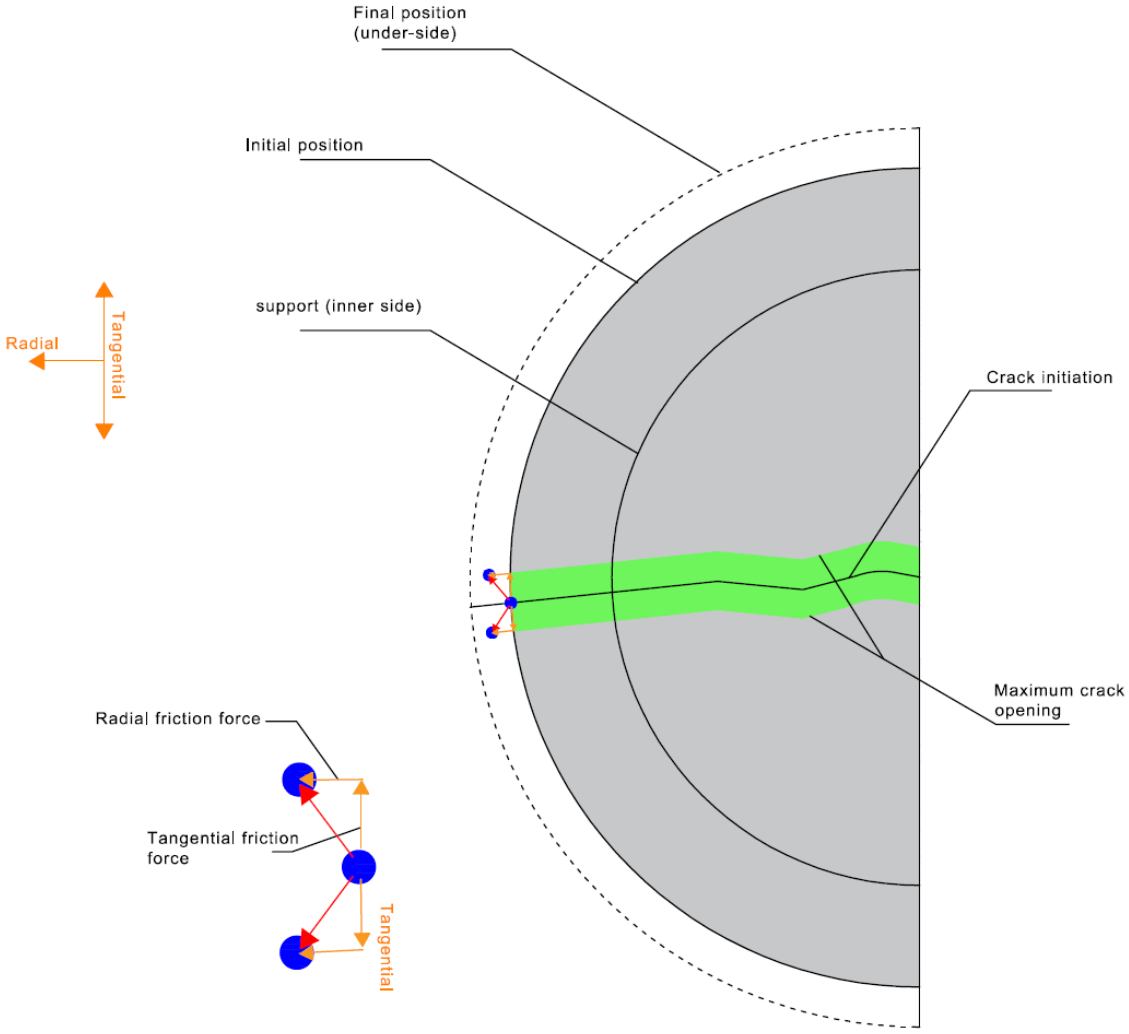

Figure 2.16: *Tangential and Radial movements in cracking of indeterminate round panel. Recreated from (Bjøntegaard, 2010)*

2.6.3 Failure mechanism

Many theories have been represented to evaluate the behaviour of concrete structures. The yield line theory can be considered as a good representation of the failure mechanism for concrete structures, which exhibits a plastic behaviour, as such a useful theory for evaluating the ultimate load resistance. The concept behind the yield line theory is that in the plastic range a certain characteristic pattern of cracks is formed, which at the end results in failure, and where the pattern is dependent on the type of loading as well as the boundary conditions (Hsueh, 1966). This failure pattern represents the hinges along the yield lines. However, there are a lot of potential failure mechanisms, and each of them can give a solution, which could be an upper-bound or lower-bound solution. Therefore, to be on the safe side, choosing the lower-bound solution, which has the lowest value among all the upper-bound solutions, is the most conservative choice. Returning to the round panel test, in order to evaluate the ultimate load that can be carried by the round panel, it is beneficial to use a combination of virtual work and yield line theory, which leads to a relationship based on the fact that the internal work

(dissipated energy) is equivalent to the external work. From Figure 2.17, the external load can simply be calculated, as stated below:

$$W_E = P_{ult.RP}\,\delta \qquad (2.6.1)$$

Where, $P_{ult.RP}$ is the ultimate load in case of round panel and δ is the deflection.

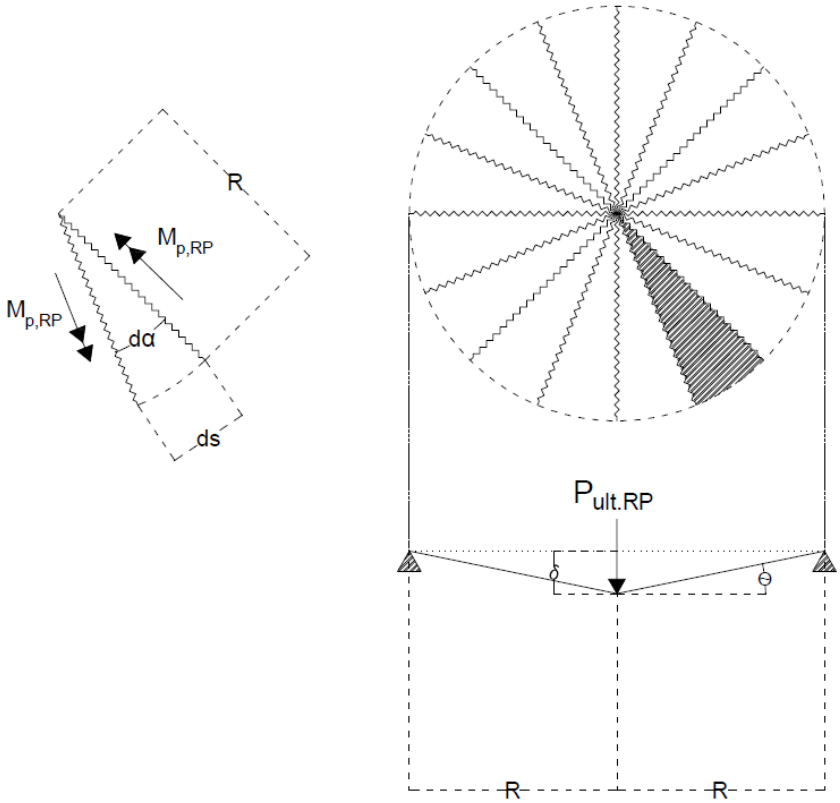

Figure 2.17: *Virtual-work theory for a simply supported round panel loaded with a centre point load. Recreated from (ACI, 2004)*

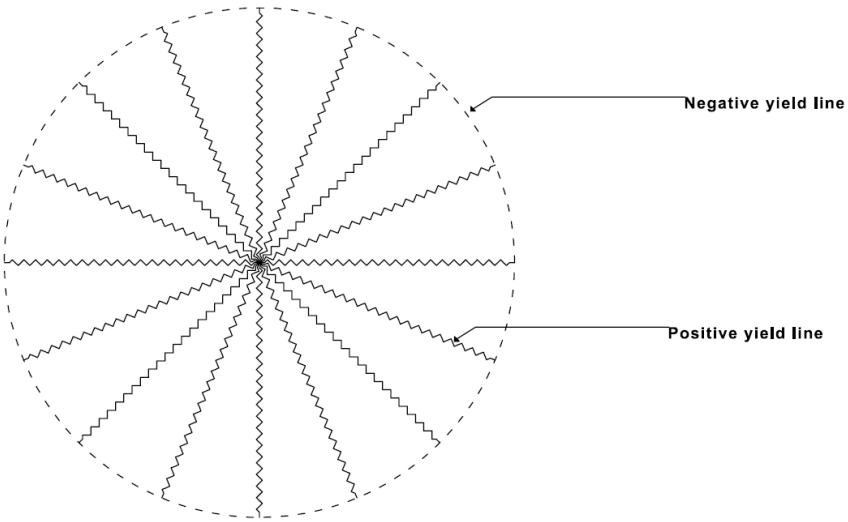

Figure 2.18: *Fan failure mechanism. Recreated from (ACI, 2004)*

On the other hand, the internal work (dissipated energy) can be calculated by firstly, assuming that a lot of cracks will initiate from the centre towards the perimeter (Fan Pattern) (Figure 2.18). Thus, an integration of the internal work on one triangular piece results in the internal work for the entire round panel. The internal work is stated in the following equations:

$$dW_l = M_{p,RP}\, R\, \theta\, d\alpha \qquad (2.6.2)$$

$$\theta = \frac{\delta}{R} \qquad (2.6.3)$$

$$dW_l = M_{p,RP}\, \delta\, d\alpha \qquad (2.6.4)$$

$$W_l = \int_0^{2\pi} M_{p,RP}\, \delta\, d\alpha = 2\pi\, \delta\, M_{p,RP} \qquad (2.6.5)$$

From the fact that internal work is equivalent to the external work, the following equation can be derived:

$$P_{ult.RP} = 2\pi\, M_{p,RP} \qquad (2.6.6)$$

To include the effect of loading plate size, which is used to apply the point load, equation (2.6.6) can be modified as suggested by (Soranakom, et al., 2007):

$$P_{ult.RP} = \frac{2\pi\, M_{p,RP}}{1 - \frac{2a}{3R}} \qquad (2.6.7)$$

Where, a is the radius of loading plate and R is the radius of round panel.

2.7 Slabs

2.7.1 General

Pile supported slabs are mostly used in industrial floors with a high level of loads, especially if the ground is not able to carry the load directly due to its insufficient bearing capacity. The most common application of SFRC is in the ground supported slabs, but when the use of ground-supported slabs is not possible due to the insufficient load-bearing capacity of the ground, SFRC can be used in pile-supported slabs as well. In the following section, some existing methods in the design of pile-supported slabs will be assessed. Influence of soil properties in the load transfer mechanism of the industrial floor is illustrated in Figure 2.19.

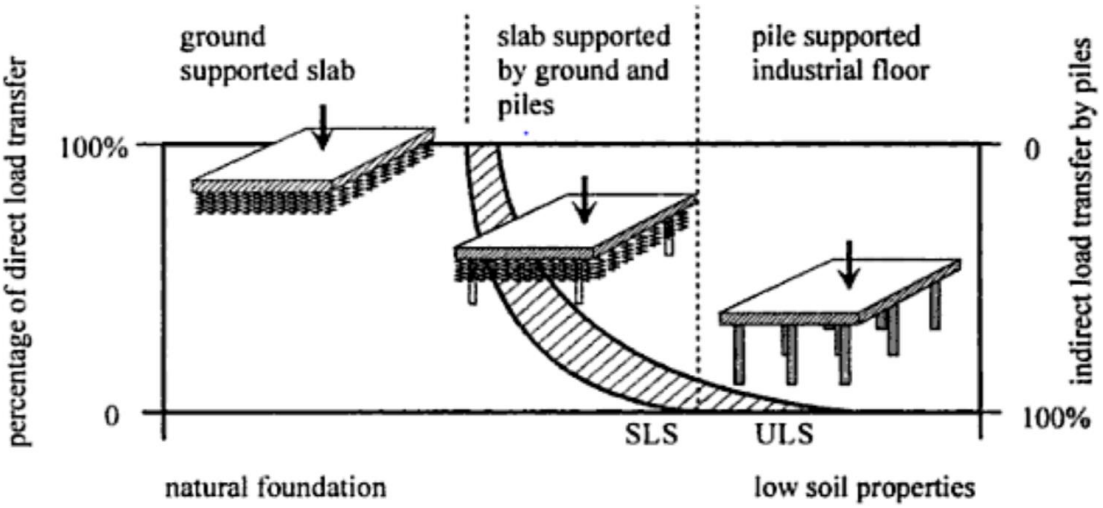

Figure 2.19: *Influence of soil properties on load-transfer of industrial floors, (H. Falkner, 1999)*

In pile-supported slabs, SFRC can be used with or without conventional reinforcement. Obviously, the former has some structural advantages such as enhanced ductility, crack control, reduced slab thickness as well as larger span length. But, the use of conventional reinforcement is more labour intensive and leads to longer construction time. On the other hand, the use of SRFC can solve the construction-related problems, whereas the cracks will be less controlled in comparison to conventional reinforced concrete. All in all, the best way to minimise disadvantages and maximise advantages mentioned above is to use a combination of SFRC with conventional reinforcement since the use of the following combination will lower the required reinforcement, and the cracks will be more controlled. Considering SFRC pile-supported slab without conventional reinforcement, which is the case in this master this, it is beneficial to mention that the fibre dosage and geometrical aspects can vary according to several research papers, which are summarised in Table 2.5.

Table 2.5: *Typical design aspects for pile supported slabs made by SFRC*

Object	Recommended Range	Unit	References
Typical pile spacing	3 - 5	m	(Destrée, 2006)
Typical slab thickness	200 - 320	mm	(The concrete society, 2013)
Fibre dosage	30 - 50	kg/m^3	(Hedebratt & Silfwerbrand, 2004)
Span-depth ratio	15	[-]	(The concrete society, 2013), (Destrée, 2006)

2.7.2 Loading

Since pile supported slabs are mostly used for industrial floors with specific types of loads, it is recommended to consider three types of loads for design purposes, including point load, line load as well as distributed load. Point load are representative of different load sources such as fixed machineries, heavy pallets equipment as well as heavy wheel load from good vehicles. On the other hand, the line load can be used to model the effect of partition walls standing on the slab. Obviously, uniformly distributed load is used as a representative of self-weight as well as imposed load. All in all, in this project only two separate load cases, which are the most critical, have been considered. The first load case is a combination of self-weight of slab and uniformly distributed imposed load. The latter is a combination of self-weight of slab and point load acting at centre of the slab.

2.7.3 Design criteria

Design criteria are based on two different states; the first criterion is the ultimate limit state (ULS), whereas the second one is the serviceability limit state (SLS).

2.7.3.1 Serviceability limit state

Industrial floors are required to be designed in an appropriate way to avoid excessive cracking as well as exceeding deflection. In case of not achieving the criteria of cracking and deflection in serviceability limit state, repair and renovation processes are necessary, which indeed requires that all the machines and equipment to be uninstalled and moved. In other words, this process is accompanied with a high labour effort as well as high economic cost (Oikonomou-Mpegetis, 2013). Moreover, in case of exceeding deflection, there are several risks since the machines and equipment can be highly sensitive to deflection. Also, for a better and safer feeling, a minimum safety and serviceability requirements shall be satisfied.

2.7.3.2 Ultimate limit state

Regarding the ultimate limit state (ULS), there are two potential failure mechanisms in case of pile-supported slab subjected to uniformly distributed load, flexural failure mechanism as well as shear punching mechanism. In the former case, the cracks will be located at the line passing over the columns centre line as well as the line passing through the span between the columns. In case of interior panel, the mentioned set of cracks, which is in the span between the columns,

will be located at the line passing through the midspan. The set of cracks, which passes over the columns represents the negative moment (negative yield line), whereas the other set of cracks, which passes through the span, is repetitive of the positive moment (positive yield line). Mentioned model is known as "folded plate failure mechanism" (Kennedy & Goodchild, 2004), and is depicted in Figure 2.20.

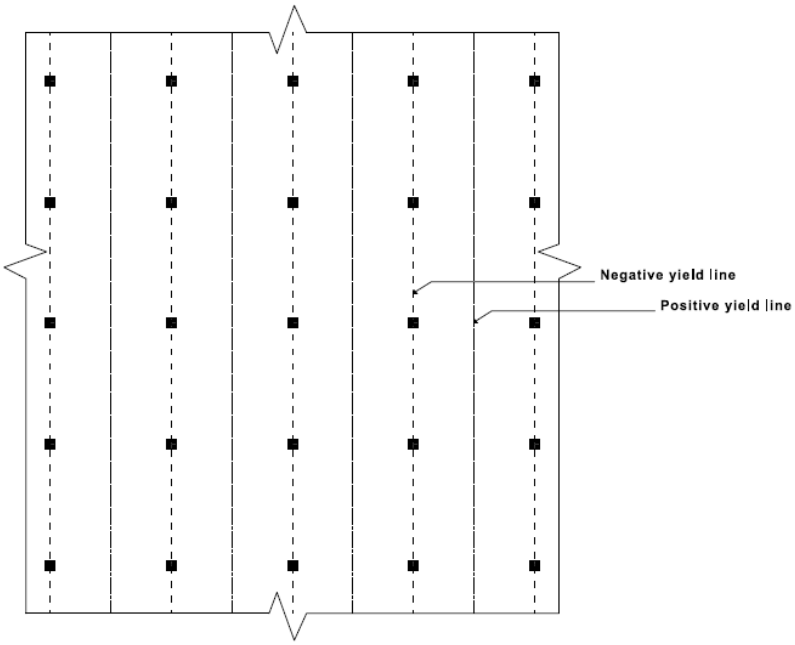

Figure 2.20: *Folded plate failure mechanism. Recreated from (Kennedy & Goodchild, 2004)*

It should be noticed that there is another potential local bending type of failure that can occur in another way, which is illustrated in Figure 2.21. In this type of failure, a circular fan pattern will form over the pile caps due to an applied bending, which is higher than the moment sectional capacity. The mentioned fan pattern in this local failure has a circular crack pattern in the bottom surface, which are representative of positive yield lines as well as radial cracks, which emanate from the pile cap toward the mentioned circular crack pattern. The mentioned radial cracks represent the negative yield lines. This type of local bending failure is rarely probable in comparison to the folded plate mechanism.

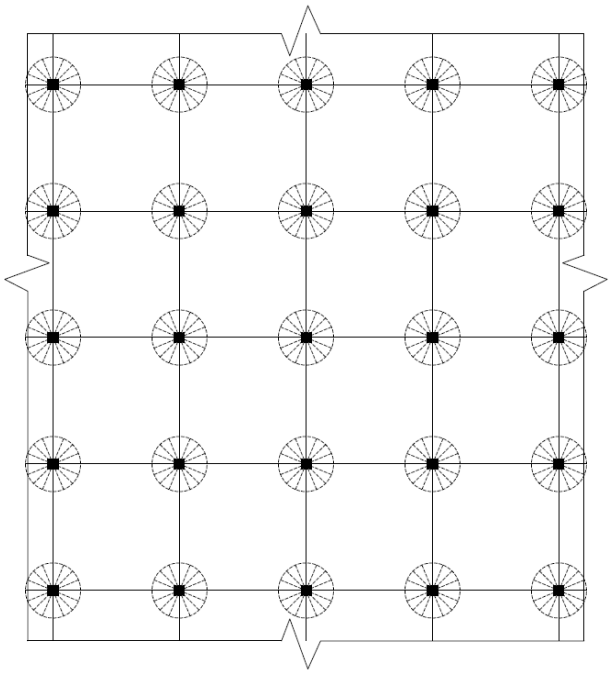

Figure 2.21: *Circular fan pattern failure mechanism. Recreated from (Kennedy & Goodchild, 2004)*

Furthermore, in the shear punching failure mechanism, a conical crack pattern forms around the perimeter of the pile head, i.e. the failure mechanism is conical and forms around the pile head. This failure mechanism is more discussed in detail in 2.7.4.3.
As mentioned before, pile-supported slabs could be under point load due to the presence of fixed machinery and good vehicles. The effect of point load results in a specific failure mechanism, which is known as "fan failure mechanism". The mentioned failure mechanism is exactly the same as the failure mechanism of the round panel test, where a lot of cracks will initiate at the location of the point load in all directions (Figure 2.22).

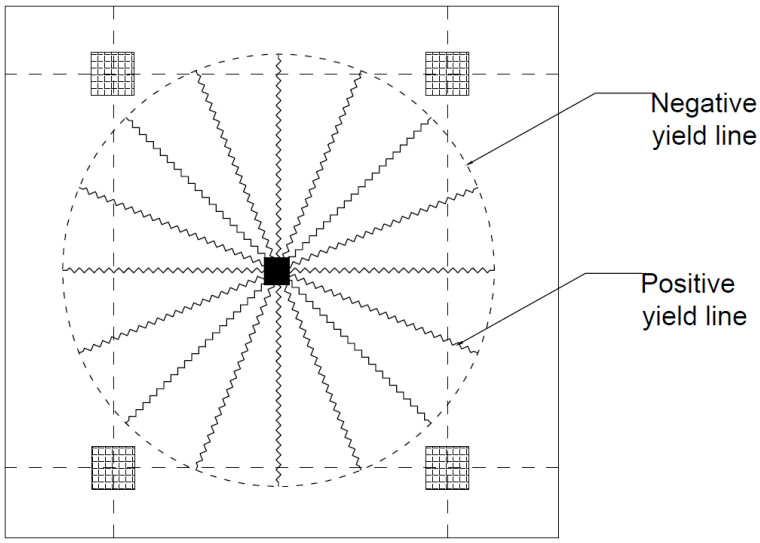

Figure 2.22: *Fan failure mechanism for interior panel under point load. Recreated from (ACI, 2004)*

2.7.4 Design method

There are several approaches for evaluation of the post-cracking capacity, deflection as well as crack width. The following approaches vary from elastic theory to yield line theory. The former is an appropriate choice for assessment of deflection and stresses in the serviceability limit state; however, it is a conservative choice for evaluation of the ultimate strength of SFRC. The second alternative is the yield line theory, which has been explained before as a good representative for evaluation of the ultimate strength.

2.7.4.1 Elastic design

One of the most conservative theories for all structural members, including pile-supported slabs, is the elastic theory. This theory has been implemented in (The concrete society, 2013) for the design of pile-supported slabs in the ultimate limit state. In the following method, moment value at the support is evaluated just in the case of uniformly distributed load, i.e. the ultimate strength under point loads as well as line loads cannot be evaluated. For evaluation of the moments, the following formula is expressed:

$$M_{el} = \alpha_{m.c}\, q\, L_{sp}^2 \qquad (2.7.1)$$

Where, q denotes the uniformly distributed load, L_{sp} denotes the span length, and $\alpha_{m.c}$ is the moment coefficient, which has been recommended to be chosen as present in Table 2.6 according to (The concrete society, 2013).

Table 2.6: *Moment coefficient for different types of panel*

Type of Panel	Moment coefficient ($\alpha_{m.c}$)
Internal Panel	0.132
External Panel	0.178
Corner Panel	0.190

All the support moments as well as span moments will be calculated for strips with a width equal to $\frac{L_{sp}}{2}$ and $\frac{L_{sp}}{4}$, which are named middle strip and edge strip, respectively.

Since the elastic theory is designing based on the elastic state of behaviour, it doesn't consider the post cracking behaviour with respect to its stiffness and moment distribution. On the other hands, fibres will be effective when the cracks initiate, by arresting the crack growth that leads to increased ductility, i.e. more energy will be dissipated. It can be deduced that by using the elastic design method, the fibres will not have any remarkable effect and it can be confirmed that another approach shall be chosen to take the effect of fibres into account.

2.7.4.2 Yield line theory

Yield line theory (YLT) is an alternative method for the design of pile-supported slabs, which gives several potential solutions (upper-bound solutions), where some of them are not on the safe side. Therefore, among all the upper-bound solutions, the one with the lowest value is the lower-bound solution and on the safe side (Hsueh, 1966). The YL-method was developed by (Johansen, 1972) and is known as plastic analysis based on the failure mechanism. YLT is a suitable choice, since the assumed crack pattern in the failure mode (yield lines) matches, to some extent, the actual crack pattern (failure mode). Regarding the failure load, it is necessary to use a combination of YLT and virtual work concept, i.e. the external work based on the load at the failure must be equal to the internal work that is a function of internal forces. YLT is applicable for flexural failure mechanisms in the ultimate limit state; the mentioned folded plate mechanism in slabs as well as circular fan pattern mechanism. Depending on the response of the slab under uniformly distributed load, the following yield lines and moment distributions, as illustrated in Figure 2.20, Figure 2.23, can be assumed for different types of panels depending on if it is a corner-panel, mid-panel or edge-panel. It is also assumed that the slab has enough rotational capacity to make the plastic hinge, which is necessary for the mechanism formation (Oikonomou-Mpegetis, 2013).

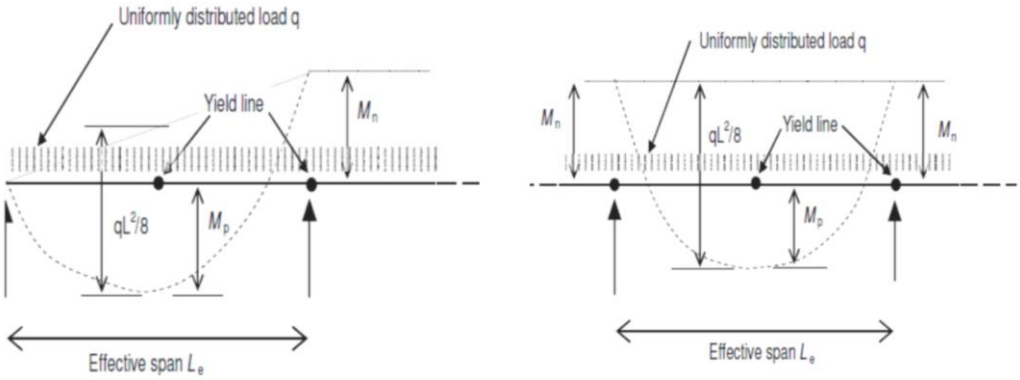

Figure 2.23: *Folded plate mechanism in an exterior panel (left) and an interior panel (right) under uniformly distributed load, (The concrete society, 2013)*

By applying YLT, a set of negative and positive yield lines are introduced, which represent negative and positive moments, respectively. Furthermore, for design purposes, by combining the virtual work concept with the yield line theory, the allowable moment capacity for the span section as well as the support section can be evaluated. It should be noticed that the ratio between the negative and positive moments shall be assumed, which is equivalent to one in case of SFRC without conventional reinforcement and with the same cross-sectional geometry. In case of analysing an SFRC pile supported slab, the moment capacity can be obtained according to several approaches such as fib model code 2010 (2.5.3.3), σ-ε-design method (2.5.3.5) as well as adaptive inverse analysis approach (2.5.3.4). Afterwards, the allowable load can be evaluated based on the obtained moment capacity.
In case of an interior panel in a pile-supported slab under uniformly distributed load, the combination of virtual work with yield line results in obtaining the equations that are stated below:

$$W_l = W_E \tag{2.7.2}$$

For segment AB in Figure 2.25, Eq.(2.7.2) can be applied as described:

$$q_{ult,SD}\ x_{0,SD}\ \frac{\delta_{SD}}{2} = M^{-}_{Py1,SD}(\theta_{1,SD}) + M^{+}_{Py,SD}(\theta_{1,SD}) \tag{2.7.3}$$

Where, $M^{-}_{Py1,SD}$ and $M^{+}_{Py,SD}$ are the negative and positive moment capacities in y-direction, respectively (Figure 2.24).

Note: The location of negative yield lines shall be assumed, and the position can affect the moment capacity. For instance, if the location is outside of the column, that would result in a higher capacity (upper-bound solution), whereas if it is close to the column support, a more conservative solution can be achieved. In other words, as much as the assumed negative yield line is further away from the column, the calculated capacity is larger.

Since the deflection is equivalent to segment length ($x_{0,SD}$) multiplied by the corresponding rotation ($\theta_{1,SD}$), Eq.(2.7.3) can be expressed as stated below:

$$\delta_{SD} = x_{0,SD}\ \theta_{1,SD} \tag{2.7.4}$$

$$M^{-}_{Py1,SD}(\theta_{1,SD}) + M^{+}_{Py,SD}(\theta_{1,SD}) = q_{ult,SD}\ x_{0,SD}\ \frac{(x_{0,SD}\ \theta_{1,SD})}{2} \tag{2.7.5}$$

$$M^{-}_{Py1,SD} + M^{+}_{Py,SD} = \frac{q_{ult,SD}\ x^2_{0,SD}}{2} \tag{2.7.6}$$

The same procedure can be applied for segment BC, which results in the following equation:

$$M^{-}_{Py2,SD} + M^{+}_{Py,SD} = \frac{q_{ult,SD}\ (L_{rx} - x_{0,SD})^2}{2} \tag{2.7.7}$$

By assuming that $\phi_{y1,SD} = M^{-}_{Py1,SD}/M^{+}_{Py,SD}$ and $\phi_{y2,SD} = M^{-}_{Py2,SD}/M^{+}_{Py,SD}$, Eq.(2.7.6) and Eq.(2.7.7) can be revised as follows:

$$M^{+}_{Py,SD}(1 + \phi_{y1,SD}) = \frac{q_{ult,SD}\ x^2_{0,SD}}{2} \tag{2.7.8}$$

$$M^{+}_{Py,SD}(1 + \phi_{y2,SD}) = \frac{q_{ult,SD}\ (L_{rx} - x_{0,SD})^2}{2} \tag{2.7.9}$$

To calculate the length of segment AB ($x_{0,SD}$), it is beneficial to divide Eq.(2.7.9) by Eq.(2.7.8), which results in obtaining the following equation:

$$x_{0,SD} = L_{rx}\left(\frac{\sqrt{(1+\phi_{y1,SD})}}{\sqrt{(1+\phi_{y1,SD})}+\sqrt{(1+\phi_{y2,SD})}}\right) \quad (2.7.10)$$

By inserting Eq.(2.7.10) into Eq.(2.7.8), the following equation can be obtained:

$$M^{+}_{Py,SD} = \frac{q_{ult,SD}\, L^2_{rx}}{2\left(\sqrt{(1+\phi_{y1,SD})}+\sqrt{(1+\phi_{y2,SD})}\right)^2} \quad (2.7.11)$$

The same procedure can be followed for the moment capacity in x-direction, which results in the following equation:

$$M^{+}_{Px,SD} = \frac{q_{ult,SD}\, L^2_{ry}}{2\left(\sqrt{(1+\phi_{x1,SD})}+\sqrt{(1+\phi_{x2,SD})}\right)^2} \quad (2.7.12)$$

According to limitations, fibre orientation has been neglected in this work; hence, the fibres are assumed to be distributed uniformly. Therefore, it can be assumed that $\phi_{y1,SD} = \phi_{y2,SD} = \phi_{x1,SD} = \phi_{x2,SD} = \phi_{h,SD}$. This assumption results in simplifying the previous equations as state below:

$$M^{+}_{Px,SD} = \frac{q_{ult,SD}\, L^2_{ry}}{8(1+\phi_{h,SD})} \quad (2.7.13)$$

$$M^{-}_{Px,SD} = \phi_{h,SD}\, M^{+}_{Px,SD} \quad (2.7.14)$$

$$M^{+}_{Py,SD} = \frac{q_{ult,SD}\, L^2_{rx}}{8(1+\phi_{h,SD})} \quad (2.7.15)$$

$$M^{-}_{Py,SD} = \phi_{h,SD}\, M^{+}_{Py,SD} \quad (2.7.16)$$

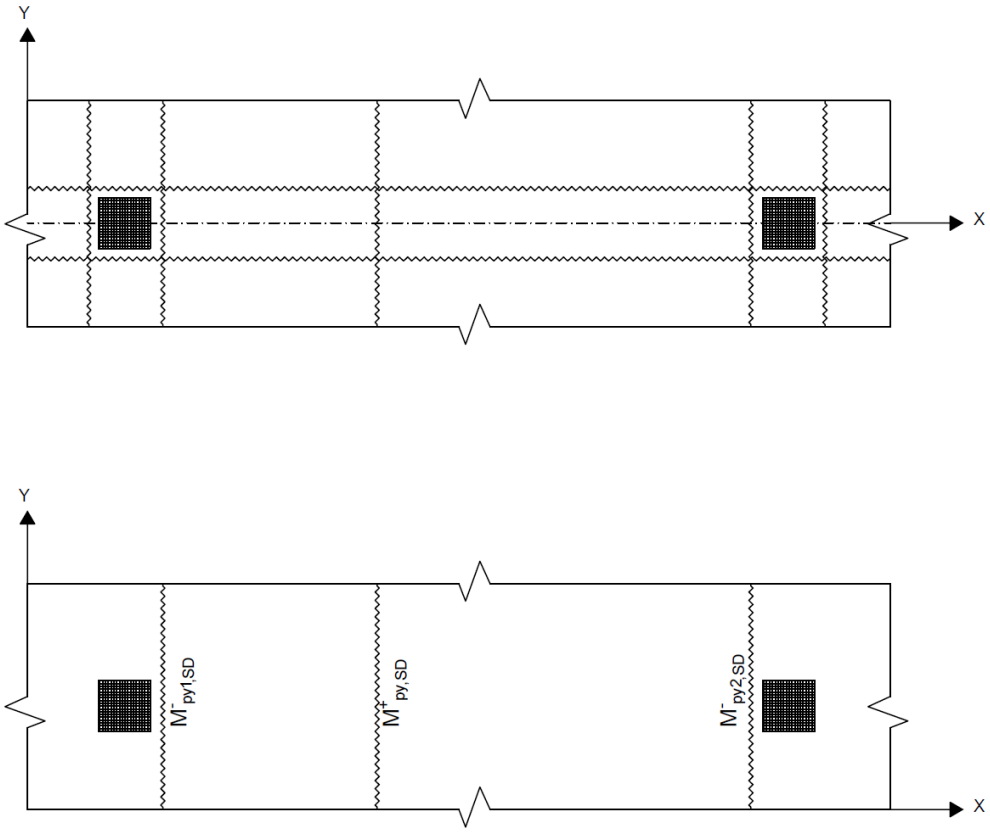

Figure 2.24: *Positive and negative yield lines for an interior panel. Recreated from (ACI, 2004)*

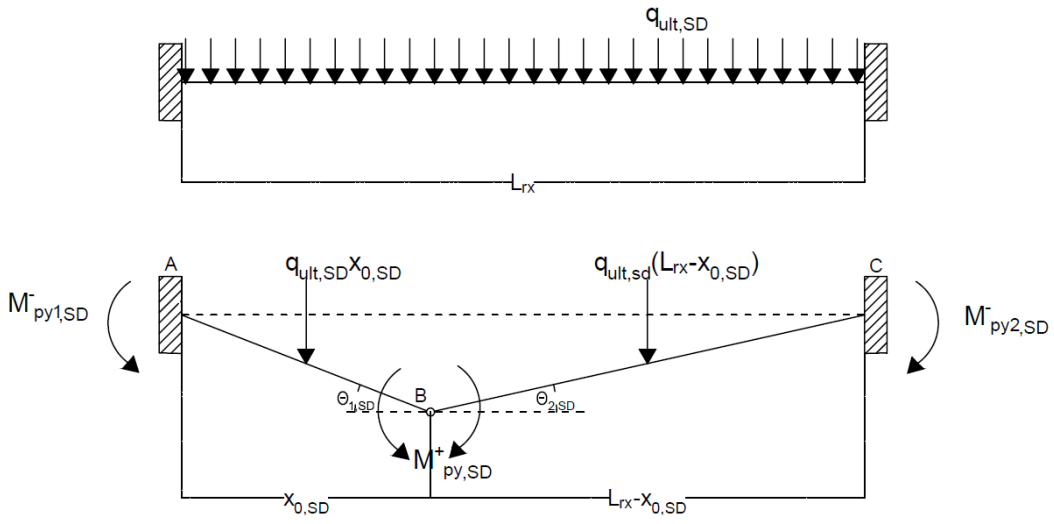

Figure 2.25: *Principle of virtual work for an interior panel. Recreated from (ACI, 2004)*

In case of an interior panel in a pile-supported slab under point load, the same combination of virtual work with yield line theory can be used (Figure 2.26). Since the failure mechanism is fan pattern, integration of the internal and external work on one triangular piece results in the internal and external work for the entire slab as stated below:

$$dW_l = M^-_{P,SP}\, R_{SP}\, \theta_{SP} d\alpha + 2\left(M^+_{P,SP}\, R_{SP}\, \theta_{SP}\, \frac{d\alpha}{2}\right) = \left(M^+_{P,SP} + M^-_{P,SP}\right) R_{SP}\, \theta_{SP} d\alpha \quad (2.7.17)$$

$$dW_l = M^+_{P,SP}\left(1 + \phi_{h,SP}\right) R_{SP}\, \theta_{SP} d\alpha \quad (2.7.18)$$

Where $\phi_{h,SP} = M^-_{P,SP}/M^+_{P,SP}$

$$dW_E = \left[\left(\frac{P_{ult,SP}}{\pi\, a^2_{SP}}\right)\left(\frac{2\, a^2_{SP}}{2\, \pi}\right) \delta_{SP}\right] d\alpha = \left[\left(\frac{P_{ult,SP}}{2\, \pi}\right)\left(R_{SP} - \frac{2}{3}\, a_{SP}\right) \theta_{SP}\right] d\alpha \quad (2.7.19)$$

By applying the law of work and energy conservation (Castigliano's theorem), the following equations can be obtained:

$$\int_0^{2\pi} M^+_{P,SP}\left(1 + \phi_{h,SP}\right) R_{SP}\, \theta_{SP} d\alpha = \int_0^{2\pi} \left[\left(\frac{P_{ult,SP}}{2\, \pi}\right)\left(R_{SP} - \frac{2}{3}\, a_{SP}\right) \theta_{SP}\right] d\alpha \quad (2.7.20)$$

$$M^+_{P,SP} = \frac{P_{ult,SP}\left(1 - \frac{2}{3}\, \frac{a_{SP}}{R_{SP}}\right)}{2\pi\left(1 + \phi_{h,SP}\right)} \quad (2.7.21)$$

Where $M^+_{P,SP}$ and $M^-_{P,SP}$ are the positive and negative moment capacities, respectively.

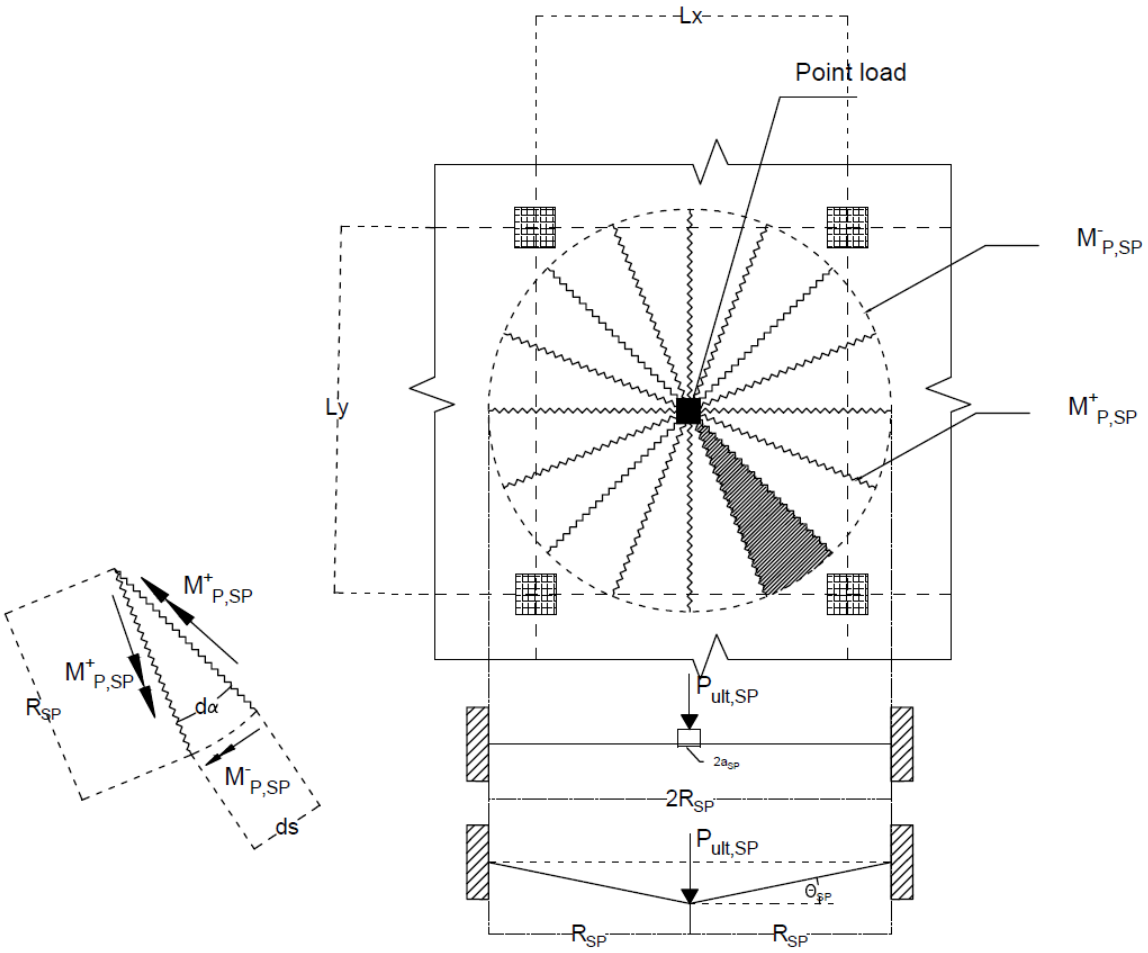

Figure 2.26: *Virtual-work theory for an interior panel under point load. Recreated from (ACI, 2004)*

2.7.4.3 Punching shear failure

Punching shear failure is a failure due to high shear stresses, which act localized at column support points. Flexural failure usually is a ductile type of failure, while shear punching failure is highly brittle, which causes in rapid loss of resistance, leading to a more dangerous failure type (Oikonomou-Mpegetis, 2013). Due to this fact, this failure mechanism has been under investigation for many years, especially for the case of pile-supported slabs (Ericsson & Farahaninia, 2010). Considering steel fibre reinforced concrete, it has been observed by (Criswell, 1974) that additional fibres increase the punching shear capacity, which is counted as a positive effect from the fibres. It can be motivated by the fact that fibres act as shear reinforcement by transferring tension across the cracks. Furthermore, it leads to increased flexural, compressive zone, which indeed increases the shear resistance (Oikonomou-Mpegetis, 2013).

2.7.5 Arching action

As stated before, yield line theory can be used for evaluation of ultimate load resistance. Although the application of yield line theory in many cases exhibited a good evaluation of the ultimate load resistance, the experimental tests for some concrete structures, especially slabs, showed an ultimate capacity that was much higher than the calculated one. Thus, several research papers such as (Beeby & Fathibitaraf, 2001) and (Belletti & Vitulli, 2014) have investigated the source of the mentioned difference in the ultimate load resistance. Since, in the yield line theory, it is assumed that the deformation of any slab stems from the rotation around the yield lines, the evaluated ultimate load resistance is based on the pure moment only, i.e. all in-plane forces are ignored. Nevertheless, in reality, in-plane forces can be formed, which in fact will result in increased moment resistance in the yield lines (Desayi & Kulkarni, 1977). These in-plane forces stem from the fact that the "exterior edges" of the slab or its supports are prevented from moving laterally. In case of restraining the exterior edges of the slab, compressive forces will appear and cause the so-called ''arching action'' (Desayi & Kulkarni, 1977). The interior slab responds as a restrained slab, which results in the formation of arching action phenomenon (Beeby & Fathibitaraf, 2001). The benefit of arching action phenomenon is that it enhances the ultimate strength, which is attained because of two involved effects. The first effect is that in the mid-span, the location of the compressive forces will be above the mid-depth, whereas, at the restrained edges the location of the compressive forces will be below the mid-depth (Figure 2.27) (Desayi & Kulkarni, 1977). The second effect is that mentioned compressive forces will increase the moment resistance in the yield lines, which leads to enhancement of ultimate strength. Up to now, there is no clear available procedure to include the effect of arching action neither for reinforced concrete structures nor for SFRC structures. Since there are several difficulties in defining the so-called "degree of restraining" and how that can affect arching action, several researchers have done relevant efforts with aim of introducing a realistic procedure to include the effect of arching action, particularly for SFRC slabs (Venkateshwaran & Tan, 2018), while these procedures are still limited to geometry of the slab as well as the boundary conditions.

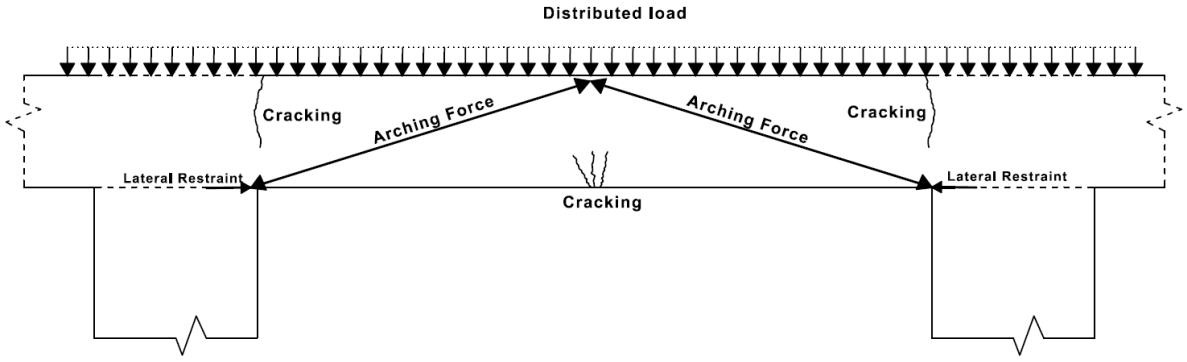

Figure 2.27: *Arching action in SFRC interior panels. Recreated from (Beeby & Fathibitaraf, 2001)*

3 Finite element analysis

3.1 Iterative method

An essential tool for solving non-linear finite element related problems is an iterative procedure, which can be used to satisfy the equilibrium for several criteria such as energy and displacement. Several alternatives can be used as an iterative procedure, such as regular Newton-Raphson, Modified Newton-Raphson, Quasi Newton-Raphson as well as Broyden-Fletcher-Goldfarb-Shanno (BFGS). It is beneficial to mention that among all the available iterative methods, the most appropriate choice for specific problem shall be chosen based on its efficiency, convergence rate as well as accuracy in related problems. Among all the alternatives mentioned above, regular Newton-Raphson is studied more in detail in the following section. In the regular Newton-Raphson method, the stiffness matrix will be updated in each step, which is the most efficient and common approach in related structural problems (Ebelechukwu, et al., 2018), (Irani & Abadi, 2013). The initial stiffness matrix is assumed to be the tangential stiffness matrix named K_0, which will be used in extrapolation to obtain a correction for initial displacement u_0. Furthermore, by the updated displacements, internal forces can be calculated, which will be used to find the total applied force as well as the residual force. This updating procedure continues until the residual force satisfies the tolerance criteria (Malm, 2015), (Eriksson & Karlsson, 2016). An illustration of the following iterative procedure is present in Figure 3.1.

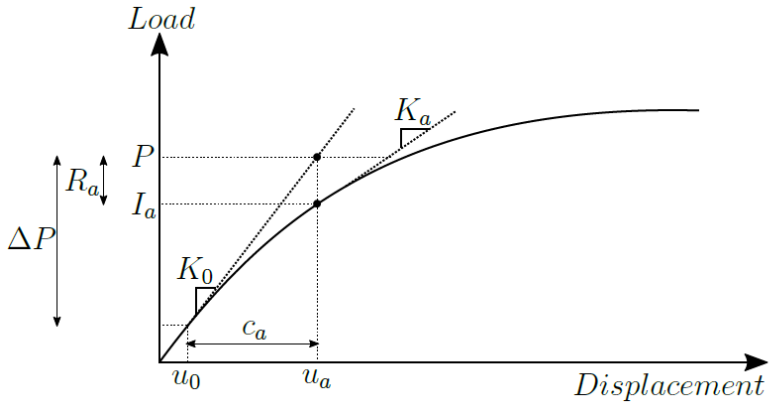

Figure 3.1: *Iterative procedure for an increment in non-linear FEA (Load-Displacement Case), (Malm, 2015)*

The iterative procedure can start by assuming that $x_{0,i}$ is the initial estimation of the true root (r_i), which is equivalent to $x_{0,i} + h_i$. Hence, h_i is the number, which measures how far the initial estimation is from the truth. As h_i is small, the tangential line can be used as an approximation, which results in the following equation:

$$0 = f(r_i) = f\left(x_{0,i} + h_i\right) \approx f\left(x_{0,i}\right) + h_i\, f'\left(x_{0,i}\right) \qquad (3.1.1)$$

If $f'\left(x_{0,i}\right)$ is not close to zero, h_i is:

$$h_i \approx \frac{f(x_{0,i})}{f'(x_{0,i})} \qquad (3.1.2)$$

Hence, the true root can be described as follows:

$$r_i = x_{0,i} + h_i \approx x_{0,i} + \frac{f(x_{0,i})}{f'(x_{0,i})} \qquad (3.1.3)$$

Then, $x_{1,i}$ is the improved estimation, which can be derived as follows:

$$x_{1,i} = x_{0,i} - \frac{f(x_{0,i})}{f'(x_{0,i})} \qquad (3.1.4)$$

The next improved estimation can be derived from the previous one, exactly by the same approach that previous estimation has been derived from the initial one:

$$x_{2,i} = x_{1,i} - \frac{f(x_{1,i})}{f'(x_{1,i})} \qquad (3.1.5)$$

By use of the equation, which is stated below, this procedure can continue until obtaining an estimation that fulfils the assumed tolerance:

$$x_{(n+1),i} = x_{n,i} - \frac{f(x_{n,i})}{f'(x_{n,i})} \qquad (3.1.6)$$

3.2 Crack model

Cracks can be modelled based on different assumptions, among which non-linear fracture mechanics, a model that considers the propagation of single cracks, is the most common model (Plos, 1996). Three major approaches are known for modelling of cracks based on their finite element method formulation, discrete crack approach, smeared crack approach as well as embedded crack approach. The last method is for the case of reinforced concrete while the two other alternatives at hand, discrete and smeared crack approach are more suitable for other purposes, including steel fibre reinforced concrete without conventional reinforcement. In the former approach, a separate crack element is necessary to be defined, which causes a discontinuity in the material (Plos, 1996). Furthermore, the region, which is not in the cracked zone needs to be modelled based on ordinary continuum element. On the other hand, in the smeared crack approach, a continuum material is considered for all the elements, and the response of the cracks will be smeared out over the elements. The main disadvantage of the discrete method is that it requires to define the location of the cracks as well as defining a special crack element (Plos, 1996). In cases that the location of the cracks can be predicted

such as notched beams (e.g. 3PBT), the former disadvantage doesn't exist, but still, there is a need to define a special type of crack element. On the other hand, the smeared crack approach considers crack initiation as well as crack propagation in one element row, which results in a fracture process. Obviously, a constitutive continuum relation, which is defined in terms of stress-strain relationship needs to be defined as the constitutive material model, including cracks. (Plos, 1996)

The smeared crack approach itself can be based on two different assumptions, which are known as the fixed crack model and the rotating crack model. The mentioned models are similar in their assumption about the crack initiation, i.e. in both crack models, the first crack will form when the maximum principal stress becomes equal to the tensile capacity of the material. Contrarily, in the propagation of the cracks, the fixed crack model, assumes that the crack will continue to propagate with the same initial crack direction, an assumption that results in shear stress on the crack surface due to the difference between the direction of the crack with respect to that of maximum principal stress. On the other hand, the rotating crack model considers that the crack rotates and propagates in the direction of the maximum principal stress, i.e. the crack direction will adapt itself with the direction of the maximum principal stress. Obviously, there will not be any effect of shear stress on the cracked surface for the rotating crack model. The schematic illustration of both crack models and their state of stress is presented in Figure 3.2 and Figure 3.3 (Eriksson & Karlsson, 2016).

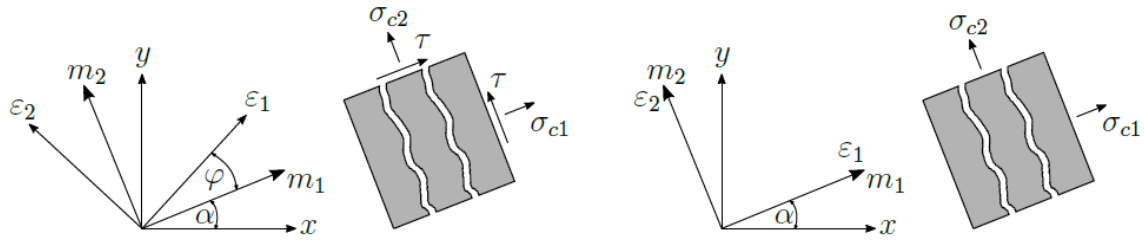

Figure 3.2: *Stress and strain states for fixed crack model as well as rotating crack model. Recreated by (Eriksson & Karlsson, 2016)*

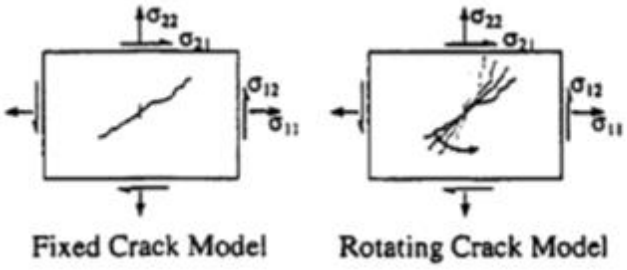

Figure 3.3: *Stress and crack direction in fixed crack model and rotating crack model, (Milne & R.O. Karihaloo, 2003)*

3.3 Element types

3.3.1 Plane stress elements

Plane stress elements, which are also known as membrane elements, can be used when the element nodes are located on a flat plane, i.e. the thickness of the plane is small in relation to other dimensions. Besides the geometrical limitation, this element can be used just when the stress component perpendicular to the face of the plane is zero. A schematic view of plane stress element is presented in Figure 3.4 (TNO DIANA, 2017).

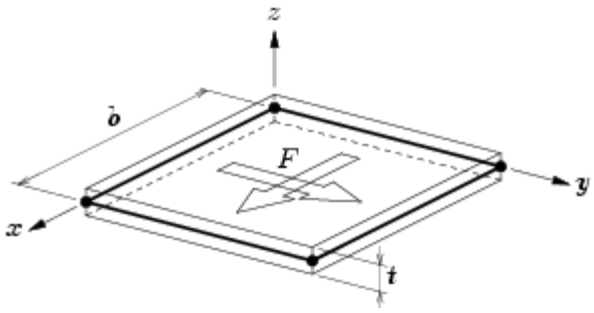

Figure 3.4: *Schematic sketch of plane stress element, (TNO DIANA, 2017)*

Considering degrees of freedom (DOF's) for this type of element, there are three DOF's; two translational and one rotational, which are well illustrated in Figure 3.5. The translational ones are in the planar direction while the rotational DOF is the so-called "drilling rotation" (TNO DIANA, 2017).

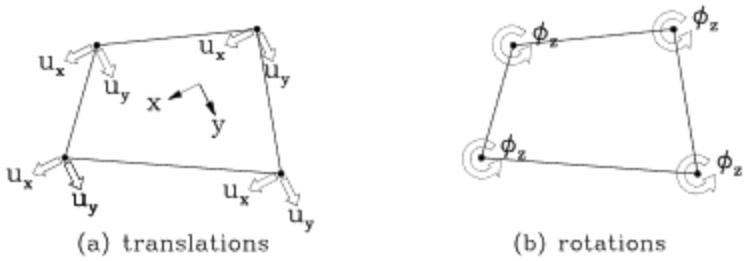

Figure 3.5: *Displacement of flat plane element, (TNO DIANA, 2017)*

It is beneficial to mention that, this type of element is valid for several types of loading such as distributed load, point load, strain load, temperature as well as initial stresses (TNO DIANA, 2017).

3.3.2 Curved shell elements

Shell elements, in general, are a suitable choice for describing bending and bending failure. Moreover, it can be used to describe the in-plane shear stresses to some extent, whereas it cannot be used to describe the out-of-plane shear stresses. More specific, curved shell elements can be defined based on several assumptions among, which isoperimetric degenerated-solid approach that introduces two shell hypothesis, Straight-normals and Zero-normal-stress are more compatible with FE software, DIANA (TNO DIANA, 2017). In the former hypothesis, normals are assumed to remain straight, while it is not necessarily normal to the reference surface. Furthermore, on the second hypothesis, the normal stress component in the normal

direction of a lamina basis is forced to be zero (TNO DIANA, 2017). A schematic characteristic view of curved shell elements is illustrated in Figure 3.6.

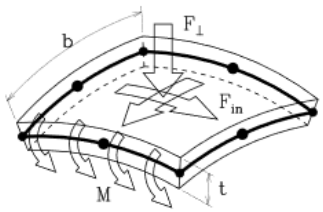

Figure 3.6: *Schematic sketch of curved shell element, (TNO DIANA, 2017)*

For the in-plane lamina strains, which includes strains in XX and YY direction as well as the XY strains, there is a linear variation assumption, whereas the shear strains in XZ and YZ directions are forced to be zero along the thickness direction. In this type of element there are five degrees of freedom assumed for every element node, three translational and two rotational Figure 3.7.

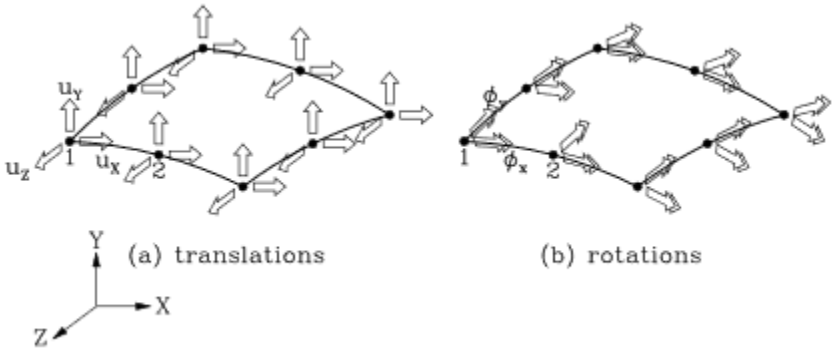

Figure 3.7: *Displacements of a curved shell element, (TNO DIANA, 2017)*

In a similar way to plane stress elements, in the curved shell elements, the member should be thin, i.e. the thickness should be much smaller than the other dimensions of the plane. On the contrary with plane stress elements, which is not valid for forces perpendicular to the face of the element, on the curved shell elements the load may act from between perpendicular to the surface and in the surface (TNO DIANA, 2017). Therefore, this type of element is a good choice for modelling of curved structures such as shell roofs, storage tanks and ship or aircraft halls. The load can also be from several categories such as concentrated load, distributed load, temperature as well as initial stresses (TNO DIANA, 2017).

3.3.3 Solid elements

Solid elements (Figure 3.8), which are the most general-purpose elements are based on a large system of equations, a fact that makes them an inefficient choice when other element types are suitable and producing accurate results (TNO DIANA, 2017).

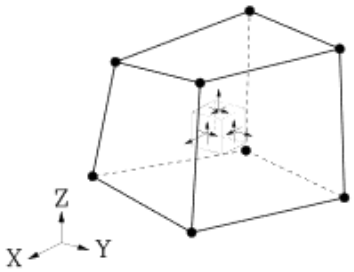

Figure 3.8: *Schematic sketch of solid element, (TNO DIANA, 2017)*

The following type of element is generally used to describe the shear failure and the ability in describing the bending failure is dependent on the number of integration points, i.e. when a solid element with a low order of integration points is used, it cannot be a reliable choice in describing the bending behaviour. On the other hand, by increasing the number of integration points, it can interpret the bending behaviour, but it makes it very inefficient from the computational point of view (Plos, 1996).
In solid elements, there is no rotational degree of freedom, and the nodes have only translational displacements in the local element directions, which is presented in Figure 3.9.

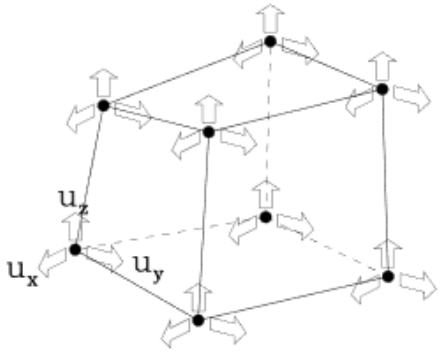

Figure 3.9: *Displacements of a solid element, (TNO DIANA, 2017)*

Considering the load types, solid elements may be loaded by a concentrated load, distributed load, volumetric load acting on the entire element, strain load, temperature as well as initial stresses (TNO DIANA, 2017).

3.4 Numerical models

In this master's thesis, several models have been studied, using the multi-purpose finite element (FE) software, DIANA 10.2.

3.4.1 Notched beam model

The studied beam in this project is the notched three-point bending test according to (EN 14651, 2005) with material properties of SFRC mix according to Table 3.6, Table 3.7 and Table 3.8. The mentioned beam is supported by steel bearing rollers on both sides, which means the translations of the nodes under the steel plate are fixed in the vertical direction as well as along the roller, but it is free to move along the beam (rolling direction). The load is applied as a prescribed vertical deformation on the top part of the beam, in the middle, by means of a steel loading plate. In order to apply the prescribed vertical deformation in DIANA, the translation of the top edge of the loading plate have been restrained in y-direction (Figure 3.11) (TNO DIANA, 2019). Moreover, the mentioned loading plate has been restrained in x-direction (Figure 3.11) (TNO DIANA, 2019).
Interface elements have been modelled between the steel elements (support and loading plate) and the concrete beam (Figure 3.11). The interface elements have been modelled as two-dimensional (2D) interface elements, based on a material model of linear elasticity (TNO DIANA, 2019; TNO DIANA, 2018). Furthermore, two types of interface element stiffnesses have been assigned; the normal stiffness has been assigned to be the average elastic modulus of the surrounded materials, divided by the structural characteristic length (l_{cs}), whereas the tangential stiffness is equivalent to the normal one divided by ten (TNO DIANA, 2019).
The element type has been chosen to be a linear plane stress element with quadratic mesh type and linear mesh order (Q8OME). Hence, the structural characteristic length (l_{cs}) is equivalent to $\sqrt{2A_{el}}$ (Rots, 1998), where A_{el} is the area of one element. In order to assure that the crack will localize in one element row above the notch, the mesh size has been chosen to be equivalent to the notch width, as illustrated in Figure 3.10.
Regarding the solving procedure of the non-linear equilibrium equations, regular Newton-Raphson iterative method has been used, since it is the most efficient method in solving non-linear equations, i.e. the convergence rate is much better than other available methods (Ebelechukwu, et al., 2018). Energy and force convergence approaches have been chosen with a tolerance of 0.001 and 0.01, respectively, for the iterative method to increase the accuracy in non-linear analysis. Moreover, to achieve high compatibility between FEA and experimental results, the loading steps has been chosen to be dense, as present in Table 3.1. The numerical code of this model can be seen in appendix C.1.

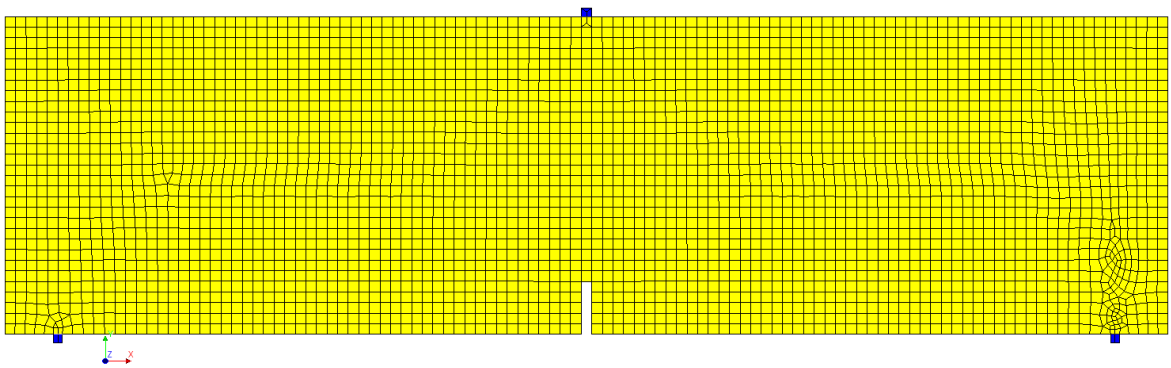

Figure 3.10: *Notched beam model with mesh size equal to notch width*

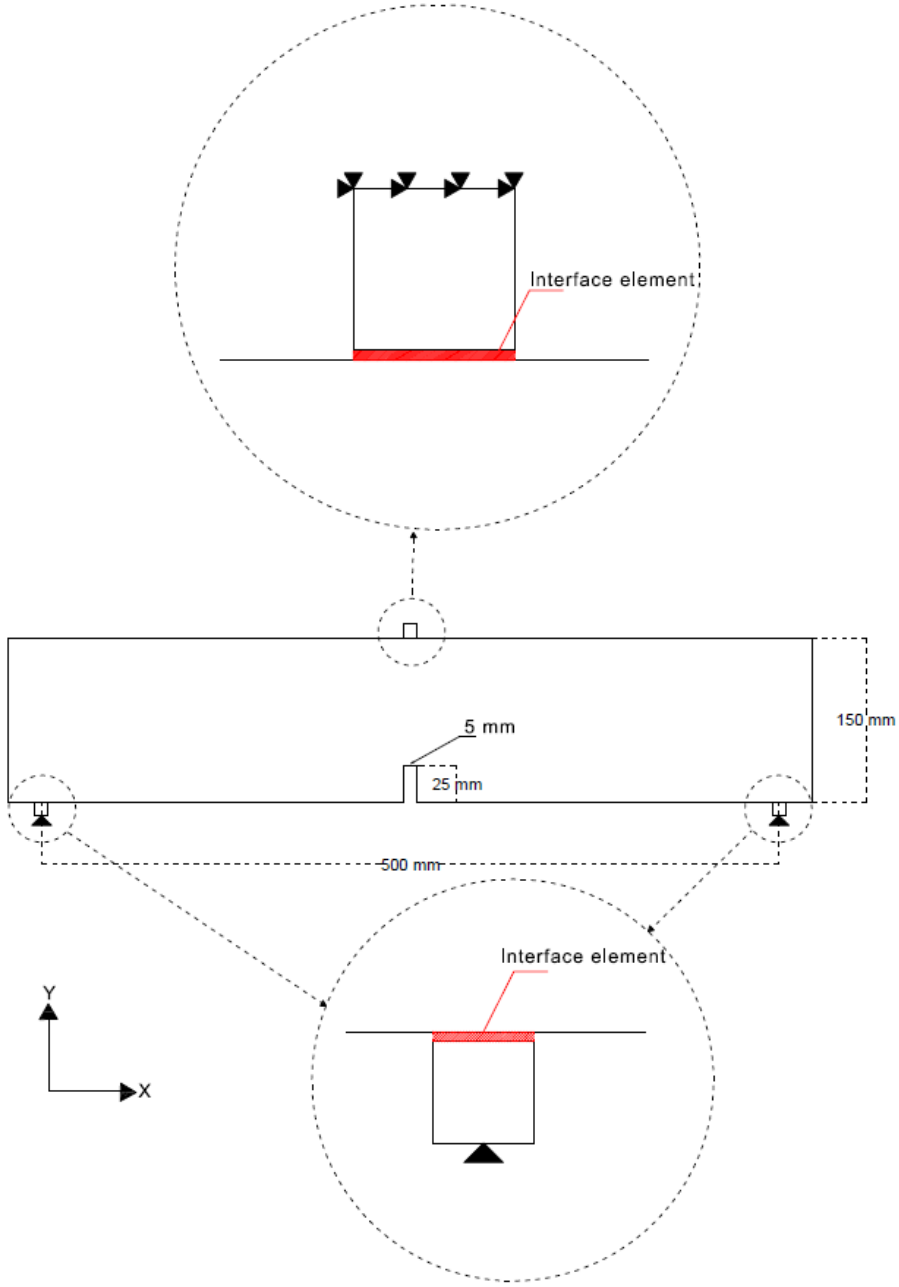

Figure 3.11: *Notched beam model*

Table 3.1: *Load step size with corresponding number of steps (Notched beam model)*

Step size [mm]	Number of steps
0.001	50
0.005	75
0.01	100
0.05	100
0.1	100
0.5	100
0.75	100
1	Until failure

3.4.2 Round panel model

The configuration and geometry of the round panel test have been chosen according to (ACI, 2004), which are illustrated in Figure 3.12 and Figure 3.13 and the dimensions are given in Table 3.2.

Table 3.2: *Geometry of the studied round panel test*

D [mm]	S [mm]	t [mm]	r [mm]
2100	2000	200	150

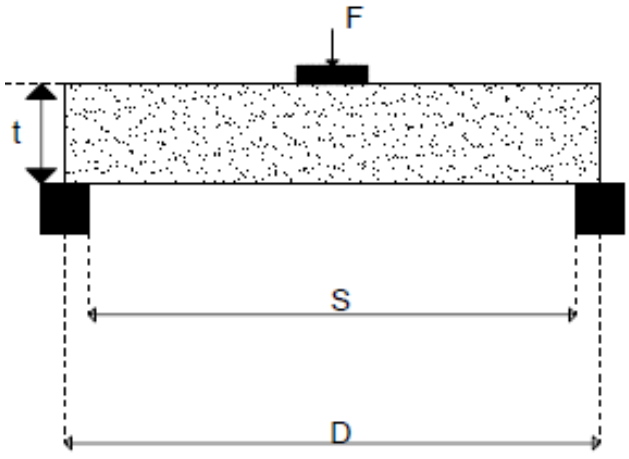

Figure 3.12: *Geometrical configuration of the round panel test (Side view)*

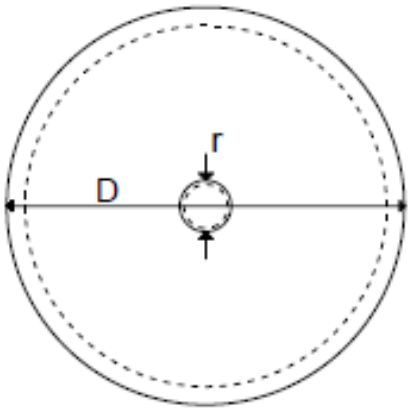

Figure 3.13: *Geometrical configuration of the round panel test (Plan view)*

3.4.2.1 Round Panel model with solid elements

The round panel is supported on steel plate, which acts as simple support and is continuous around the perimeter of the panel. In order to reduce the computation time, only a quarter of the round panel has been modelled, since it is symmetric around the centre. The boundary conditions of symmetry are depicted in Figure 3.14. Solid elements with quadratic mesh type, linear (HX24L) and quadratic (CHX60) mesh order, have been used to model the round panel, which results in different approach to calculate l_{cs}, since the structural characteristic length for solid elements is equivalent to $\sqrt[3]{V_{el}}$, where V_{el} is the volume of one element (Rots, 1998). It is highly recommended to have as much as possible equal dimensions for the solid elements since that results in a good approximation of post-cracking behaviour (Figure 3.15).
In this model, interface elements have been assigned to be between the loading plate and the round panel as well as between the continuous supporting plate and the round panel (Figure 3.14). Moreover, the type has been chosen to be three-dimensional (3D) surface interface with normal and tangential stiffnesses as it is described in 3.4.1.
On the other hand, two material models have been considered for the interface elements. The first material model is the Coulomb friction, which can describe the frictional behaviour between the round panel and the plates, at the same time this model can describe the sliding failure, i.e. it can describe the non-linear behaviour of interface elements (Shu, et al., 2015) (TNO DIANA, 2017). The aim of assigning this material model is to investigate the effect of different friction coefficients between the round panel and the continuous support, therefore, three different friction coefficients have been chosen equivalent to 0.1, 0.4 and 0.8, whereas the friction coefficient between the loading plate and the round panel has been chosen to be 0.1 (Gorst, et al., 2003). Regarding the cohesion between the continuous support and the round panel, it can exist in the real test, which depends on the material of the continuous support, for instance, a layer of Ultracal grouting and plastic membrane can be a separation layer between the round panel and the support (Destrée, 2006). Therefore, the cohesion has been chosen equivalent to $0.5\ \mathrm{N/mm^2}$ for all round panel models. Additionally, a cohesionless contact zone has been implemented to see the effect of cohesion.
The second material model for the interface elements is non-linear elasticity with no-tension; thus, the normal stiffness has been assigned as depicted in 3.4.1, whereas the tangential stiffness has been assigned to be very low (TNO DIANA, 2018). The main goal of assigning this material model is to evaluate the round panel's capacity without the effect of any

restraining, i.e. to eliminate the effect of friction coefficient on the evaluated capacity. The use of non-linear elasticity with no-tension results in allowing the round panel to be lifted up (Maekawa, et al., 2003), which means that the effect of friction coefficient will be excluded, and the model will present the case of being simply supported.
Regarding the applied load, it has been chosen to be applied by means of a loading plate with step size and number of steps as it is present in
Table 3.**3**. The load has been applied as a prescribed vertical deformation on the top face of the loading plate. Therefore, the translation of the top edge in the vertical direction has been restrained.

Table 3.3: *Load step size with corresponding number of steps (Round panel model)*

Step size [mm]	Number of steps
0.1	30
1	Until failure

By the same approach, which has been used for the notched beam, regular Newton-Raphson iterative method has been chosen as the solver tool, which is the most efficient and capable method for solving non-linear equations (Ebelechukwu, et al., 2018). Moreover, energy and force convergence approaches have been chosen with a tolerance of 0.001 and 0.01, respectively. The numerical code of this model is present in appendix C.2.

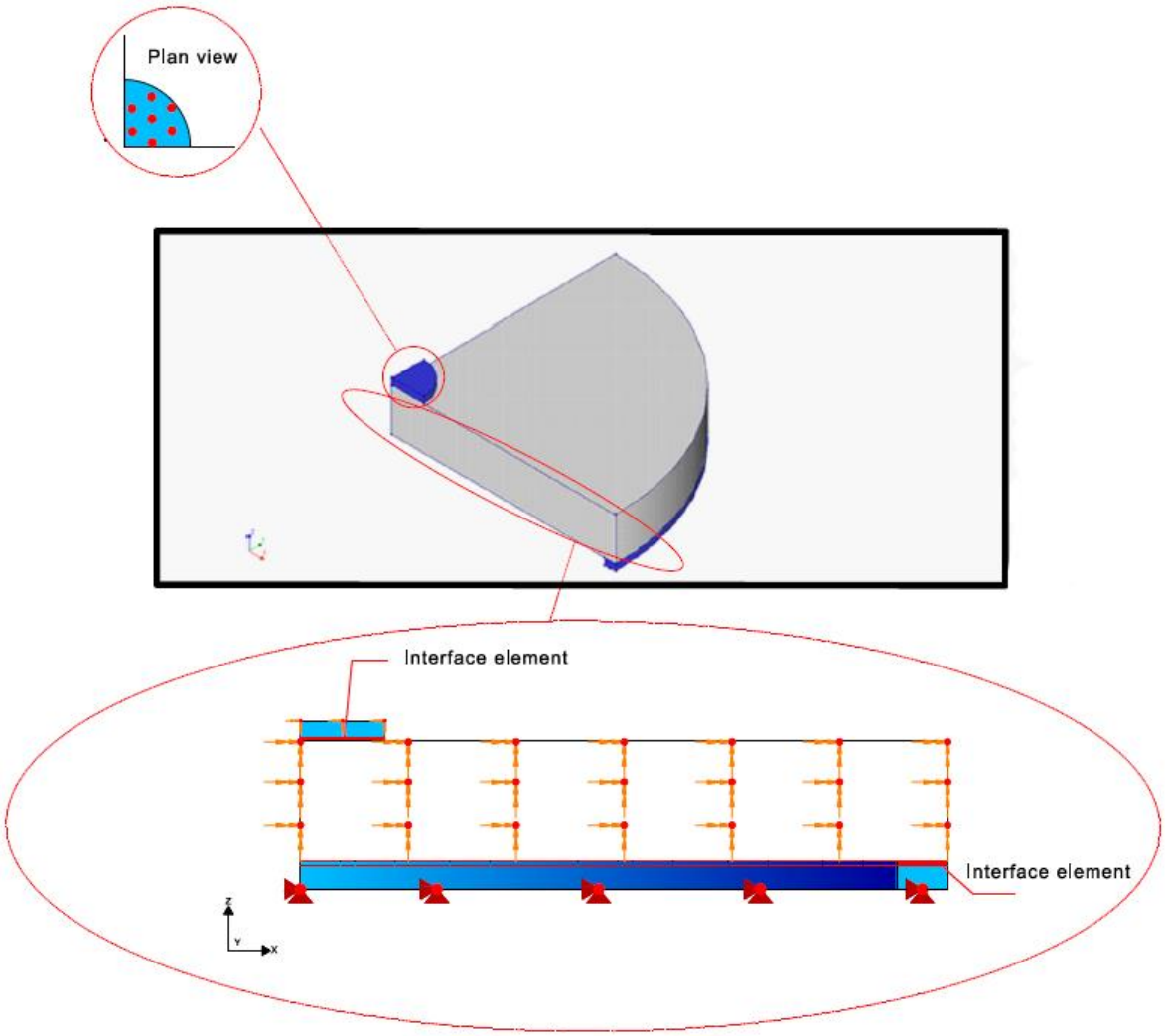

Figure 3.14: *Boundary conditions and interface elements in X-Z plane (Case of 3D round panel model)*

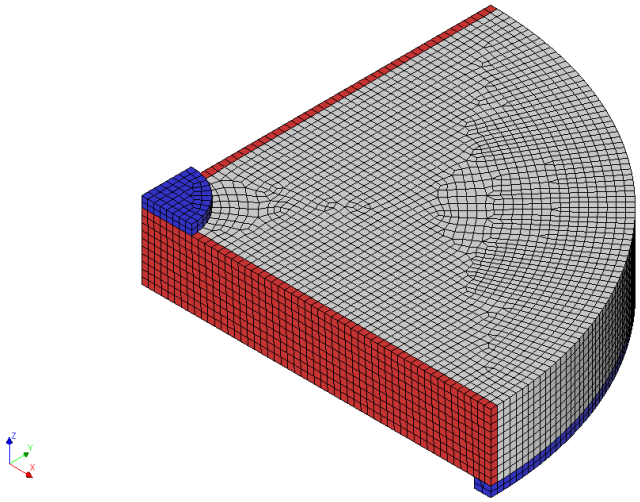

Figure 3.15: *Mesh pattern for the case of 3D round panel model*

3.4.2.2 Round panel with curved shell elements

This model is similar to the previous model of the round panel, but instead of considering solid elements, curved shell elements have been implemented with quadratic mesh type and both linear and quadratic mesh order (Q20SH, CQ40S) (Figure 3.16). Hence, the structural characteristic length for curved shell elements is equivalent to $\sqrt{2A_{el}}$ in case of linear mesh order, whereas it is equivalent to $\sqrt{A_{el}}$ in case of quadratic mesh order, where A_{el} is the area of one element (Rots, 1998). Moreover, as curved shell elements have been considered, the thickness shall be defined. Additionally, the number of thickness integration points needs to be defined, and this has been assumed to be equivalent to the maximum allowable value, which is eleven. Furthermore, the numerical integration scheme has been chosen to be regular since there are few triangular elements, which are not compatible with the high scheme. The boundary conditions of symmetry are depicted in Figure 3.17.
Moreover, boundary interface elements with the type of 3D line interface between shells, have been assigned for the contact zone between the continuous support and the round panel. The material model of boundary interface elements is based on non-linear elasticity with no-tension. Additionally, the normal stiffness has been assigned as it is described in 3.4.1, whereas the tangential stiffness is very low (TNO DIANA, 2018). Regarding the geometry of boundary interface elements, the thickness has been assumed to be 1 mm, the shape definition type is flat, the direction vector is parallel to the shell plane and the local y-axis of boundary interface elements is in the direction of the negative global z-axis. The local y-axis of boundary interface elements has been assigned in this way to assure that the round panel is resting on the continuous support, not hanging (Figure 3.17). Hence, the normal stiffness is assigned in the direction of the local y-axis of the boundary interface elements (TNO DIANA, 2018).
Regarding the applied load, it has been chosen to be applied by means of a loading plate (With solid elements) with step size and number of steps as it is present in Table 3.3. The iterative method and the convergence approaches have been chosen as depicted in 3.4.2.1.

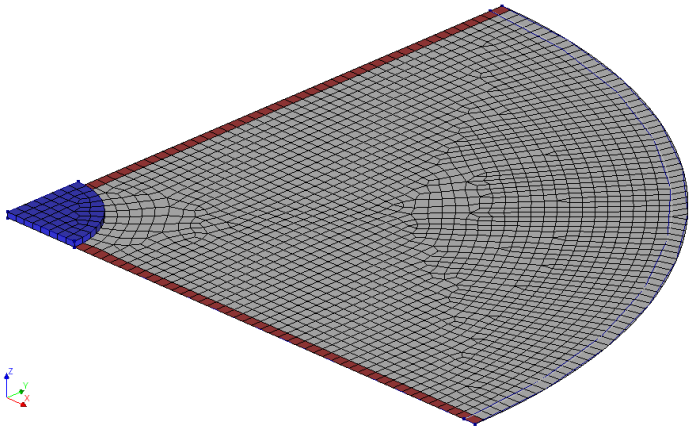

Figure 3.16: *Mesh pattern for case of 2D round panel model*

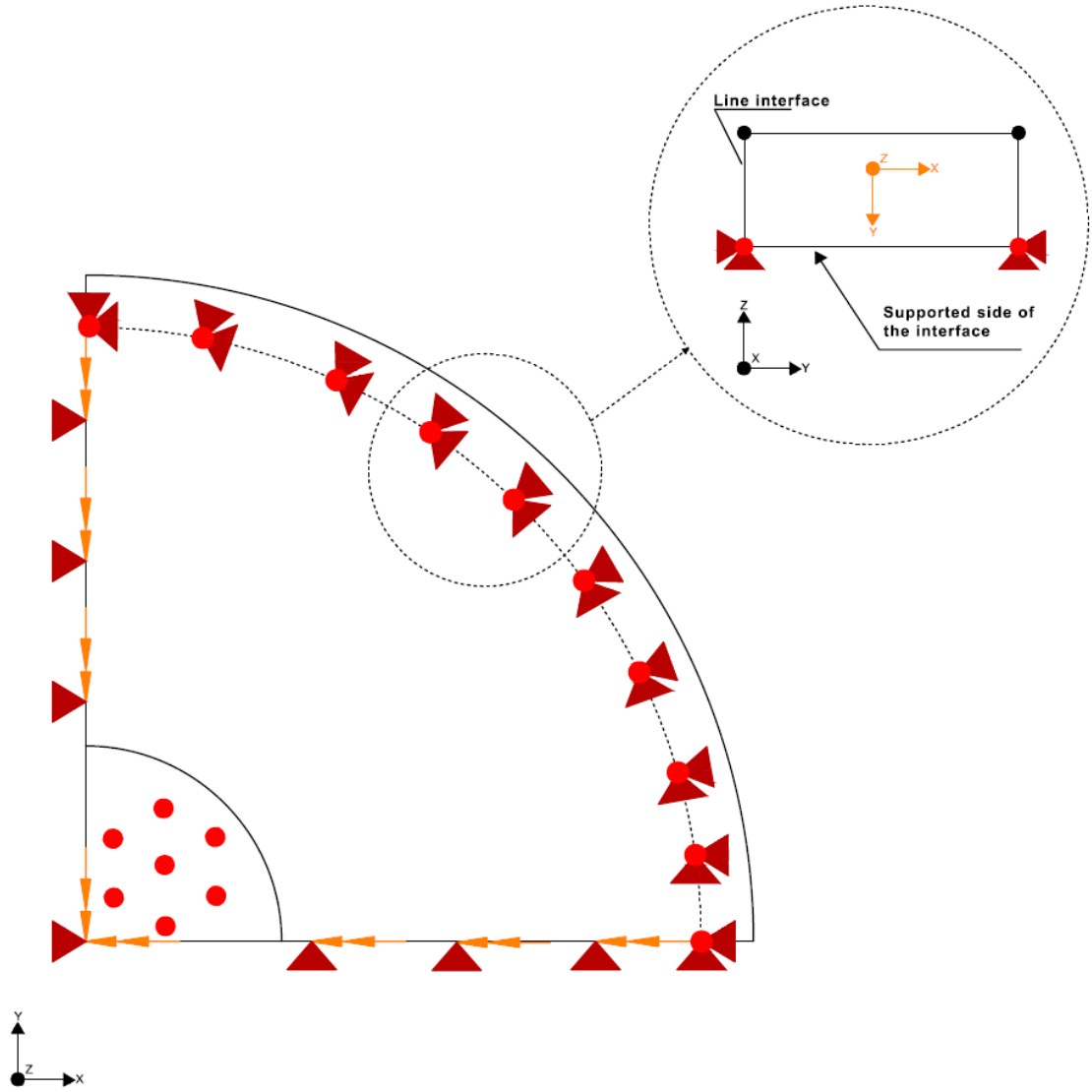

Figure 3.17: *Boundary condition for symmetry and interface element (case of 2D round panel model)*

3.4.3 Slab model

The studied slab is an industrial pile-supported SFRC floor, and the geometry of this slab is as illustrated in Figure 3.18 (Silfwerbrand, 2017). A section of this slab can be seen in Figure 3.19, which represents a typical design of SFRC pile-supported slabs. It can be noticed from the section of this slab (Figure 3.19) that every pile has a pile cap and over each pile cap there is a drop panel, which have been implemented to increase the shear strength of the slab, i.e. the drop panel and pile cap prevents the punching shear failure. Since one of the aims of this master's thesis is to investigate the structural behaviour of interior SFRC slab, the edges of this slab have been extended in two directions to see the effect of the negative moment over the supporting pile. Furthermore, the interior slab is symmetric around two directions (x-axis and y-axis), therefore to reduce the computation time, only a quarter of this interior slab with its extension has been modelled. The resulted modelled part and the boundary conditions of symmetry can be seen in Figure 3.18 and Figure 3.21.

By the same approach as for the round panel, solid elements have been considered, which results in l_{cs} that is equivalent to $\sqrt[3]{V_{el}}$. In this model, the mesh type and the mesh order are quadratic (CHX60) (Figure 3.22). In addition, the previous recommendation of choosing as much as possible equal dimensions for the solid elements shall be followed as well.
Interface elements have been assigned to be between the pile cap and the slab. Since the slab is resting on the pile cap and there is a separating polyethylene sheet between the slab and the pile cap (Figure 3.19), 3D surface interface elements with normal and tangential stiffnesses have been assigned to the contact zone between the pile cap and the slab (Figure 3.20). The values of normal and tangential stiffnesses have been chosen as it is depicted in 3.4.1. Moreover, Coulomb friction has been chosen as a material model for the interface elements. In order to simulate the real connection between the pile cap and the slab, the friction angle and cohesion have been chosen to be 17 degrees and 1.83 kPa ($0.00183\ \mathrm{N/mm^2}$), respectively as it is recommended in (Cen, et al., 2018).
Since the slab will be analysed under two types of load, point load and uniformly distributed load, two load cases have been assigned. It should be noticed that in case of uniformly distributed load, the dead-load has not been assigned separately, i.e. the evaluated failure load, includes the dead-load as well. On the other hand, for the case of point load, a loading plate with dimensions of 150×150 mm has been modelled to apply the load in the centre (mid-span) of the slab. The dimensions of this loading plate represent only a quarter of the real loading plate, which has dimensions of 300 ×300 mm. The loading plate has been considered as a steel plate; therefore, 3D surface interface elements with a material model of Coulomb friction have been chosen. The friction coefficient and cohesion for the interface elements between the loading plate and the slab have been selected to be 0.1 and as small as possible, respectively.
Not only, but also to apply the load in case of point load, a prescribed deformation over the loading plate has been assigned with the load step increment as mentioned in Table 3.4. It should be noted that in order to apply the point load by means of prescribed deformation, the upper face of the loading plate shall be restrained in the vertical direction, which is illustrated in Figure 3.21. Furthermore, for the case of distributed load, the load step increment has been considered as it is present in Table 3.5.

Table 3.4: *Load step size with corresponding number of steps (Slab model with point load)*

Step size [mm]	Number of steps
0.01	10
0.1	30
10	Until failure

Table 3.5: *Load step size with corresponding number of steps (Slab model with uniformly distributed load)*

Step size [$\mathrm{kN/m^2}$]	Number of steps
0.5	100
2.5	Until failure

Finally, by the same approach as for the notched beam and the round panel, regular Newton-Raphson iterative method has been chosen as the solver tool as well as energy and force convergence approaches have been considered with a tolerance of 0.001 and 0.01, respectively. The numerical codes of these two models are present in appendices C.3 and C.4.

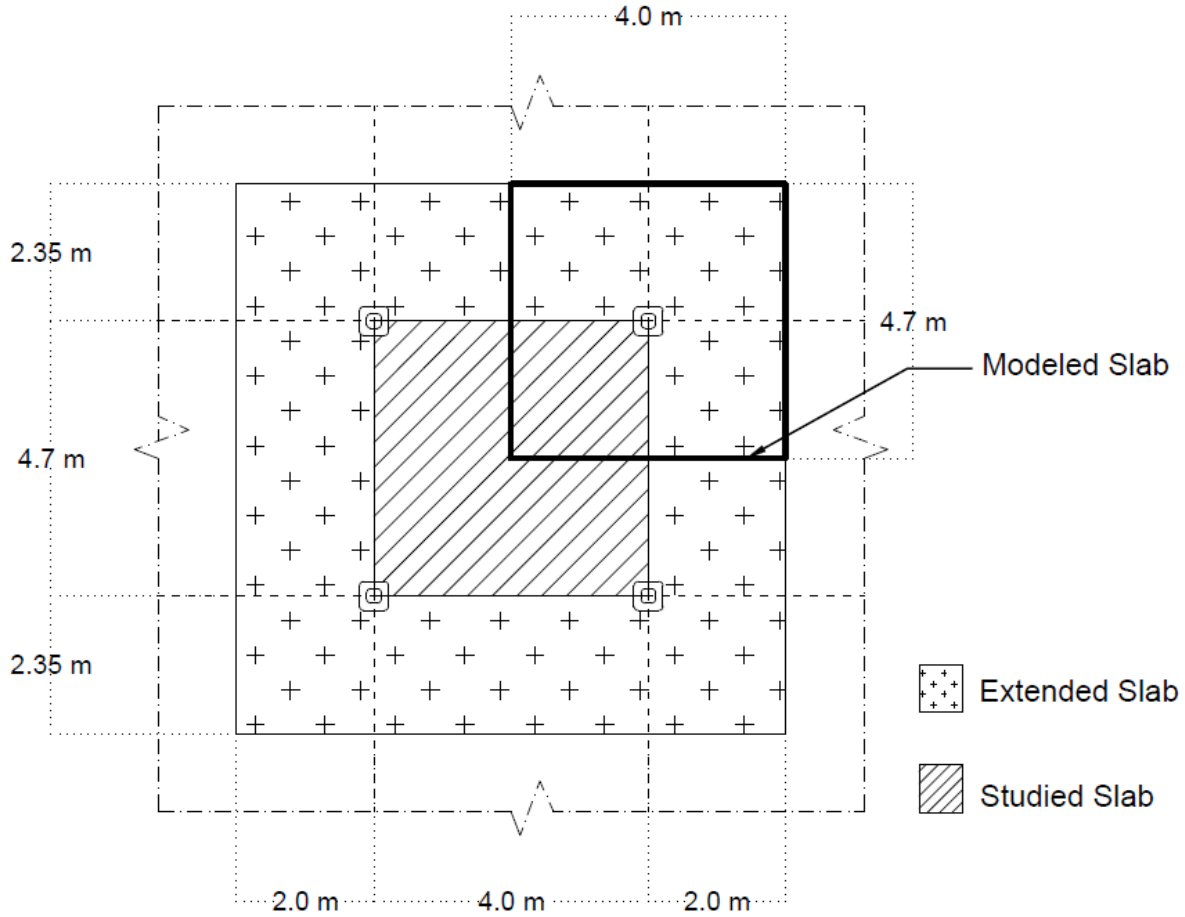

Figure 3.18: *Geometry of the studied and modelled slab*

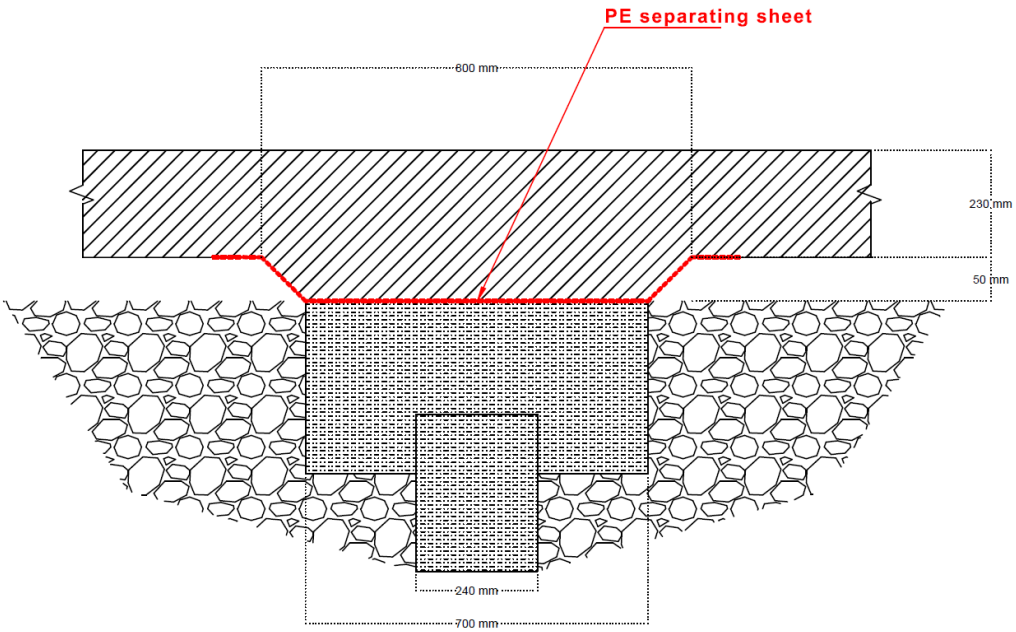

Figure 3.19: *Section view for the slab, over the support*

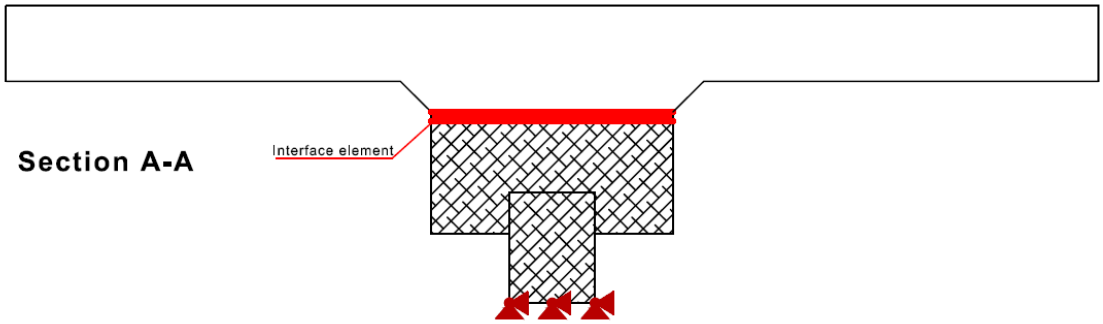

Figure 3.20: *Section A-A of the modelled slab*

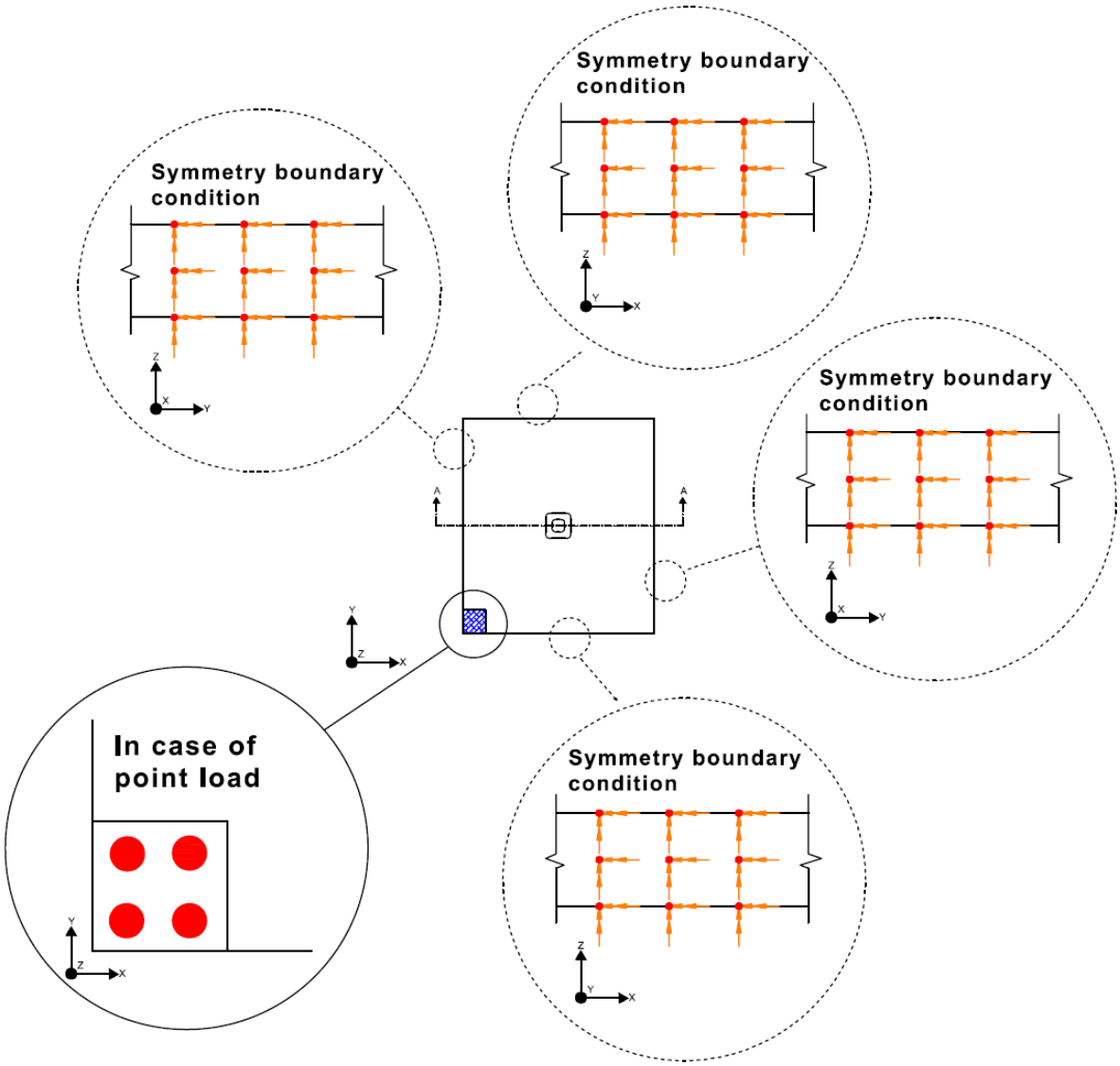

Figure 3.21: *Boundary conditions for the modelled slab*

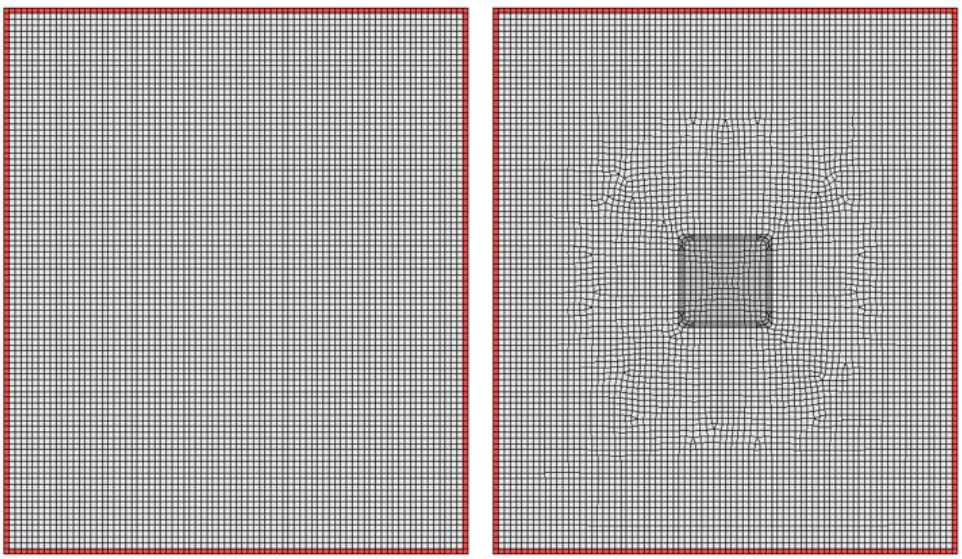

Figure 3.22: *Mesh pattern from top (left) and bottom (right)*

3.5 Concrete model

3.5.1 General

One concrete mix has been considered in the project at hand. The compositions of this concrete are present in Table 3.6 (Löfgren, 2005). This concrete has undergone different tests such as a test for the compressive strength and three-point bending test (EN 14651, 2005), which have been carried out by (Löfgren, 2005). The results are present in Table 3.6 and Table 3.7.

Table 3.6: *SFRC mix compositions, (Löfgren, 2005)*

Constitutes	Density [kg/m^3]	SFRC Mix [kg/m^3]
CEM II/A-LL 52.5 R	3100	360
Fly ash	2250	100
Water	1000	172
Equivalent w/b ratio	-	0.42
Superplasticizer-SIKA ViscoCrete 34	1090	0.4
Aggregates ($00-04$ mm)	2535	745.4
Aggregates ($04-08$ mm)	2642	313.3
Aggregates ($08-16$ mm)	2637	635
Fibre, V_f	7800	0.5%
Steel – Dramix© (65/60)		1.0
(Aspect ratio/Length)	-	(65/60)
Measured air content	-	1.4%

Table 3.7: *Properties of SFRC mix, (Löfgren, 2005)*

Concrete class	Density [kg/m^3]	$f_{c,cyl}$ [MPa]	E_{ci} [GPa]	ν [-]
C40/50	2384	49.1	35.5	0.2

Table 3.8: *Tensile strength and flexural-tensile strengths of SFRC mix, (Löfgren, 2005)*

Stages	Stress [MPa]	CMOD [mm]
f_{ct}	3.62	-
$f_{R,1}$	5.56	0.5
$f_{R,2}$	6.22	1.5
$f_{R,3}$	5.89	2.5
$f_{R,4}$	5.31	3.5
$f_{R,5}$	5.08	4.0

3.5.2 Compressive behaviour

In order to simulate the compressive behaviour of SFRC, a material model needs to be implemented. In this work, compressive behaviour of SFRC is not a significantly important issue, since there is no conventional reinforcement. This means that SFRC will likely fail in tension before failing in compression, where at the stage of failure, the behaviour of SFRC will be almost linear behaviour. The fib Model Code 2010 suggests considering SFRC as ordinary concrete in compression, where the uniaxial compressive stress-strain response has a parabolic shape (fib, 2013). On the other hand, some researches have shown that for concrete with compressive strength of more than 40 MPa, Thorenfeldt as a material model is more suitable (Vecchio & Collins, 1993), (Burgers, 2006). Therefore, in this project, the concrete has been modelled based on the total strain rotating crack model with a material model of Thorenfeldt (Figure 3.23). In addition, the influence of lateral cracking has not been considered.

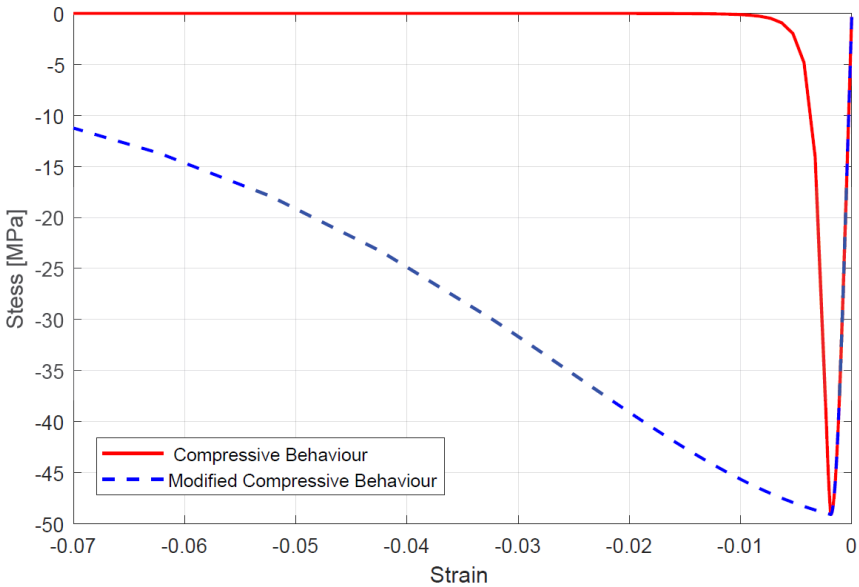

Figure 3.23: *Modification of Thorenfeldt material model (Model of one element under pure compression, extracted from DIANA)*

The material model of Thorenfeldt is described by the following equations (Thorenfeldt, et al., 1987), (TNO DIANA, 2017).

$$\sigma_c = f_{ct}\left(\frac{\varepsilon}{\varepsilon_c}\right).\left(\frac{n}{n-1+\left(\frac{\varepsilon}{\varepsilon_c}\right)^{n.k}}\right) \qquad (3.5.1)$$

$$n = 0.8 + \frac{f_{ct}}{17} \qquad (3.5.2)$$

$$k = \begin{cases} 1 & if\ 0 < \varepsilon < \varepsilon_c \\ 0.67 + \frac{f_{ct}}{62} & if\ \varepsilon > \varepsilon_c \end{cases} \qquad (3.5.3)$$

Where, σ_c and ε are the stress and strain of the concrete, f_{ct} is the compressive strength, and ε_c is the strain at maximum stress.

The material model of Thorenfeldt is mesh-dependent as well as specimen size-dependent; therefore, the stress-strain curve of Thorenfeldt has been calibrated to fit an experimental cylindrical test with a length of 300 mm. Additionally, for FEA, the stress-strain curve must be modified for the element size (Figure 3.23), (Zandi, et al., 2007). Hence, these calibration and modification have been implemented by multiplying the plastic strain by a ratio of $300\ \text{mm}/l_{cs}$ (Zandi, et al., 2007). Furthermore, the crack bandwidth has been considered equivalent to l_{cs}, since there is no conventional reinforcement.

3.5.3 Tensile and post-cracking behaviour

Another property that needs to be considered is the post-cracking behaviour of SFRC for which there are several approaches available such as, RILEM TC162-TDF, Spanish guidelines as well as fib model code 2010. The constitutive model based on RILEM (RILEM-TC-162-TDF, 2003) exhibited a significant discrepancy from experimental results for small displacement, whereas the results are more accurate in case of large displacement (Blanco, et al., 2013). Furthermore, Spanish design guideline (EHE-08, 2008) as well as fib model code 2010 (fib, 2013) have displayed a satisfactory prediction of a tensile constitutive model for both large and small displacements. It can be deduced that for SLS, where deflections and crack widths are small, all mentioned methods are suitable, whereas, in case of ULS, which concerns about large deflections, RILEM and fib model code 2010 are more accurate (Blanco, et al., 2013). However, in case of SFRC, a more idealistic approach has been used in recent years, which is the inverse analysis. Since the SFRC is a complex system and the behaviour in tension differs between different mixes, the inverse analysis approach is more accurate and realistic, when it comes to FEA. Therefore, an inverse analysis, which has been carried out on the studied SFRC (Jepsen, et al., 2018), has been used first. Since this inverse analysis has shown a bit overestimation, more adjustment has been implemented by studying the effect of changing many parameters such as the crack opening and the tensile stress, which represented in (Stephen, et al., 2019). The resulted stress-crack opening curve and its values can be seen in Table 3.9 Figure 3.24. Moreover, a material of plain concrete has been assigned to compare the flexural tensile behaviour of SFRC and plain concrete. The tensile behaviour of plain

concrete can be derived by not considering the effect of steel fibres in the post-cracking behaviour as it is illustrated in Table 3.10. In addition, it is beneficial to pay attention to the crack bandwidth value, since the choice of crack bandwidth can affect the results to some extent. However, in this project, all the models have a crack bandwidth equal to l_{cs}, since there is no conventional reinforcement. For the elements at symmetry surfaces, the material has been adjusted to have half fracture energy, i.e. the crack bandwidth is doubled (Jirásek & Bauer, 2012).

Table 3.9: *Tensile behaviour of the modelled SFRC based on crack width-tensile stress*

Crack width [mm]	Tensile stress [MPa]
-	0
-	3.52
0.035	2.05
0.054	1.65
0.1	1.79
0.25	1.92
0.6	2.02
1.0	2.10
1.25	2.17
1.5	2.30
2.5	1.80
5	1.04
20	0

Table 3.10: *Tensile behaviour of the modelled plain concrete based on crack width-tensile stress*

Crack width [mm]	Tensile stress [MPa]
-	0
-	3.52
0.035	2.05
0.084	0

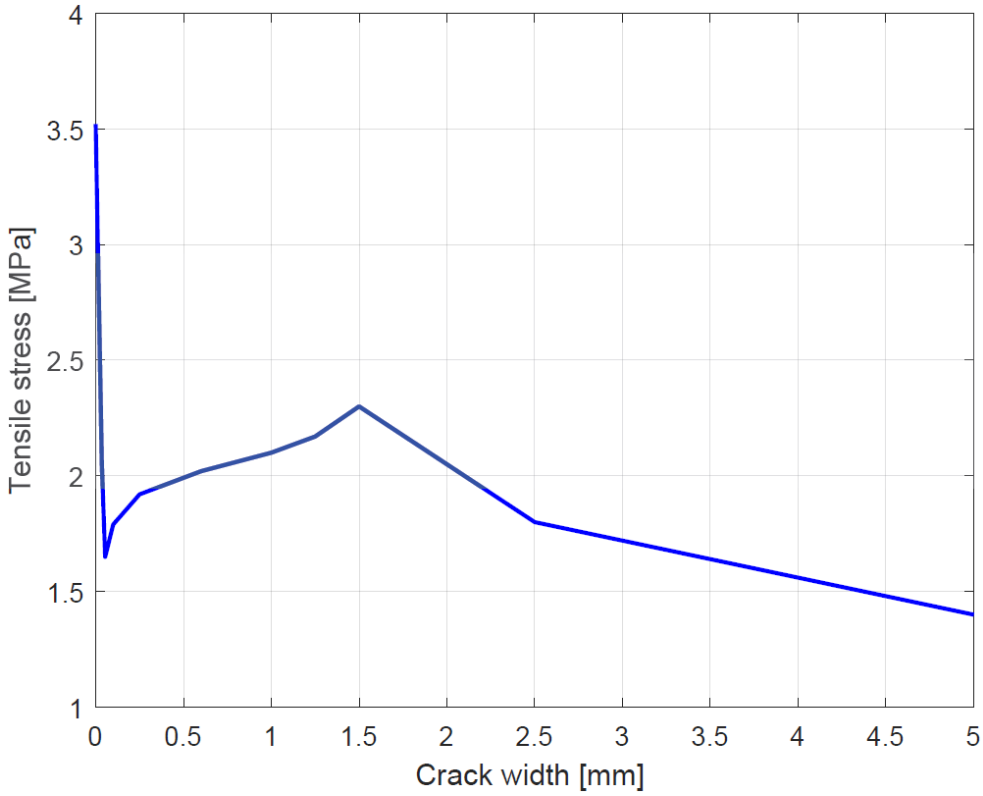

Figure 3.24: *Tensile constitutive model for studied SFRC mix*

4 Discussion of results

4.1 Notched beam

4.1.1 Material response verification

The main aim of analysing the notched three-point bending beam was to derive and verify the tensile material response. For this purpose, an appropriate inverse analysis based on AIA has been carried out. In Figure 4.1, a comparison between the implemented inverse analysis in Diana model and the experimental data is shown.

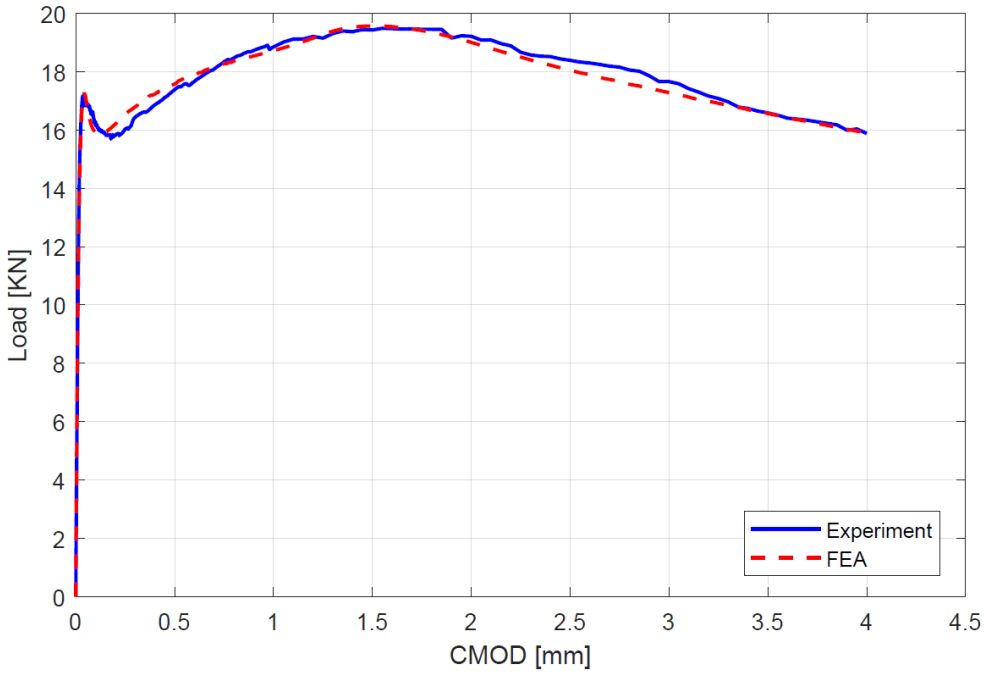

Figure 4.1: *Inverse analysis of multilinear σ-ε relationship*

The appropriate mesh size has been chosen to be equivalent to the notch width, which is 5 mm. In Figure 4.2, it can be noticed that the cracks are localized in one element row, which dedicates that the behaviour of the beam is governed by the element row above the notch. Therefore, it can be deduced that in case of notched three-point bending model, there is no difference between implementing the smeared crack approach or the discrete crack approach.

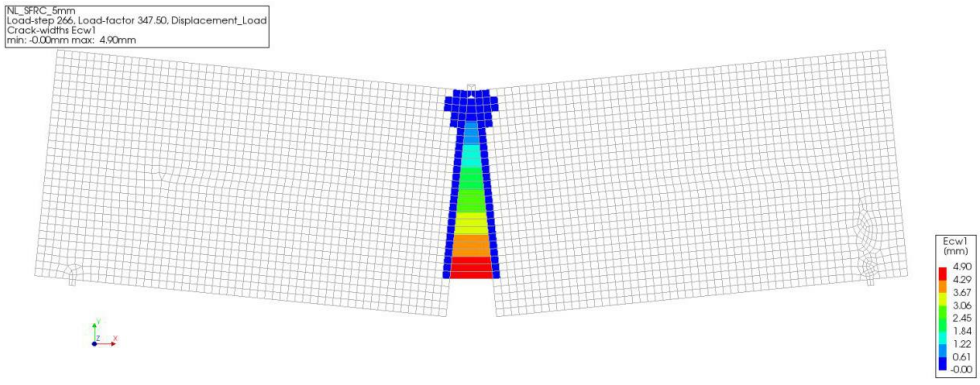

Figure 4.2: *Crack localization in one element row*

4.1.2 Comparison between SFRC and Plain concrete

The difference between SFRC and plain concrete is only in the post cracking behaviour, i.e. SFRC exhibits a more ductile behaviour (more energy dissipation) due to the presence of steel fibres. The following fact can be verified by Figure 4.3, which displays that the fracture energy of plain concrete is incomparable with that of SFRC.

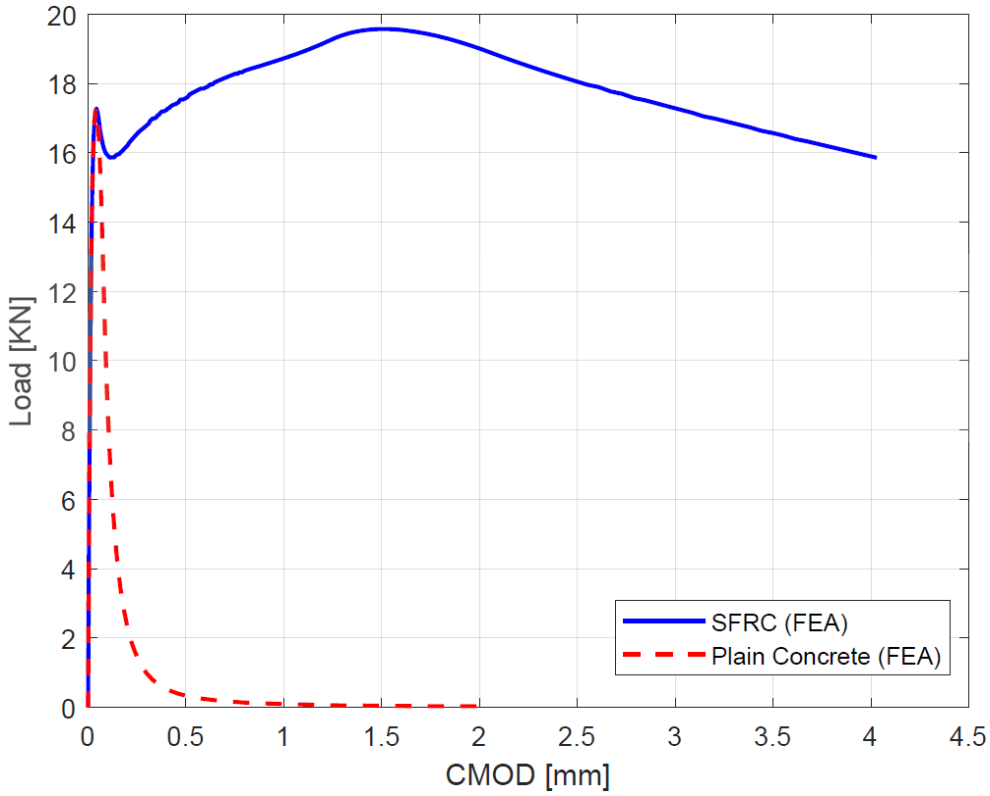

Figure 4.3: *Load versus CMOD for SFRC and plain concrete*

4.2 Round panel

4.2.1 Structural behaviour evaluation

The results of analysing the round panel model with different friction coefficients show that the higher the friction between the support and the round panel, the more post-cracking capacity can be expected. It is also obvious that the effect of friction coefficient is almost negligible in the elastic state (uncracked state), whereas the initial peak load (beyond the elastic state) displays a dependency on the friction coefficient, i.e. the load at cracking increases as the friction coefficient increases (Figure 4.4). Moreover, it can be realised that as the friction coefficient increases, the post-cracking capacity is reached for a smaller deflection.

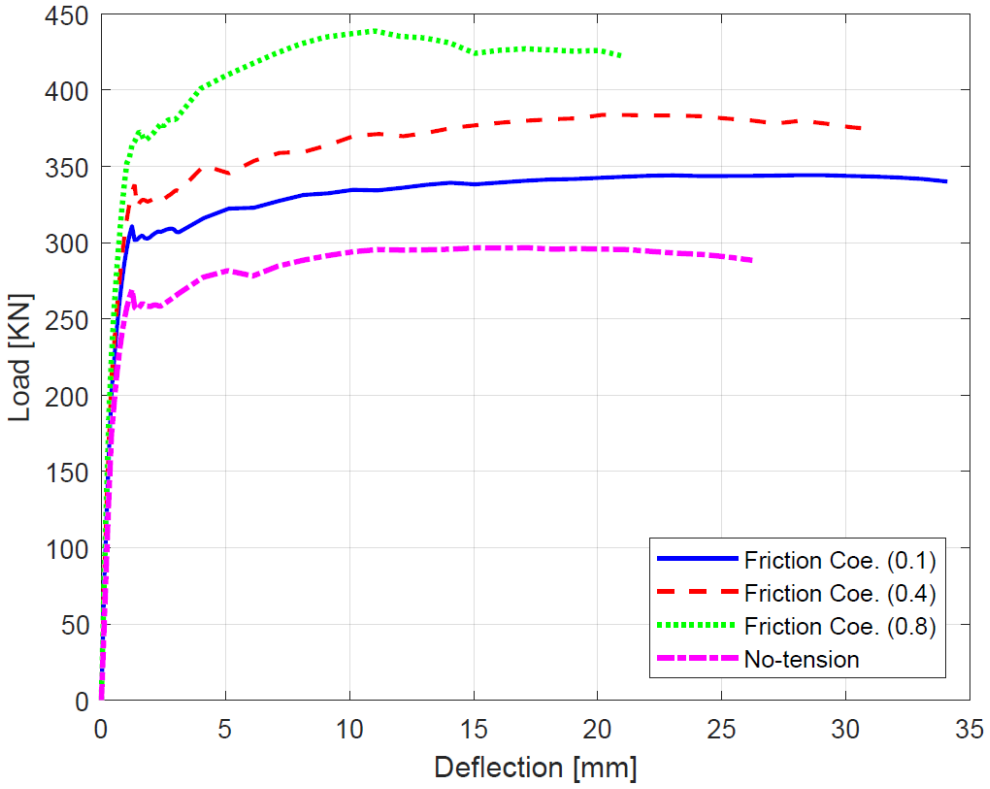

Figure 4.4: *load versus deflection for the case of round panel without friction coefficient and with different friction coefficients*

Table 4.1 compares the results from FEA of round panels without friction coefficient and with different friction coefficients of 0.1, 0.2 and 0.4. It can be realised from the table that the presence of friction forces increases the post-cracking capacity and when the friction coefficient is 0.1, 0.4 and 0.8, the post-cracking capacity increased by 16 per cent, 29 per cent and 48 per cent, respectively. This increase in the post-cracking capacity stems from the fact that the round panel is more restrained since the friction coefficient is higher. Obviously, it can be supported by the fact that since the round panel becomes more restrained, more capacity can be obtained due to arching action.

Table 4.1: *Effect of friction coefficient on the structural behaviour of round panel*

Friction Coefficient	Post-cracking capacity [kN]	Increment parentage [%]
Frictionless	296.6	-
0.1	344.2	16
0.4	383.7	29
0.8	438.7	48

Figure 4.5 and Table 4.2 show to which extent can cohesion affect the structural behaviour and the post-cracking capacity of the round panel.

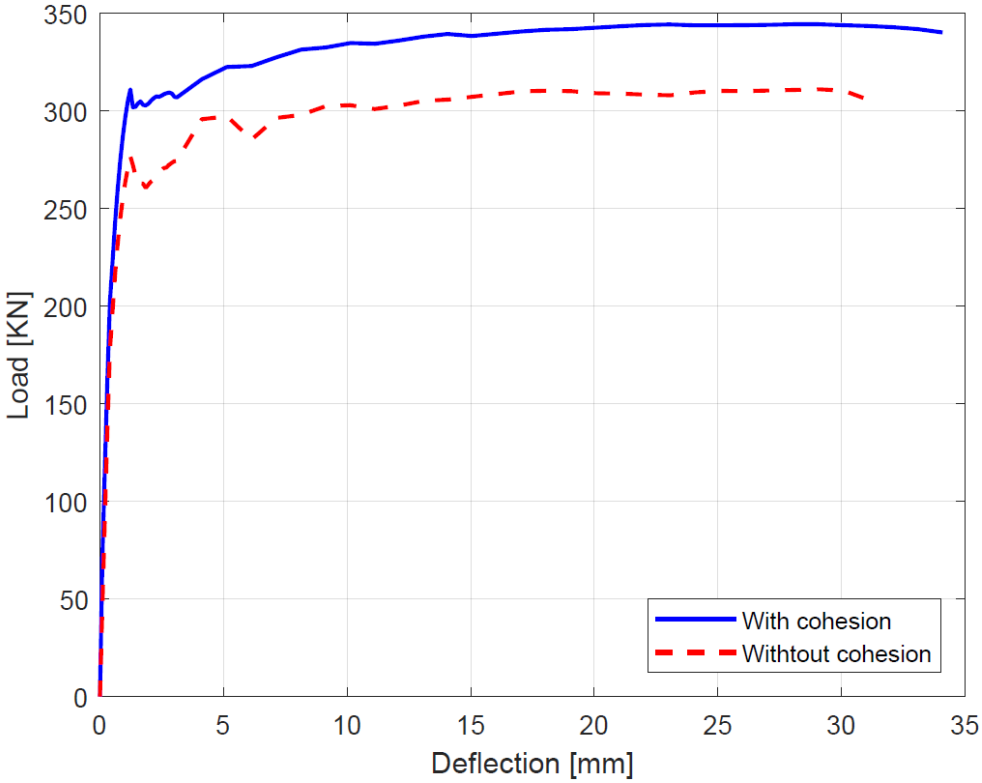

Figure 4.5: *Effect of cohesion on the structural behaviour of round panel (frictional contact zone with friction coefficient of 0.1)*

Table 4.2: *Effect of cohesion on the structural behaviour of round panel (frictional contact zone with friction coefficient of 0.1)*

Post-cracking capacity with cohesive contact zone [kN]	Post-cracking capacity with cohesionless contact zone [kN]	Difference [%]
344.2	310.9	10.6

The round panel model with no-tension interface elements has been implemented to conduct a comparison between the capacities, which are obtained from the FEA and calculation based on YLT. Table 4.3 displays the difference between the obtained capacities from FEA and hand calculation (see appendix B.1). This discrepancy springs from the fact that the hand-calculated capacity is based on the rigid tensile constitutive model, which is somewhat conservative, whereas the modelled tensile behaviour in FEA is based on AIA, which represents the actual behaviour.

Table 4.3: *Hand-calculated capacity versus capacity calculated from FEA for round panel model (frictionless contact zone)*

FEA post-cracking capacity [kN]	Hand-calculated post-cracking capacity [kN]	Difference [%]
296.6	279.8	6.0

Furthermore, a comparison of the structural behaviour of the round panel with two different element types (solid and curved shell elements) has been carried out where the contact zone is frictionless. This comparison displays that the use of curved shell elements results in increasing

the maximum elastic tensile load. Additionally, the implementation of curved shell elements induces a slight increase in the post-cracking capacity, for smaller of deflections but a lower capacity for larger deflections (see Figure 4.6).

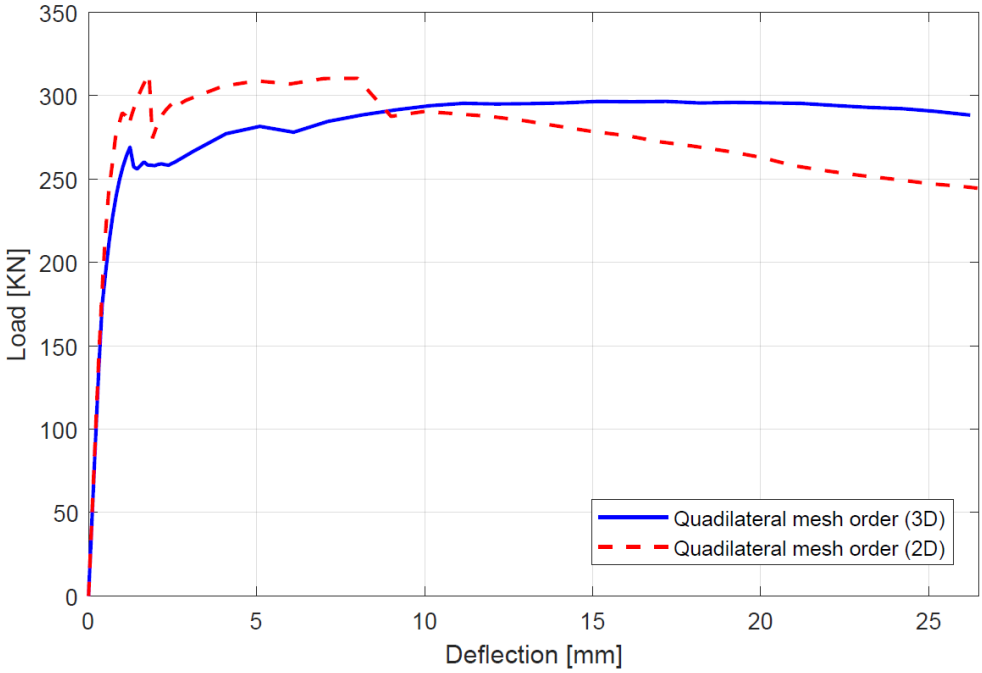

Figure 4.6: *Effect of element type on the structural behaviour of round panel (frictionless contact zone)*

In this work, the effect of mesh order has been investigated to show how the mesh order affects the structural behaviour of the round panel. Therefore, two types of mesh orders (linear and quadrilateral) have been considered for both 2D and 3D models without friction coefficient. The results show that the effect of mesh order is more noticeable when the model is 2D, whereas it is negligible when the model is 3D model. However, the effect of mesh order in 2D is still small and can be ignored for the purpose of reducing the computation time.

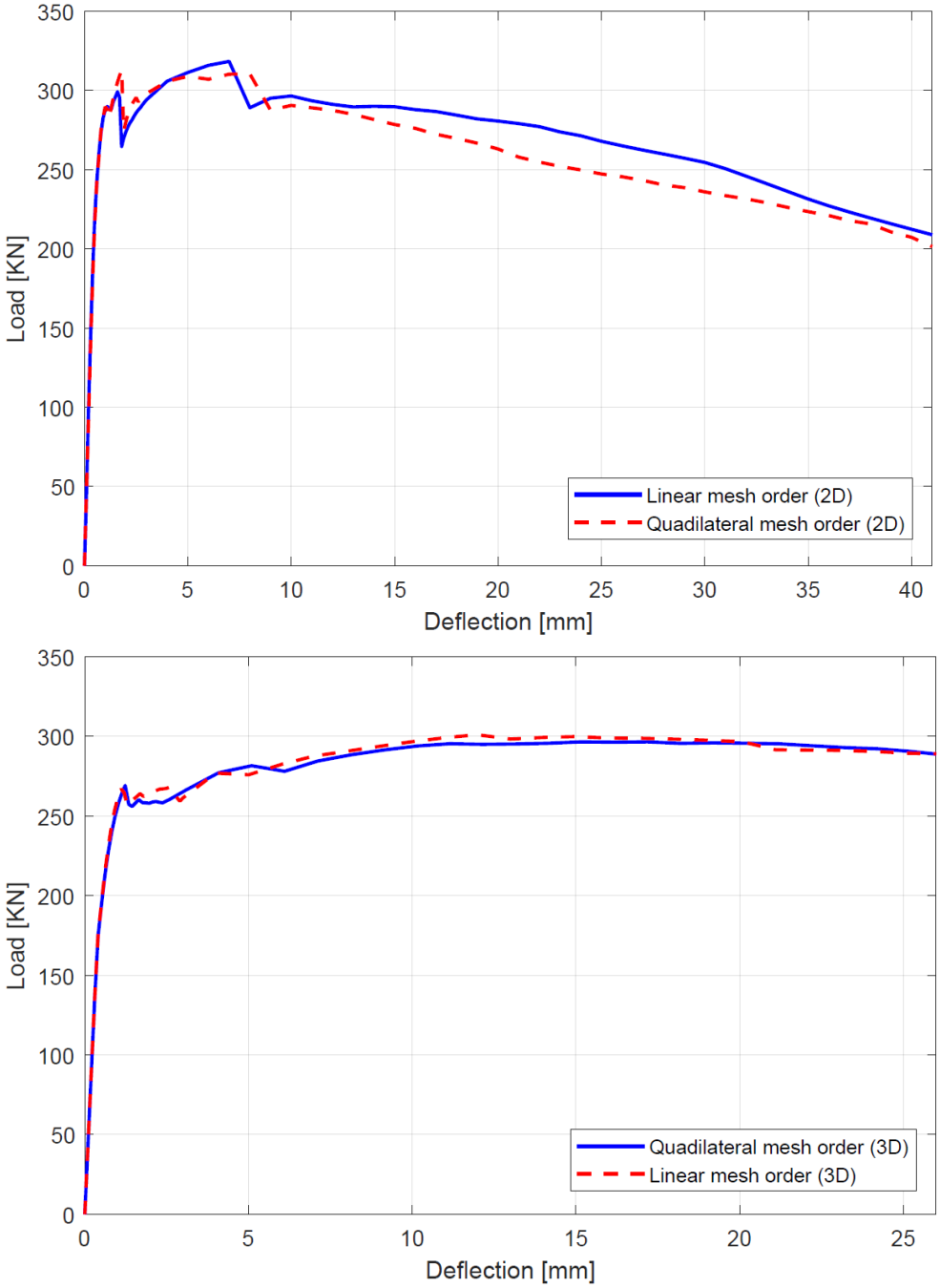

Figure 4.7: *Effect of mesh order on the structural behaviour of round panel (frictionless contact zone)*

4.2.2 Crack evaluation

The crack development in the round panel with frictionless and frictional contact zone with different friction coefficients is shown in Figure A.1, Figure A.2, Figure A.3 and Figure A.4 (in appendix A.1). It can be deduced from mentioned figures that the number of cracks increases when there is friction between the round panel and its continuous support. This increase stems from the fact that when the crack starts opening the friction forces will restrain the opening of this crack, which leads to stress the uncracked material more. This means forcing the uncracked material to be cracked, which results in an increase in the number of cracks.

Table 4.4 represents the crack width at a certain value of deflection equal to 1.6 mm (A deflection, which can be categorized in the serviceability limit state just after crack initiation) as well as the crack width when the post-cracking capacity is reached. Considering the SLS, it can be deduced that a higher friction coefficient results in a lower crack width, but the difference is very small. This small difference springs from the fact that as the radial and tangential movements are very small, the impact of friction forces will be significantly small as well. Additionally, in the stage of post-cracking capacity, the crack width decreases when the friction coefficient is increasing from 0.1 to 0.8. It should be remarked that the crack width is much smaller for the case with friction coefficient equivalent to 0.8, i.e. the overall crack width decreases but this change is more significant when the friction coefficient changes from 0.4 to 0.8. It is expected to see the decrease in crack width since when the friction coefficient is higher, the post-cracking capacity is achieved with less deflection.

Table 4.4: *Crack width in several stages for round panel test*

Friction Coefficient	Crack width at deflection 1.6 mm [mm]	Crack width at the stage of post-cracking capacity [mm]
0.1	0.06	6.79 (At deflection 28.1 mm)
0.4	0.05	6.59 (At deflection 20.2 mm)
0.8	0.04	2.57 (At deflection 11.0 mm)

4.3 Pile-supported slab

4.3.1 Pile-supported slab under uniformly distributed load

4.3.1.1 Structural behaviour evaluation

The analysis of pile-supported slab under distributed load exhibits a capacity of 144.7 kN/m^2, which is more than three times of the hand-calculated capacity (see appendix B.2) (Table 4.5). This discrepancy stems from several factors that can increase the capacity of the studied pile-supported slab. Considering that the studied panel is an interior type of panel and the edges are completely restrained against lateral movement; hence, the most decisive factor involved is the arching action phenomenon. Moreover, the second factor that causes this difference is that in the hand-calculated capacity, the material model has been chosen based on rigid tensile constitutive model (fib, 2013), i.e. a more conservative constitutive tensile model is implemented in the hand calculation. Furthermore, in the yield line theory, the effect of support condition (friction coefficient) is not included, whereas it has been considered by means of implemented interface element in FEA. Therefore, to some extent, it is expected to increase the capacity in FEA. Additionally, the effect of drop panel, which has a small contribution in increasing the flexural capacity of the slab, has not been considered in the hand-calculated capacity (although it can be considered), whereas it has been considered in FEA. Figure 4.8 illustrates the load-deflection diagram for the studied slab, which shows a sudden change in the slope, which stems from the fact that the initiation of cracks will decrease the stiffness gradually until reaching its capacity.

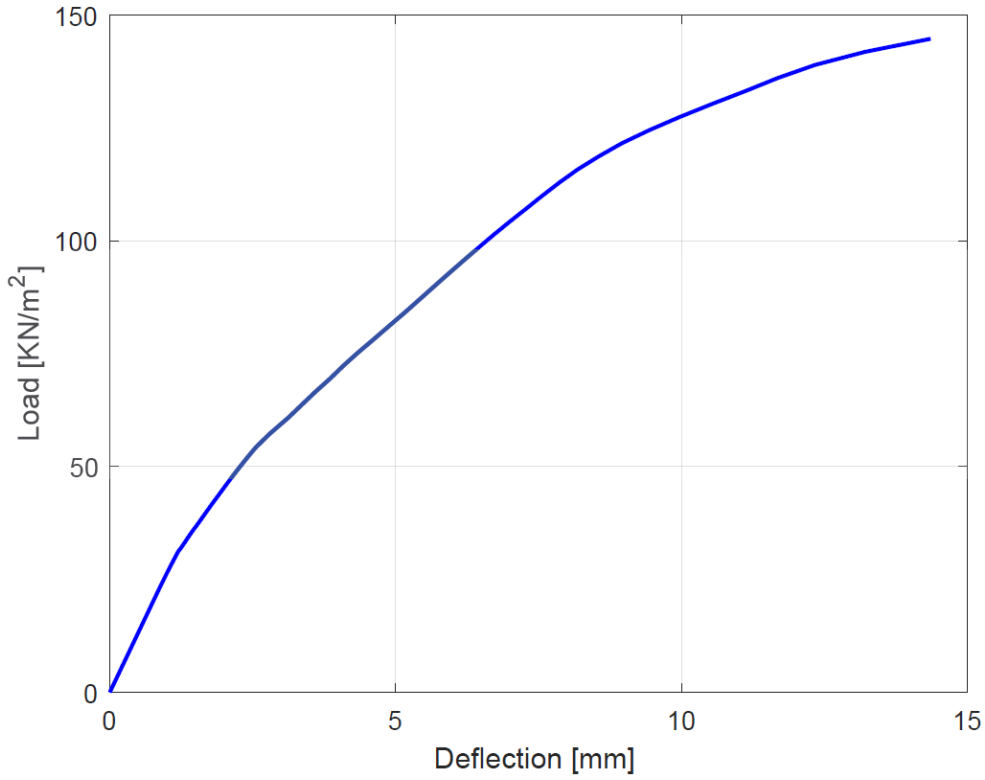

Figure 4.8: *Load-Deflection diagram for the studied pile supported slab under uniformly distributed load.*

Table 4.5: *Calculated capacity based on YLT versus capacity calculated from FEA for slab loaded under uniformly distributed load*

Calculated Capacity [kN/m^2]	FEA Capacity [kN/m^2]	Difference [%]
44.9	144.7	322

4.3.1.2 Crack stress and strain evaluation

Top surface

The response of the slab can be divided into two different main stages, before cracking and after cracking. Furthermore, the analysed panel is an interior type of panel, i.e. the modelled panel is part of a continuous slab. Therefore, before cracking, the moment over the pile cap is higher in comparison to the moment in the mid-span. Hence, it is expected to have more stresses over the pile cap, which results in cracks formation over the pile cap before the mid-span, as illustrated in Figure 4.9.

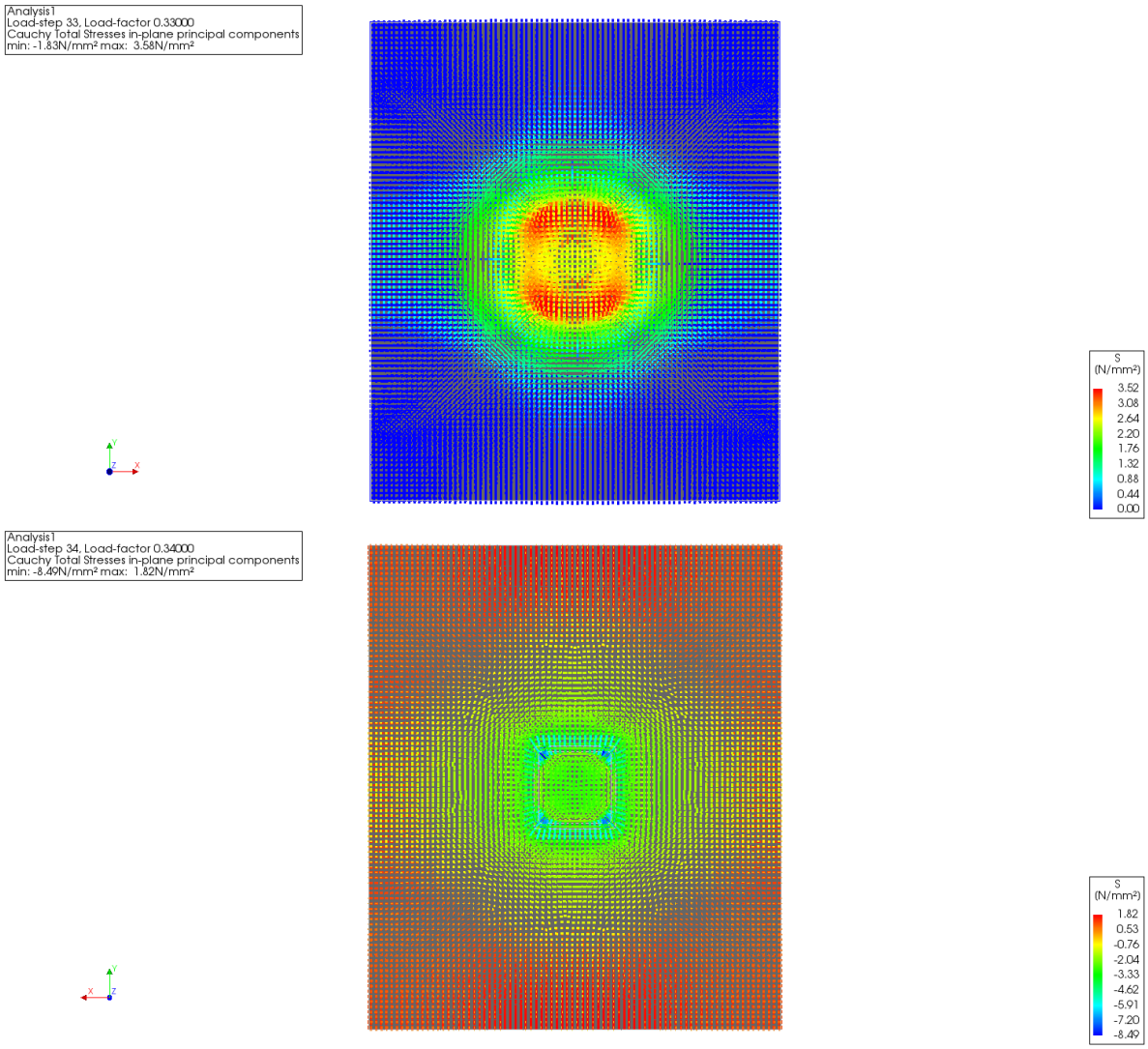

Figure 4.9: *Stress distribution of top (top) and bottom (bottom) surfaces (one stage before cracking in the top surface)*

After the formation of the first crack over the pile cap, this section, which is over the pile cap, starts to get reduced stiffness during cracking. This results in the so-called "plastic redistribution", i.e. since the post-cracking flexural response of the studied SFRC exhibits a hardening behaviour, it is expected to have moment hardening over the pile cap, which means the moment over the pile cap increases after the stage of cracking. On the other hand, the section of the mid-span starts dissipating more energy. When the load increases, the mid-span section starts to be cracked, which is accompanied by a decrease in the stiffness, meanwhile the section over the pile cap, which is already cracked starts to dissipate energy through the steel fibres (Figure 4.11). As the load increases, the calculated capacity according to yield line theory can be reached without showing failure in the slab, which springs from several factors, i.e. crack stresses decrease while crack strains increase, respectively (Figure 4.12). One of the most important factors, which is involved is the arching action phenomenon. Another factor that can be mentioned is that the hand calculation is based on a conservative tensile constitutive model. In case of SFRC, the crack model has been chosen based on the fictitious crack model, which results in a reduction in the stress while the strain increases. As illustrated in Figure 4.13 to Figure 4.15, this procedure continues and makes the cracks more localized until the failure occurs.

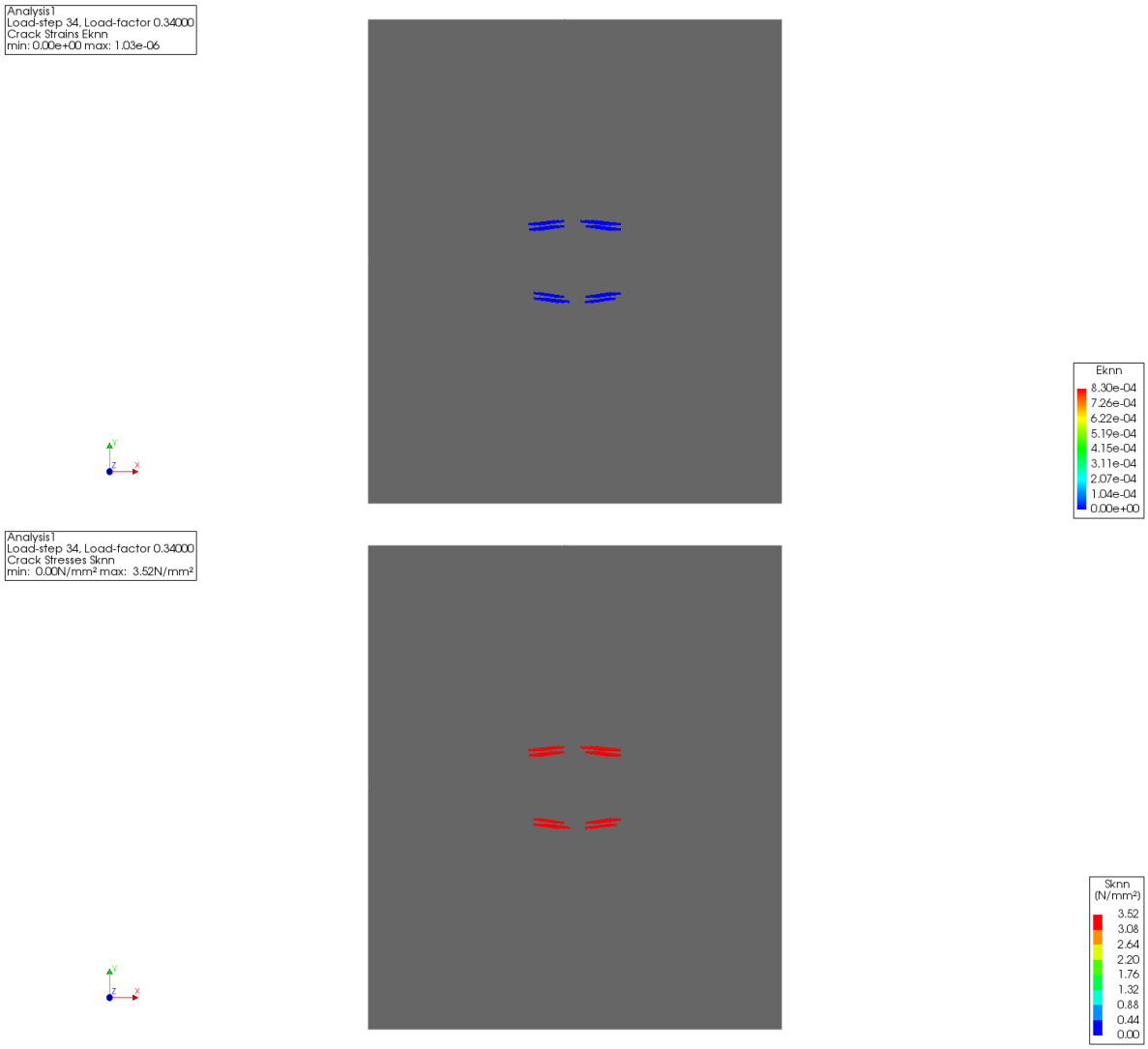

Figure 4.10: *Crack stress and strain of top surface at load 19.7 kN/m^2 (first crack at top surface).*

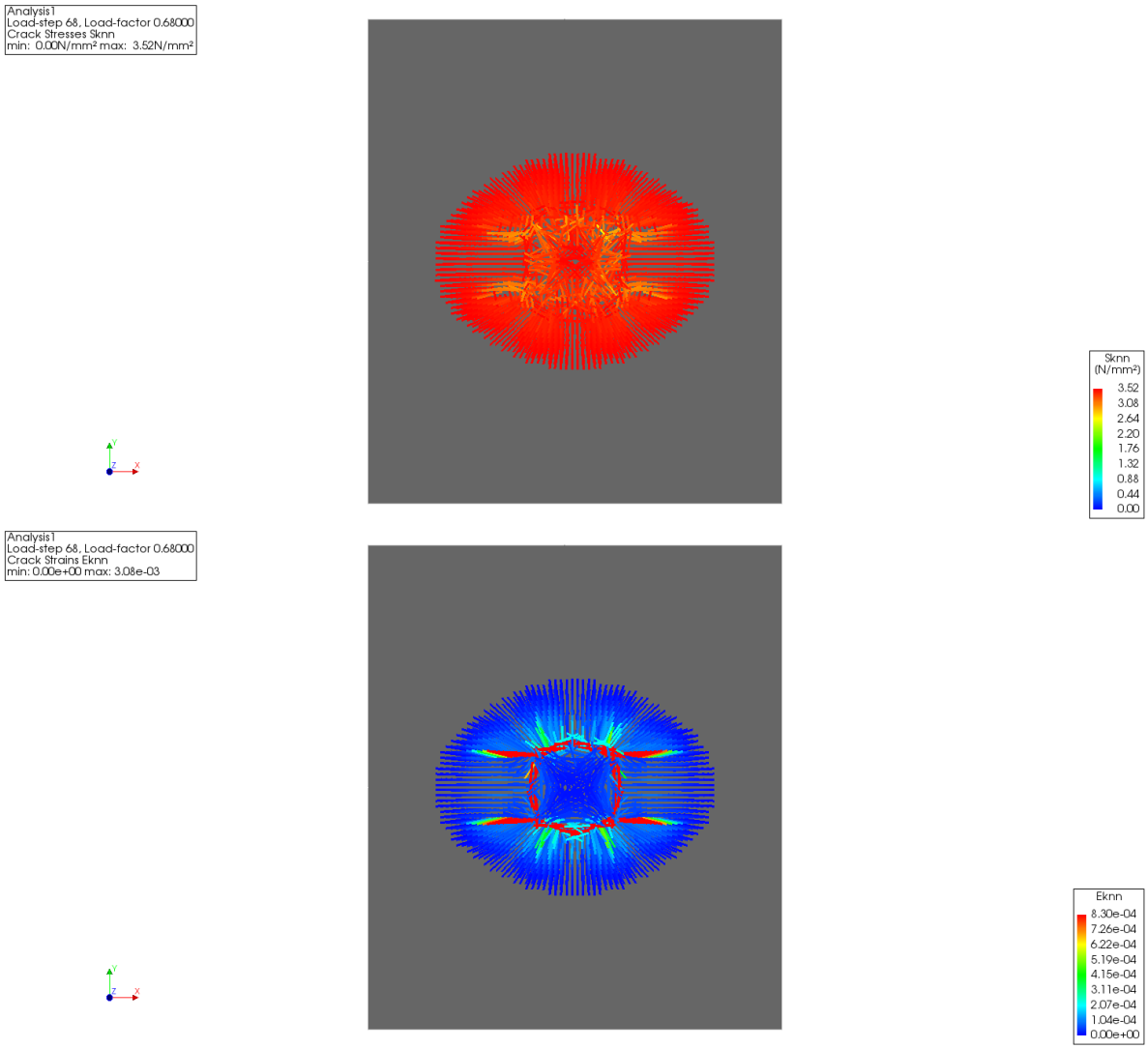

Figure 4.11: *Crack stress and strain of top surface at load 39.4 kN/m^2 (first crack at bottom surface)*

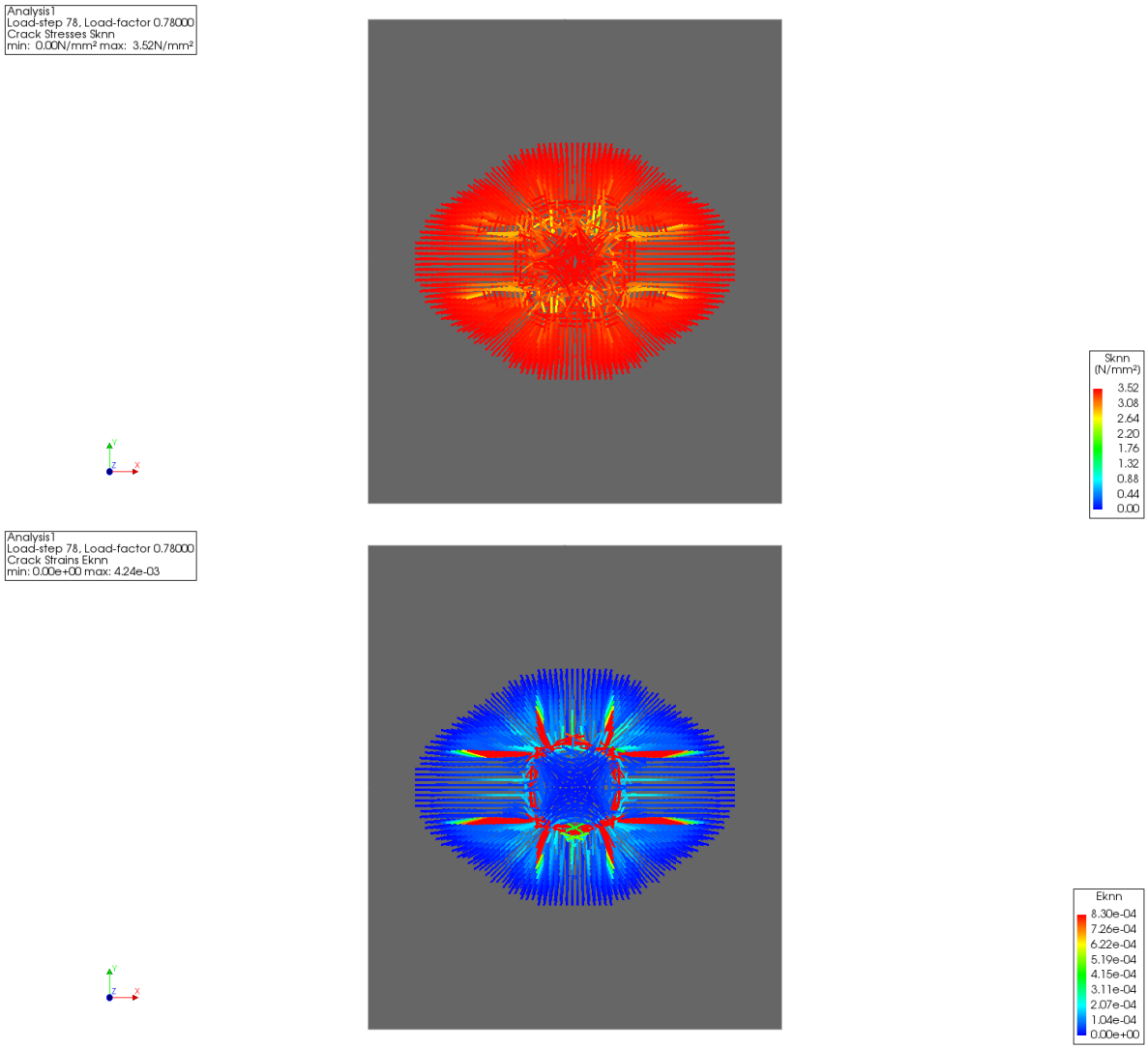

Figure 4.12: *Crack stress and strain of top surface at load 45.1 kN/m^2 (almost equivalent to the calculated capacity)*

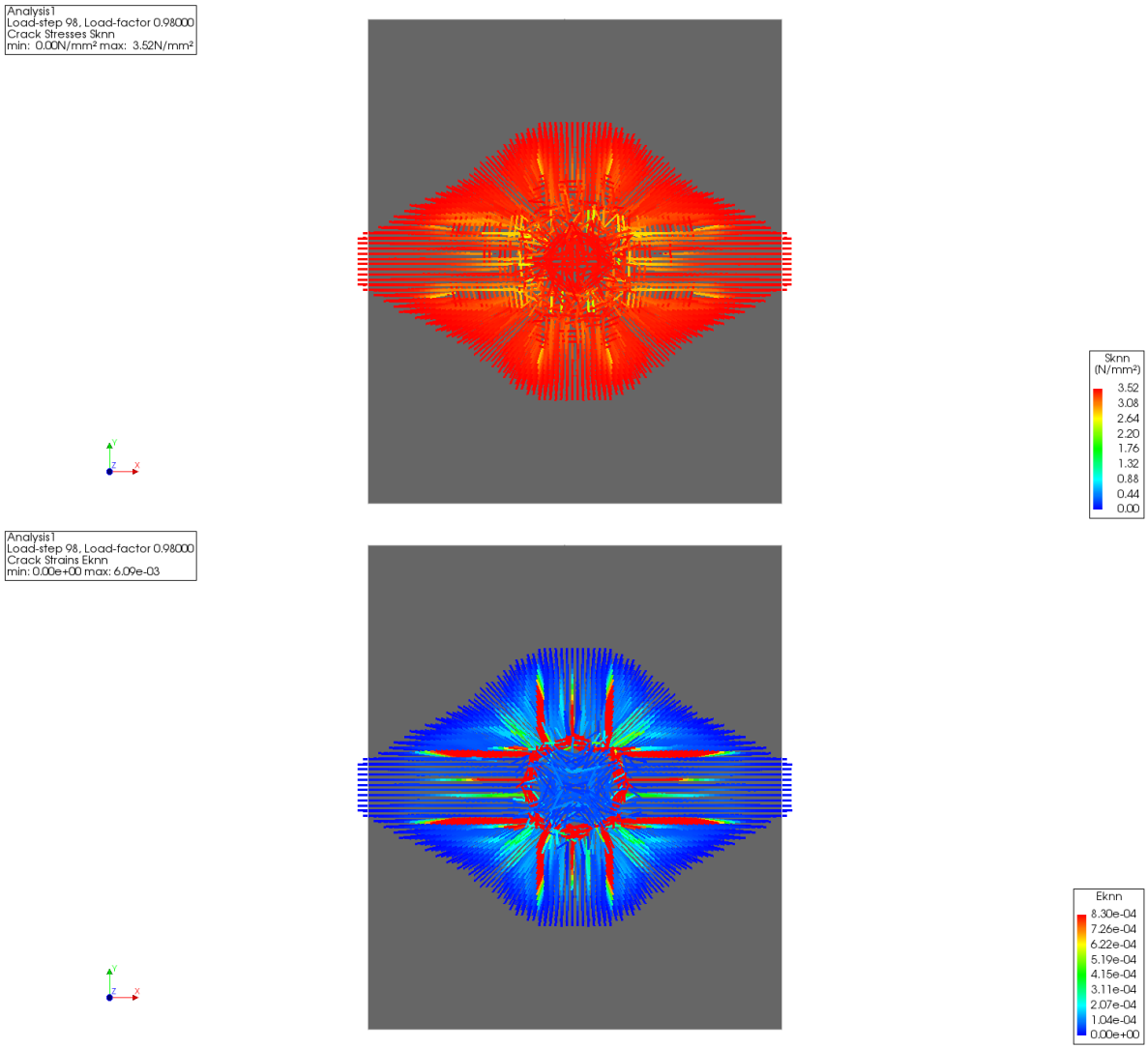

Figure 4.13: *Crack stress and strain of top surface at load 56.7* kN/m^2

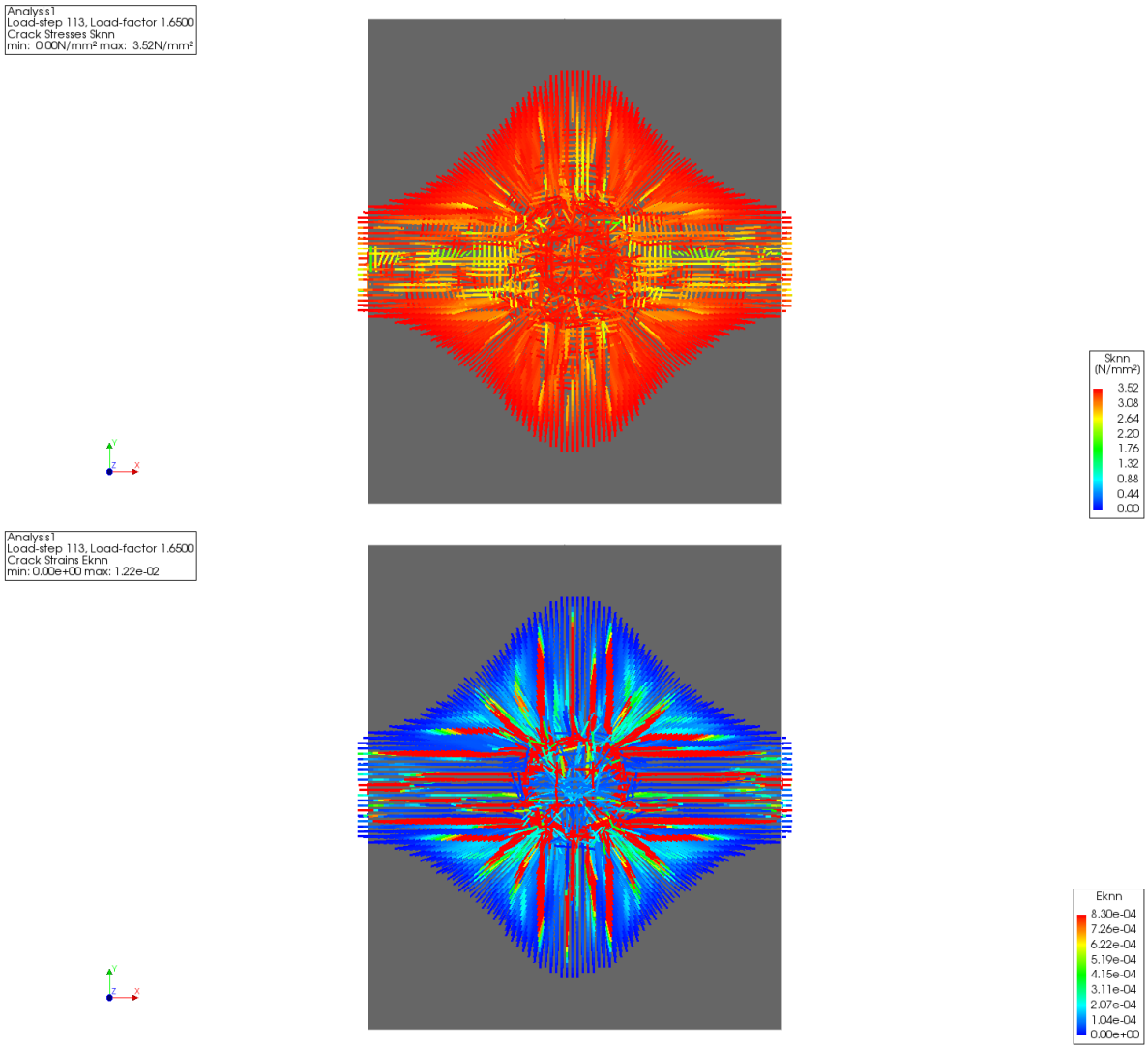

Figure 4.14: *Crack stress and strain of top surface at load 95.5* kN/m^2

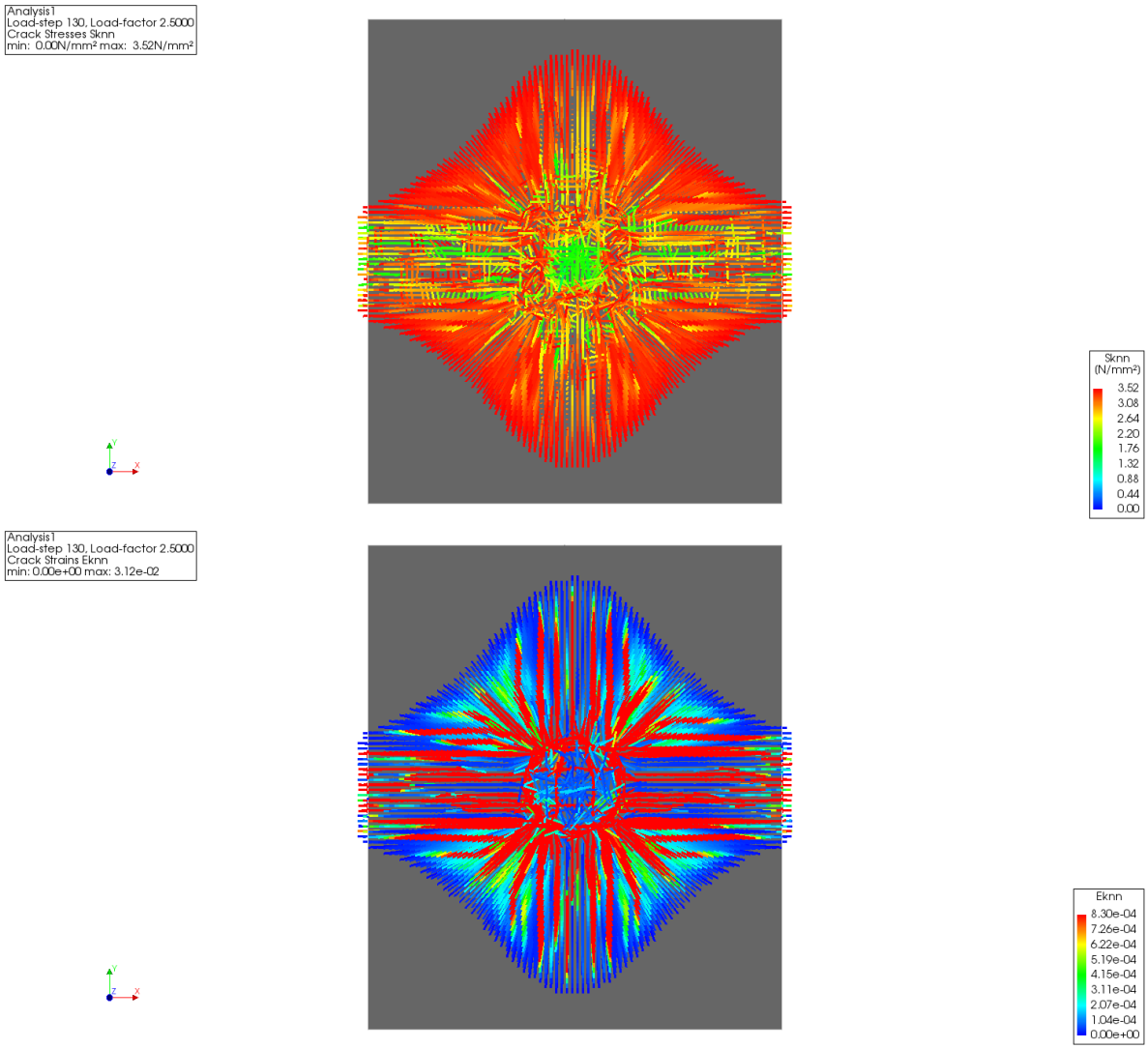

Figure 4.15: *Crack stress and strain of top surface at load 144.7 kN/m^2 (failure load)*

Bottom surface

Regarding the bottom surface, it could be observed that it will stay in the elastic state when the first crack initiates over the pile cap due to the fact that the bending moment is highest there. As the load increases, the crack over the pile cap grows, and a plastic redistribution will occur until the cracking moment is reached in the mid-span. All stated above, will result in a stress distribution before cracks initiate in the mid-span, which is smooth in the bottom surface, whereas it is disturbed in the cracked area over the pile cap (Figure 4.16).

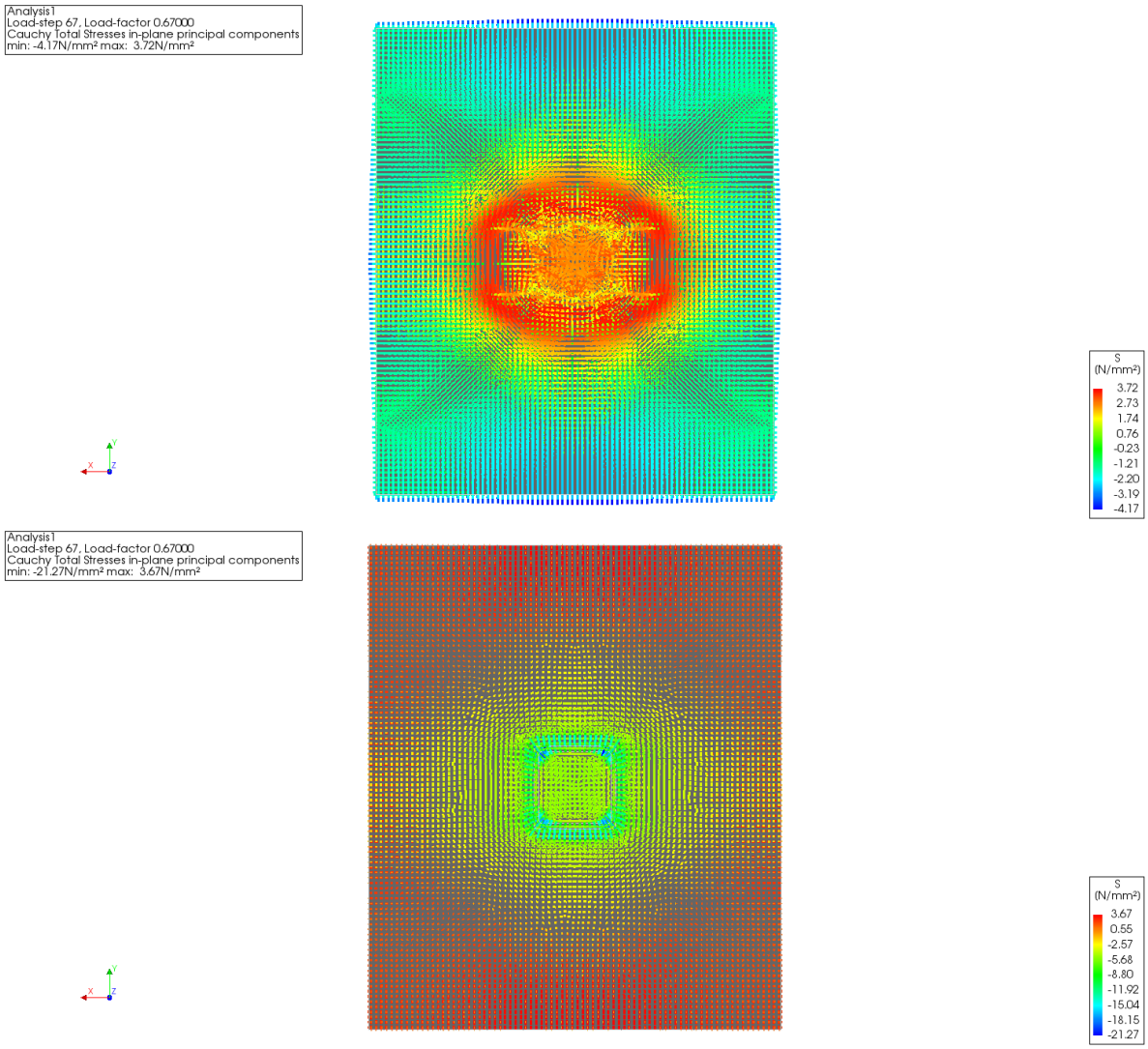

Figure 4.16: *Stress distribution of top (top) and bottom (bottom) surfaces (one stage before cracking in the bottom surface)*

By comparing Figure 4.10 and Figure 4.17, it can be seen that the load at crack initiation is equivalent to 19.7 kN/m^2 for the top surface while it is 39.4 kN/m^2 for the bottom surface, which means that the first crack initiates in the bottom surface when the load is twice the load for crack initiation in the top surface. The mid-span cracks in the bottom surface initiate in the long span direction before the short span, which can be supported by the fact that moments are slightly higher in the long span direction (Figure 4.17). Furthermore, Figure 4.18 shows that the calculated load based on yield line theory is not high enough to cause failure in the studied slab. It can also be noticed that the stress, when the load is equivalent to the calculated capacity based on YLT, both stress and strain are in the marked region in Figure 4.22, where there is no significant contribution from steel fibres, i.e. the contribution from steel fibres is small, and the major part of the stress is carried by concrete, not fibres. Afterwards, as illustrated in Figure 4.19, Figure 4.20 as well as Figure 4.21, when the load increases, the cracked region spreads more through the bottom surface of the slab until the failure occurs. It is beneficial to mention that the stress is decreased in the cracked zones since it is following the tensile constitutive model, while the strain is increasing (Figure 3.24). Figure 4.21 illustrates that cracks at the pile cap are also formed in the bottom surface. However, this occurs when the load exceeds 115.8 KN/m^2 and the crack strains at the corners of the pile cap have such a high value, which means that some element suffering from punching shear failure. This issue arises from the fact that

the elements in the mentioned areas are triangular elements (knife elements), which could result in forming a shear punching type of failure in some elements.

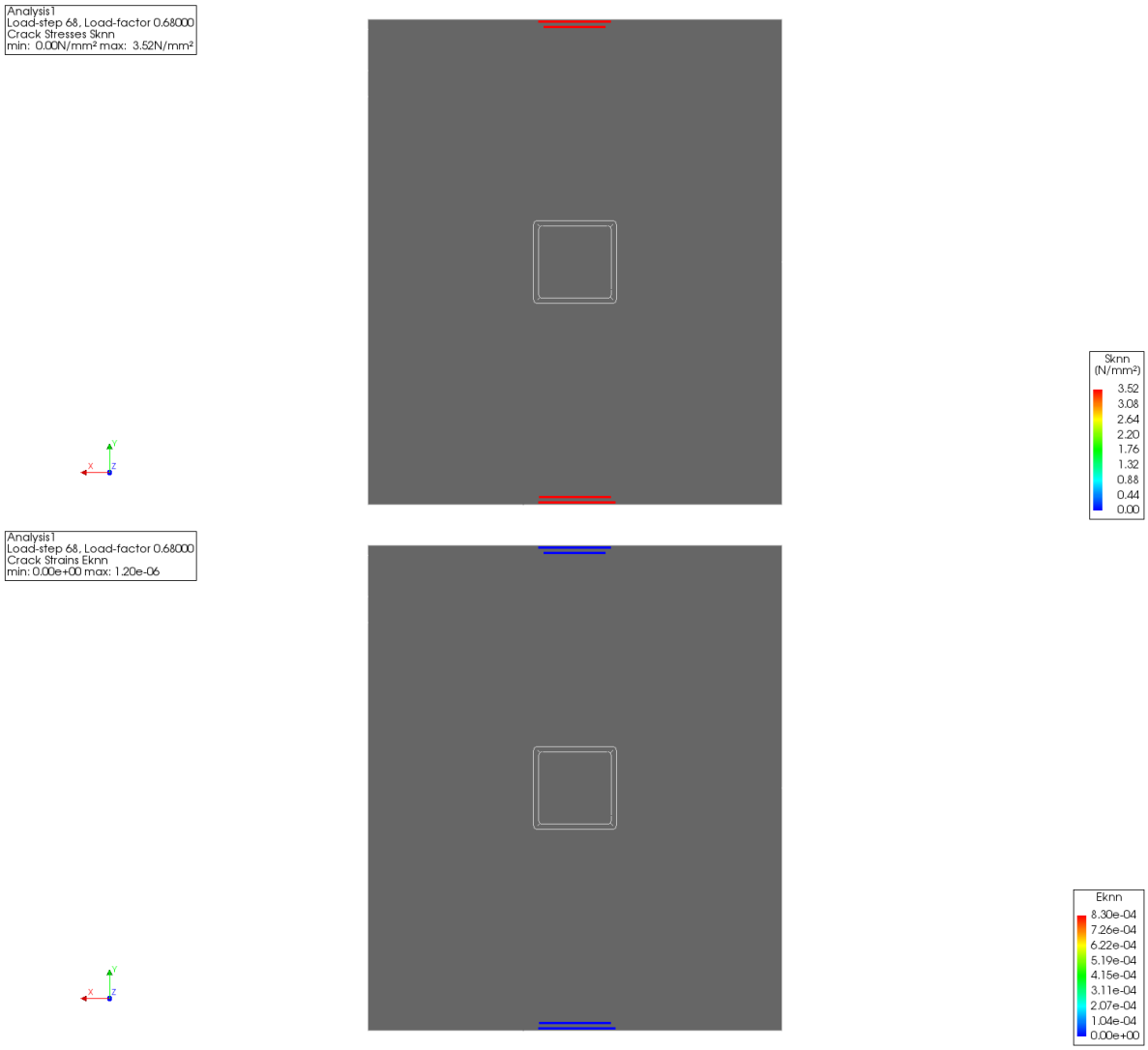

Figure 4.17: *Crack stress and strain of bottom surface at load 39.4 kN/m^2 (first crack at bottom surface)*

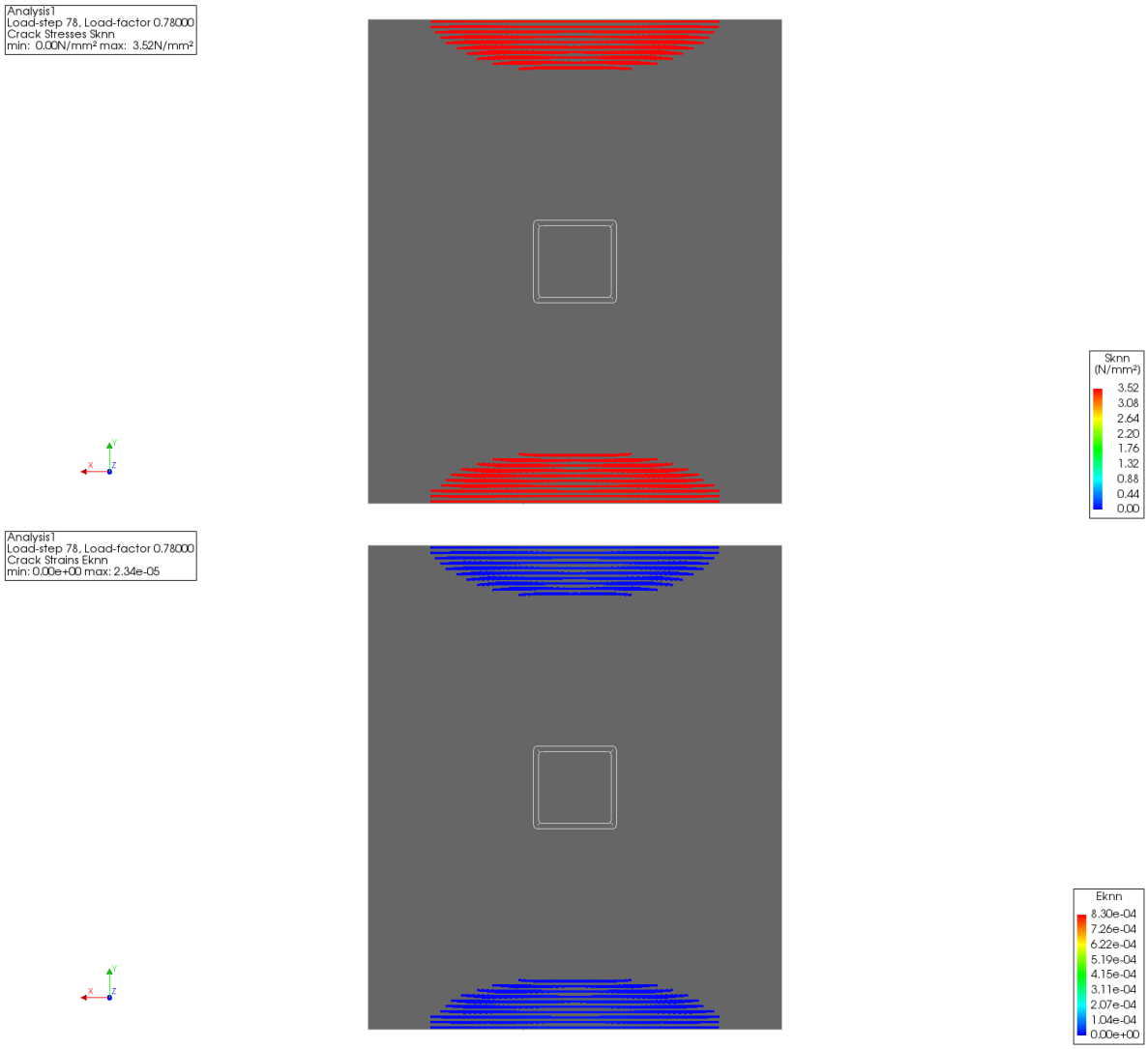

Figure 4.18: *Crack stress and strain of bottom surface at load 45.1 kN/m^2 (almost equivalent to the calculated capacity)*

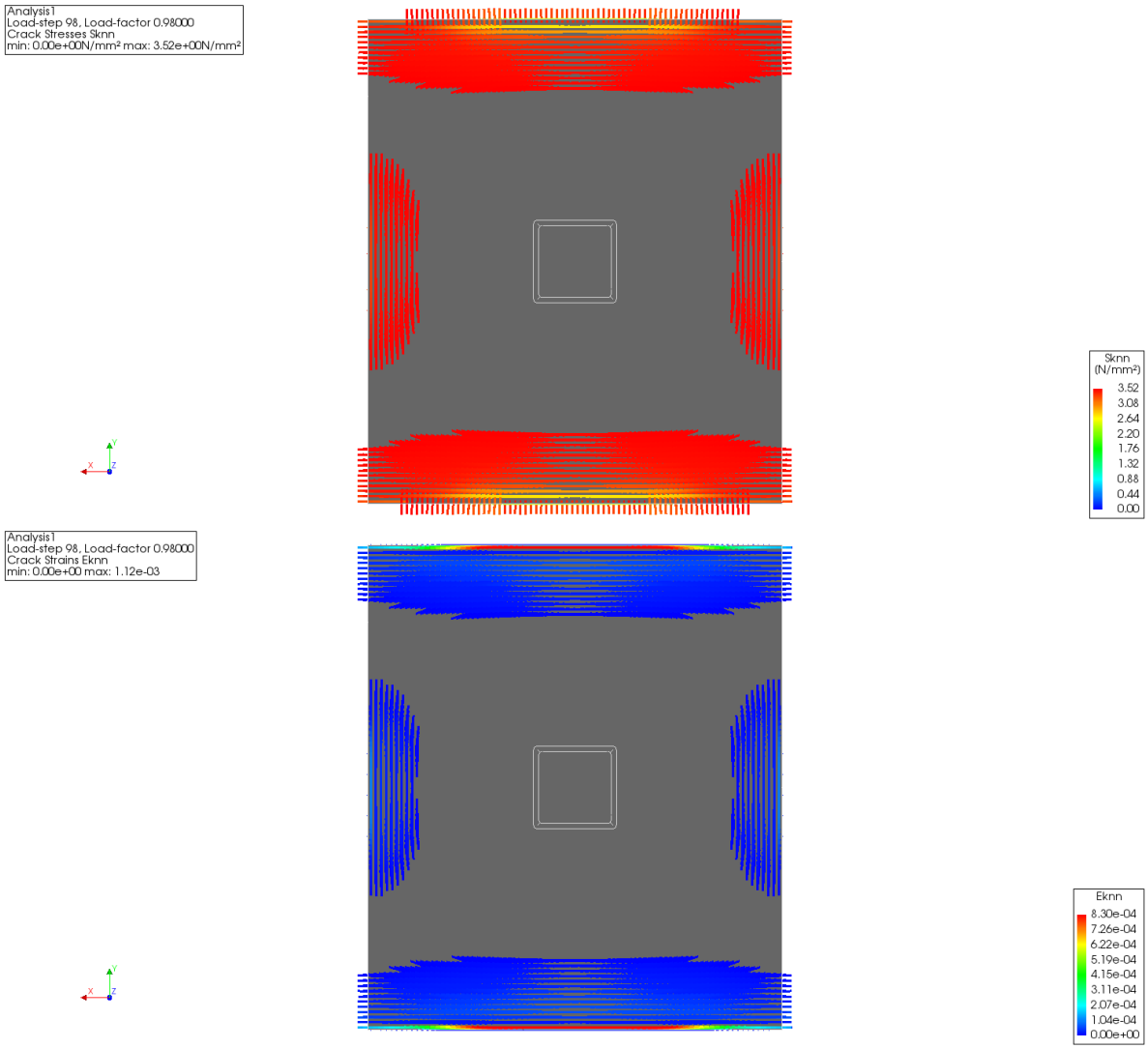

Figure 4.19: *Crack stress and strain of bottom surface at load 56.7* kN/m^2

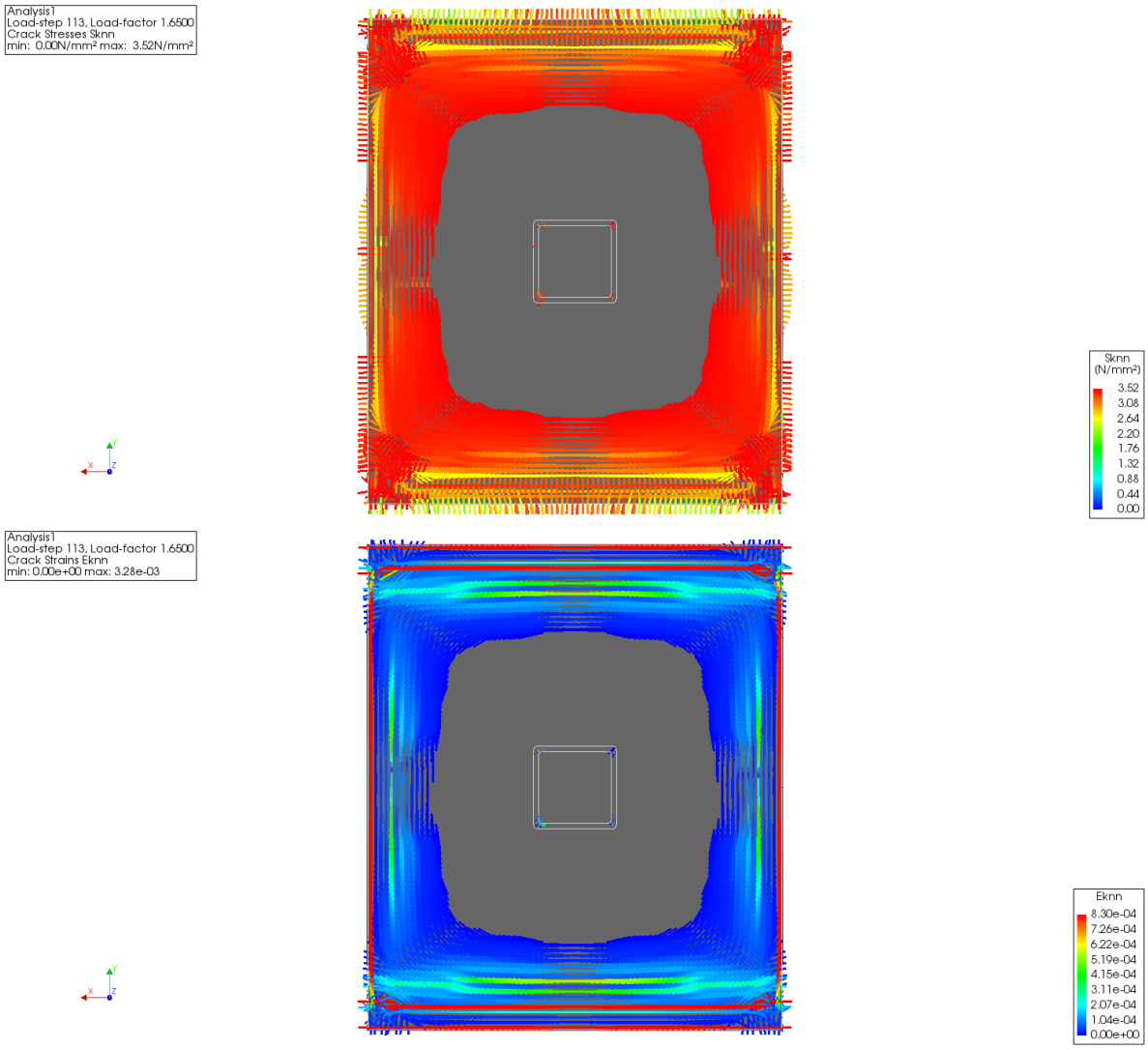

Figure 4.20: *Crack stress and strain of bottom surface at load 95.5* kN/m^2

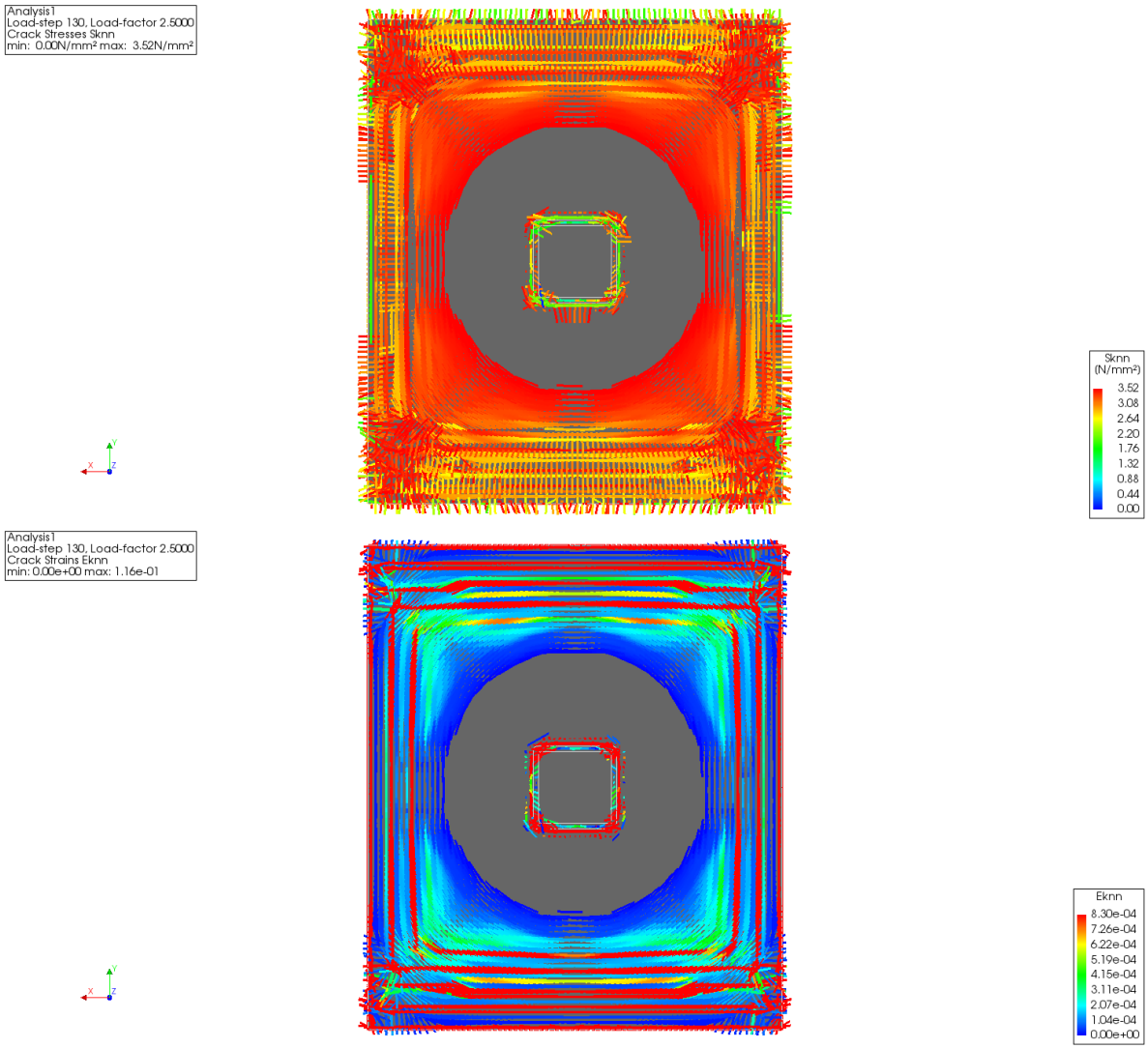

Figure 4.21: *Crack stress and strain of bottom surface at load 144.7 kN/m^2 (failure load)*

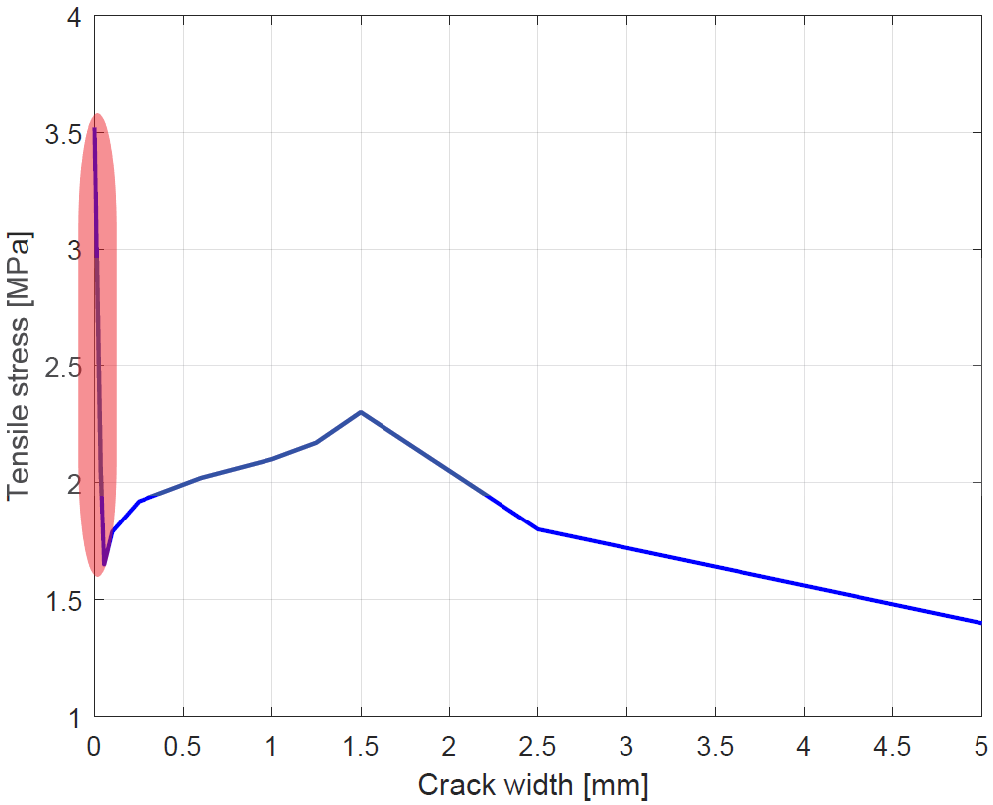

Figure 4.22: *Stress-crack width region immediately after cracking*

4.3.1.3 Crack evaluation

The crack pattern for both the bottom and top surface of the studied slab is present in Figure 4.23, and the crack development can be seen in appendix A.2. Regarding the top surface, the first plastic hinge develops over the pile cap, which results in a fully cracked section around the pile cap at failure. On the other hand, for the bottom surface, the second plastic hinge is expected to form in the mid-span as the maximum positive moment is there. The formation of both mentioned plastic hinges leads to failure. Furthermore, by investigating the crack width in the studied slab after a certain deflection equal to 8.5 mm, it has been found that the crack width in the bottom surface around the pile cap (in several elements close to corners of drop panel) has significantly increased in comparison to the crack width in the top surface around the pile cap. Hence, it is believed that a shear punching type of failure has started in several elements that are close to corners of the drop panel for the load corresponding to a deflection of about 8.5 mm. The presence of a few knife elements (sharp elements) in the sharp corners of the drop panel may have caused stress concentration, which may contribute to the formation of shear punching failure.

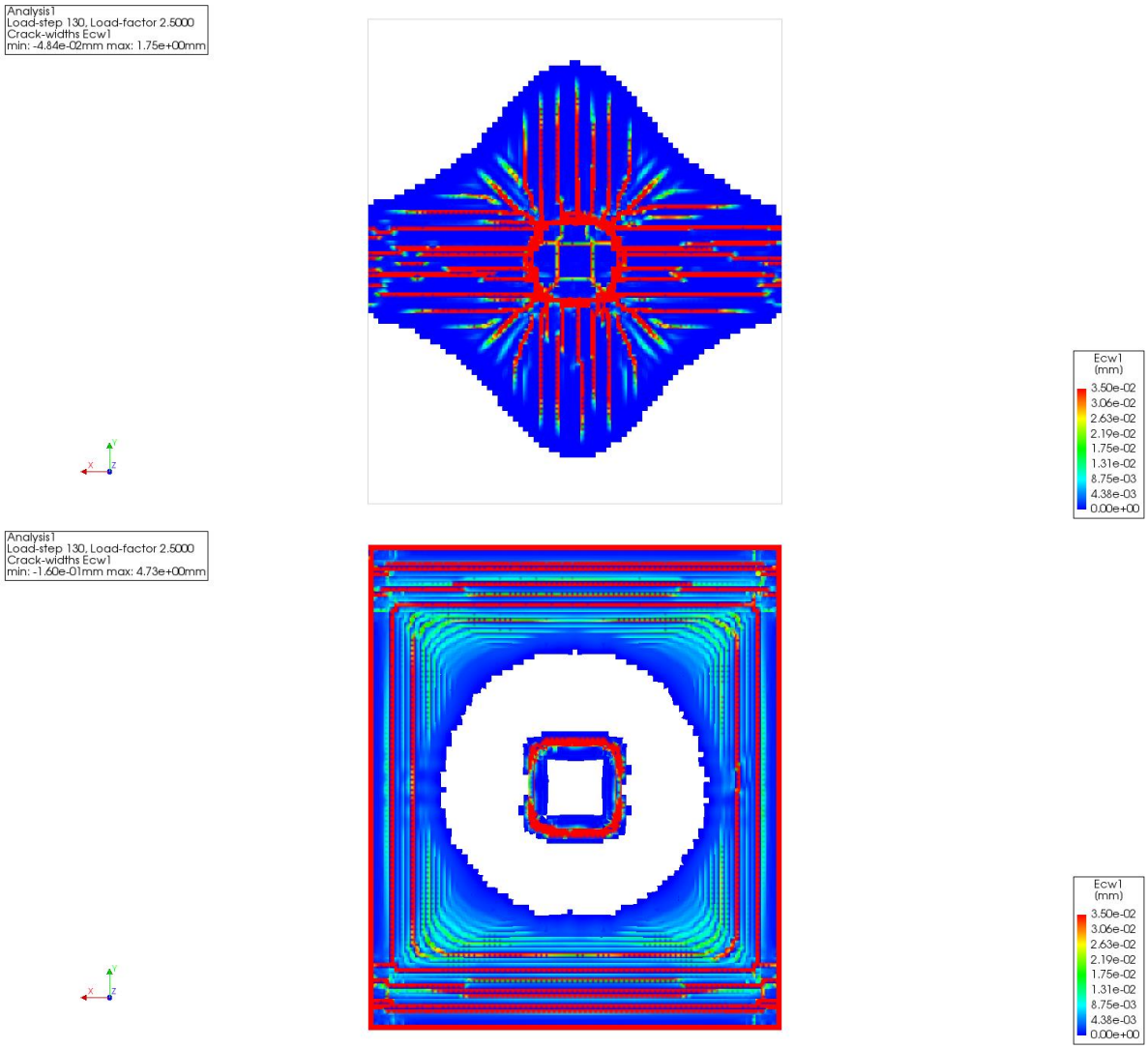

Figure 4.23: *Crack pattern for top surface (top) and bottom surface (bottom) of the slab under uniformly distributed load*

From Figure 4.24, it can be understood that the negative yield lines are fully formed in the short direction, passing through the pile caps. Furthermore, the cracks are denser in the mid-span of short direction, which is an indication for the fact that yield lines are formed in the mid-span.

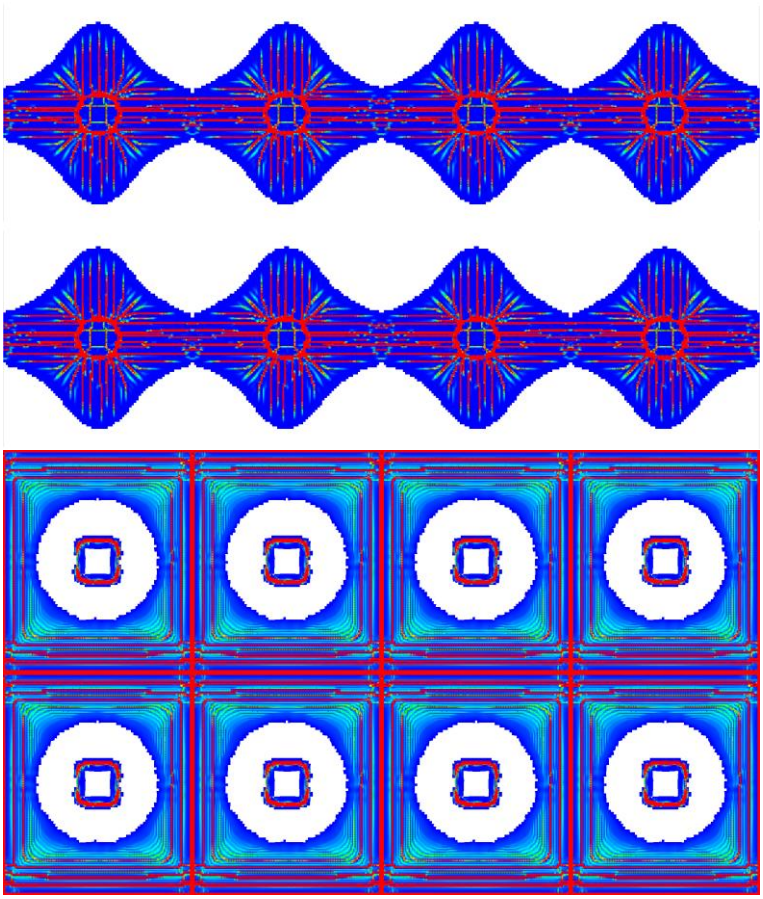

Figure 4.24: *Positive (top) and negative (bottom) yield lines for the entire slab*

Since the section over the pile cap will be cracked before the mid-span section, it is expected to have larger crack widths over the pile cap than the mid-span section (Figure 4.10 and Figure 4.17).

Table 4.6: *Deflection and crack width in several stages for slab under uniformly distributed load*

Stage	Deflection [mm]	Crack width over the pile cap (top surface) [mm]	Crack width at mid-span (bottom surface) [mm]
At stage of first crack in the top surface	0.74	0.0000507 (Negligible)	-
At stage of first crack in the bottom surface	1.66	0.18	0.0000551 (Negligible)
At stage of hand-calculated capacity	1.99	0.25	0.00106
At stage of failure	14.36	1.75	0.36

4.3.2 Pile-supported slab under point load

4.3.2.1 Structural behaviour evaluation

The finite element analysis of the studied slab under point load displays a capacity of 1152.6 kN, which is 1.72 times the hand-calculated capacity (see appendix B.3) (Table 4.7). This difference is expected, and several research papers have investigated the difference between experimental capacity versus calculated capacity and found that the experimental capacity is significantly higher than the calculated capacity based on bending theory (Venkateshwaran & Tan, 2018). This discrepancy springs from several factors such as arching action, the effect of drop panel and the support conditions as well as the implementation of a conservative constitutive tensile model in the hand calculation. These sources of discrepancy are discussed more in detail in 2.7.5 and 4.3.1.1. It must be emphasised that the major increase arises from the arching action effect. Figure 4.25 displays the load-deflection diagram for the studied slab under point load, which shows some changes in the slope due to cracking.

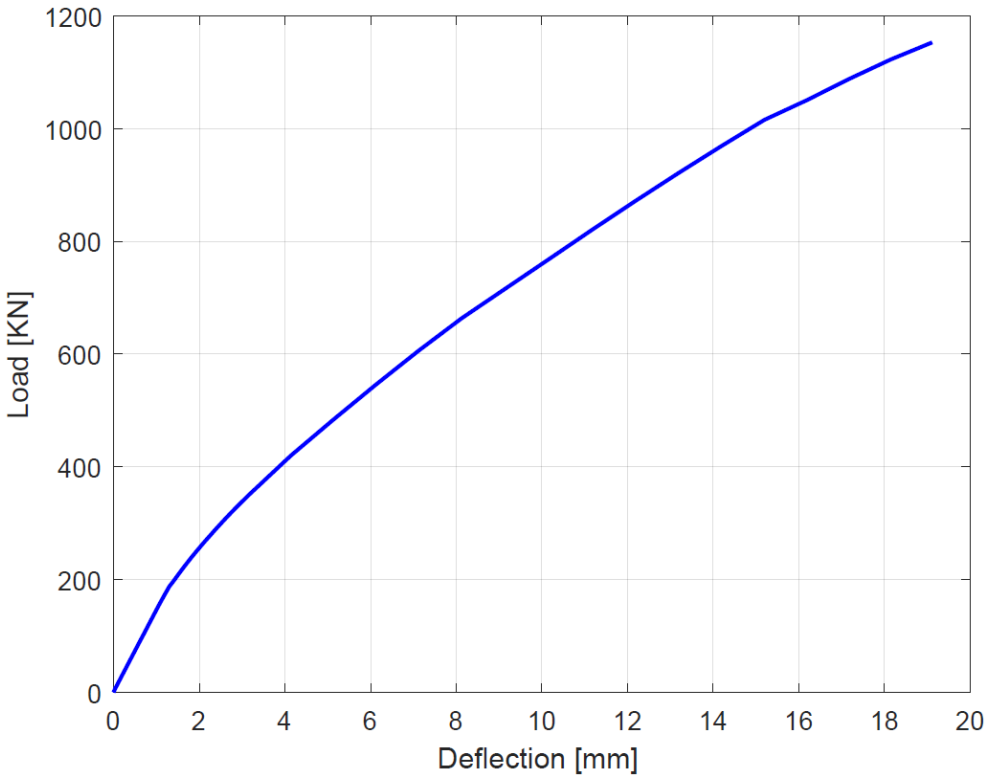

Figure 4.25: *Load-Deflection diagram for the studied pile supported slab under point load*

Table 4.7: *Calculated capacity based on YLT vs. capacity calculated from FEA for slab loaded under point load*

Calculated Capacity [kN]	FEA Capacity[kN]	Difference [%]
668.7	1152.6	172

4.3.2.2 Crack stress and strain evaluation

Bottom surface

Due to the point load acting in the centre of the slab, it is expected to see the first crack initiation in the bottom surface, under the point load (Figure 4.26). In this stage, there are no other cracks in the slab. When the load increases, the top surface starts being cracked, meanwhile the existing cracks in the bottom surface will propagate more. The mentioned behaviour results in a reduction of stress as well as an increase of strain in several cracks, which are propagating (Figure 4.27). It should be noted that since the slab is under point load, the cracks will propagate in a circular way, as illustrated in Figure 4.27. Furthermore, when the load reaches the calculated capacity based on YLT (Figure 4.28), the yield lines are still in a stage of forming, i.e. the actual maximum capacity is not reached, and the slab has not failed yet. Moreover, at the failure stage (Figure 4.29), there is a significant reduction in crack stresses as well as a remarkable increase in the crack strain. The mentioned changes in crack stress and strain, which are following the tensile constitutive model of SFRC, results in the fact that negative yield lines are fully formed, and the failure mechanism has occurred, i.e. the hinges along the yield lines are formed.

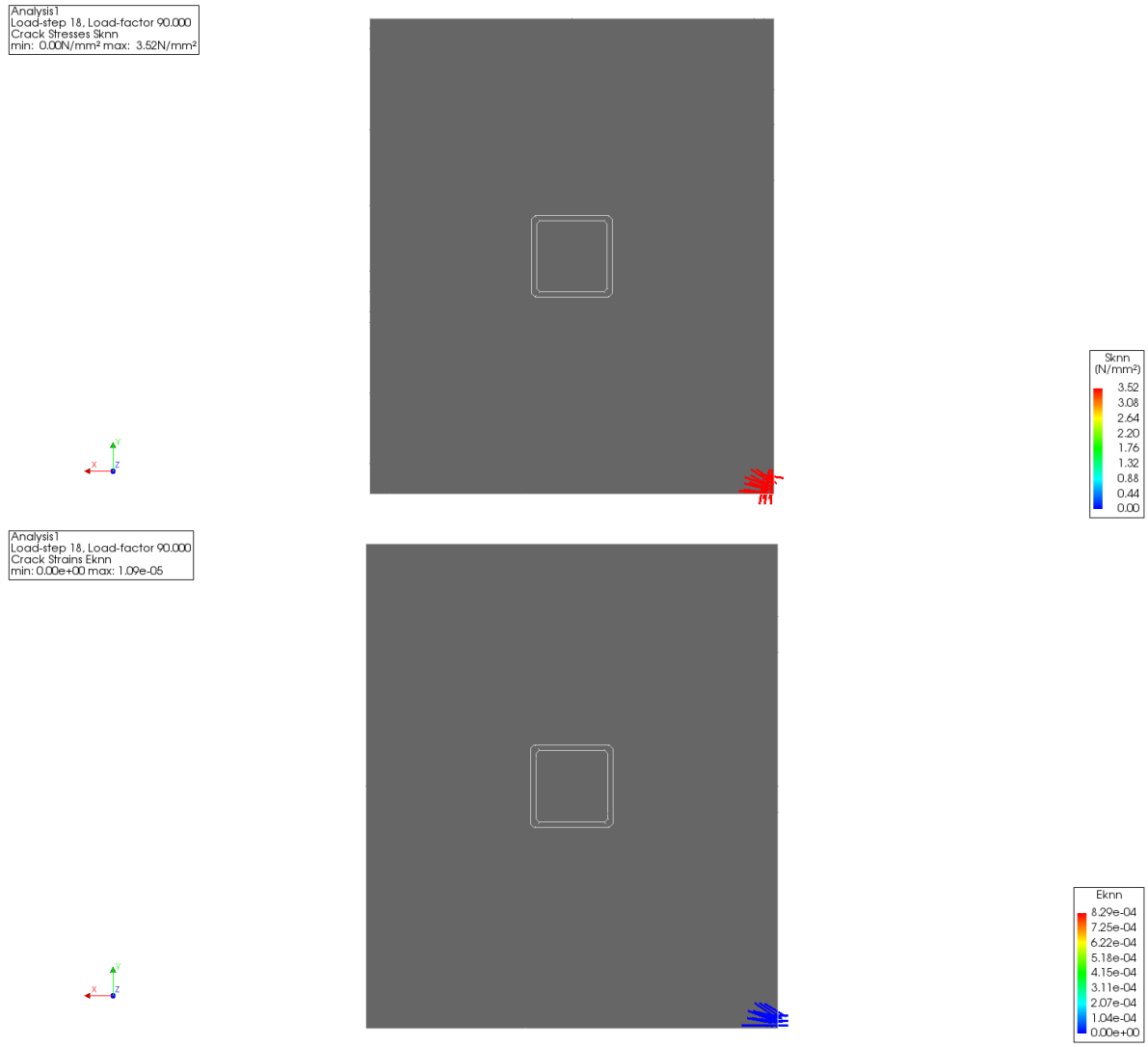

Figure 4.26: *Crack stress and strain of bottom surface at load 132.1 kN (First crack at bottom surface)*

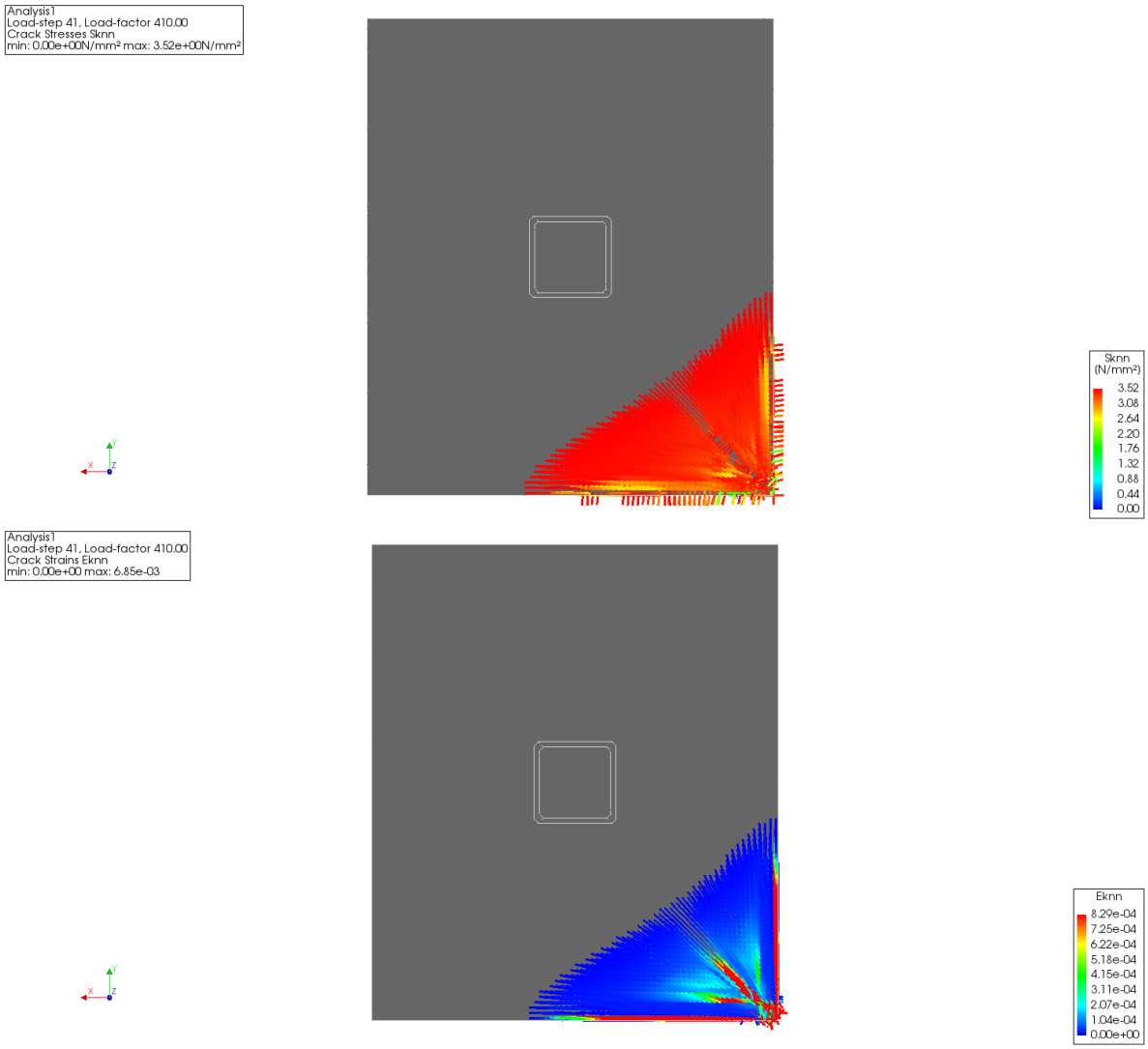

Figure 4.27: *Crack stress and strain of bottom surface at load 419.8 kN (First crack at top surface)*

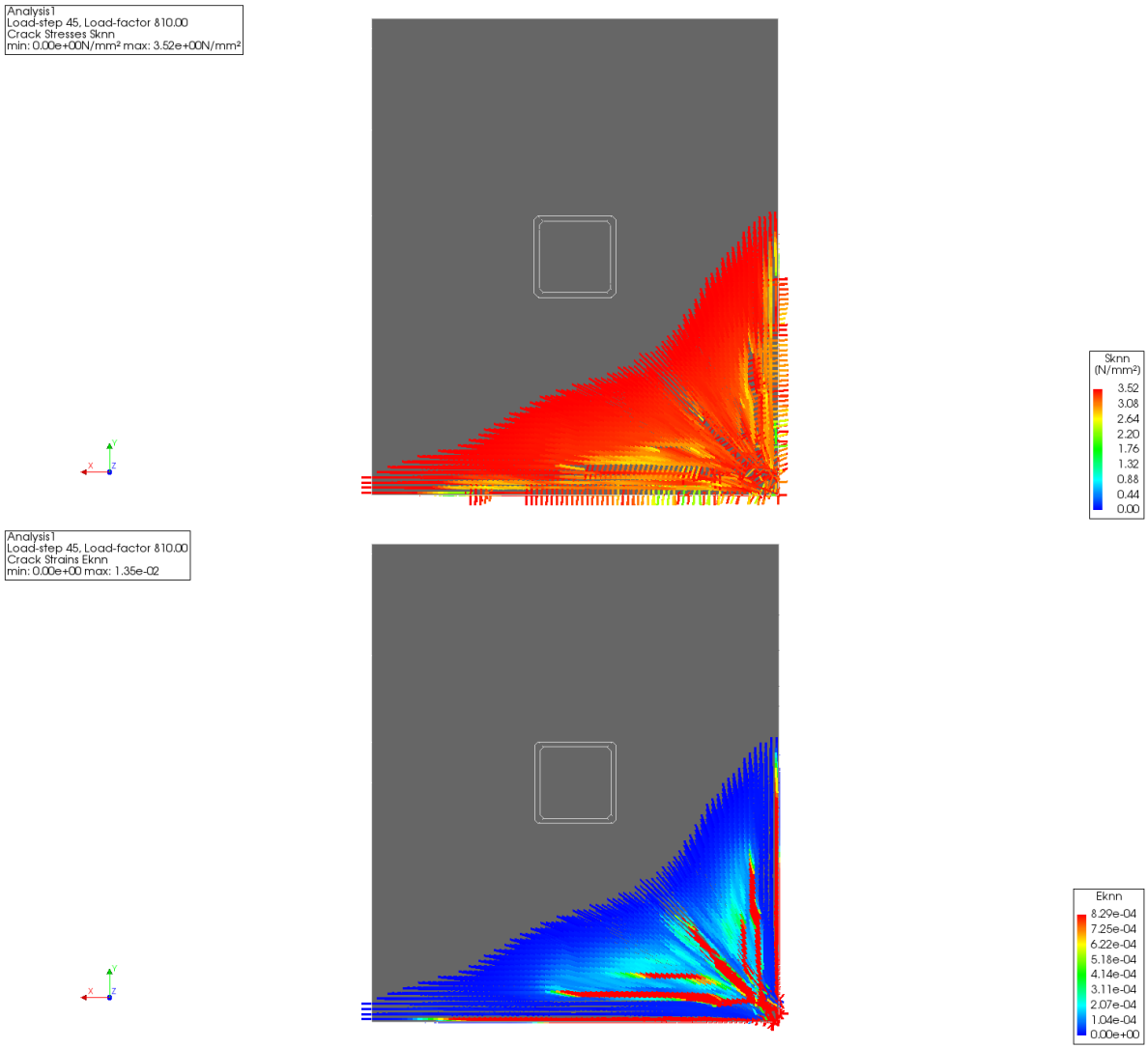

Figure 4.28: *Crack stress and strain of bottom surface at load 663.8 kN (almost equivalent to the calculated capacity)*

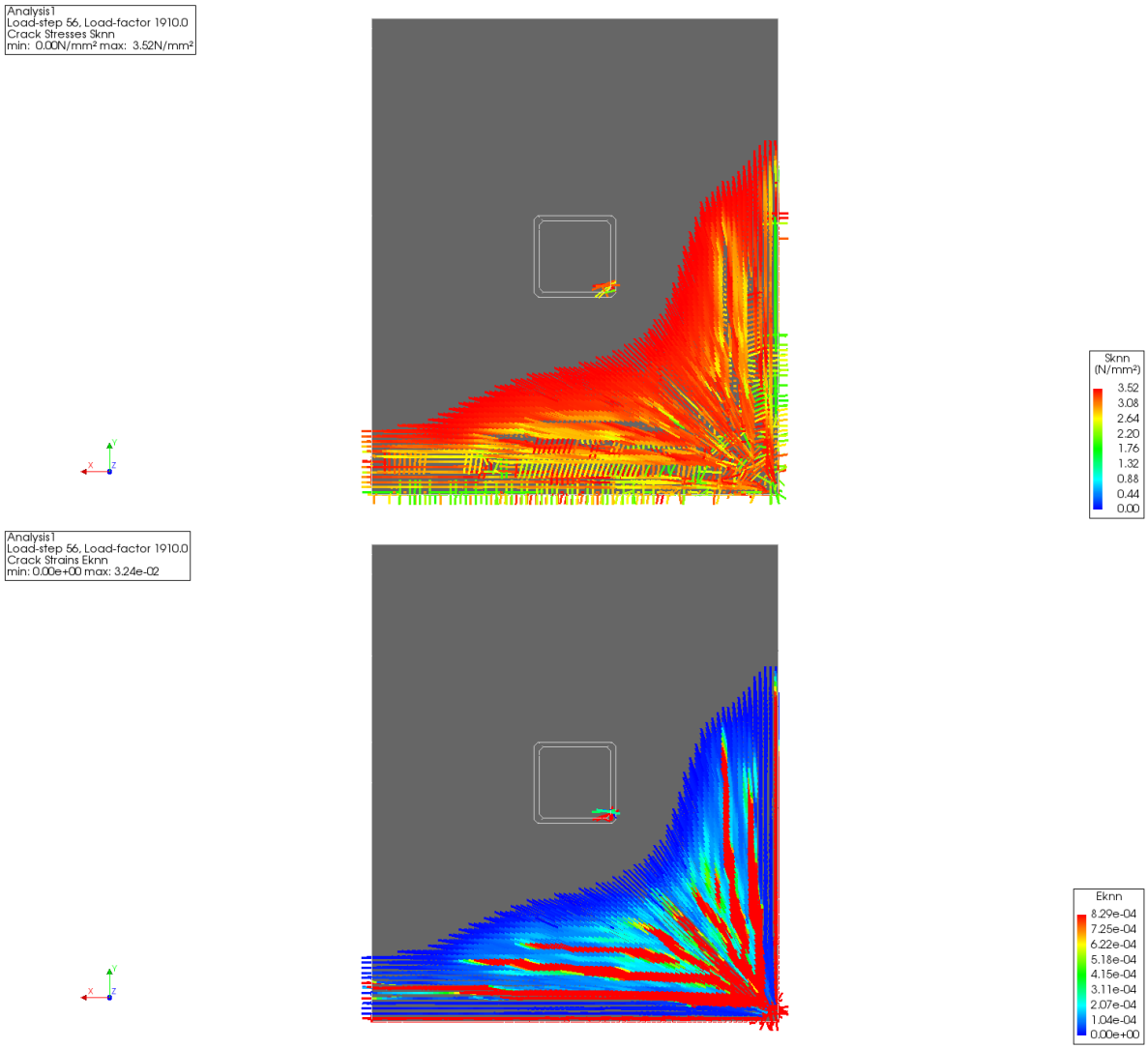

Figure 4.29: *Crack stress and strain of bottom surface at load 1152.6 kN (Failure load)*

Top surface

Regarding the top surface of the slab, the first crack initiates over the pile cap when the load is equivalent to 419.8 kN (Figure 4.30). However, this crack is small in the following stage. Moreover, the calculated capacity based on YLT is showing an underestimation since the positive yield lines are not fully formed (Figure 4.31), i.e. the slab is still capable of carrying more load. At the end, when the load increases to 1152.6 kN, the crack stresses drop significantly, whereas the crack strains increase. This remarkable change in crack stress and strain (Figure 4.32) occurs in a way to form a circular crack pattern, which is representative of positive yield lines.

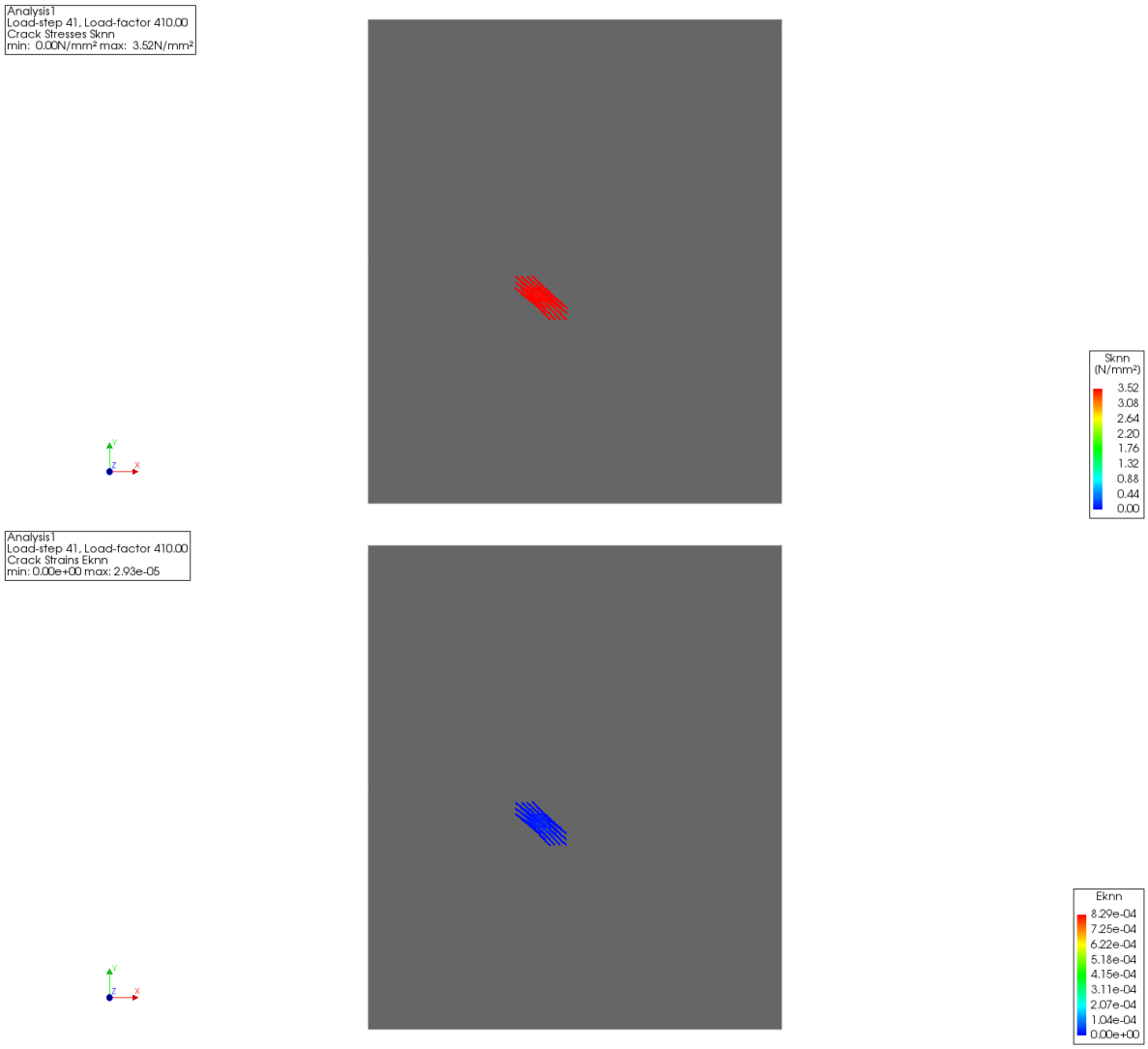

Figure 4.30: *Crack stress and strain of top surface at load 419.8 kN (First crack at top surface)*

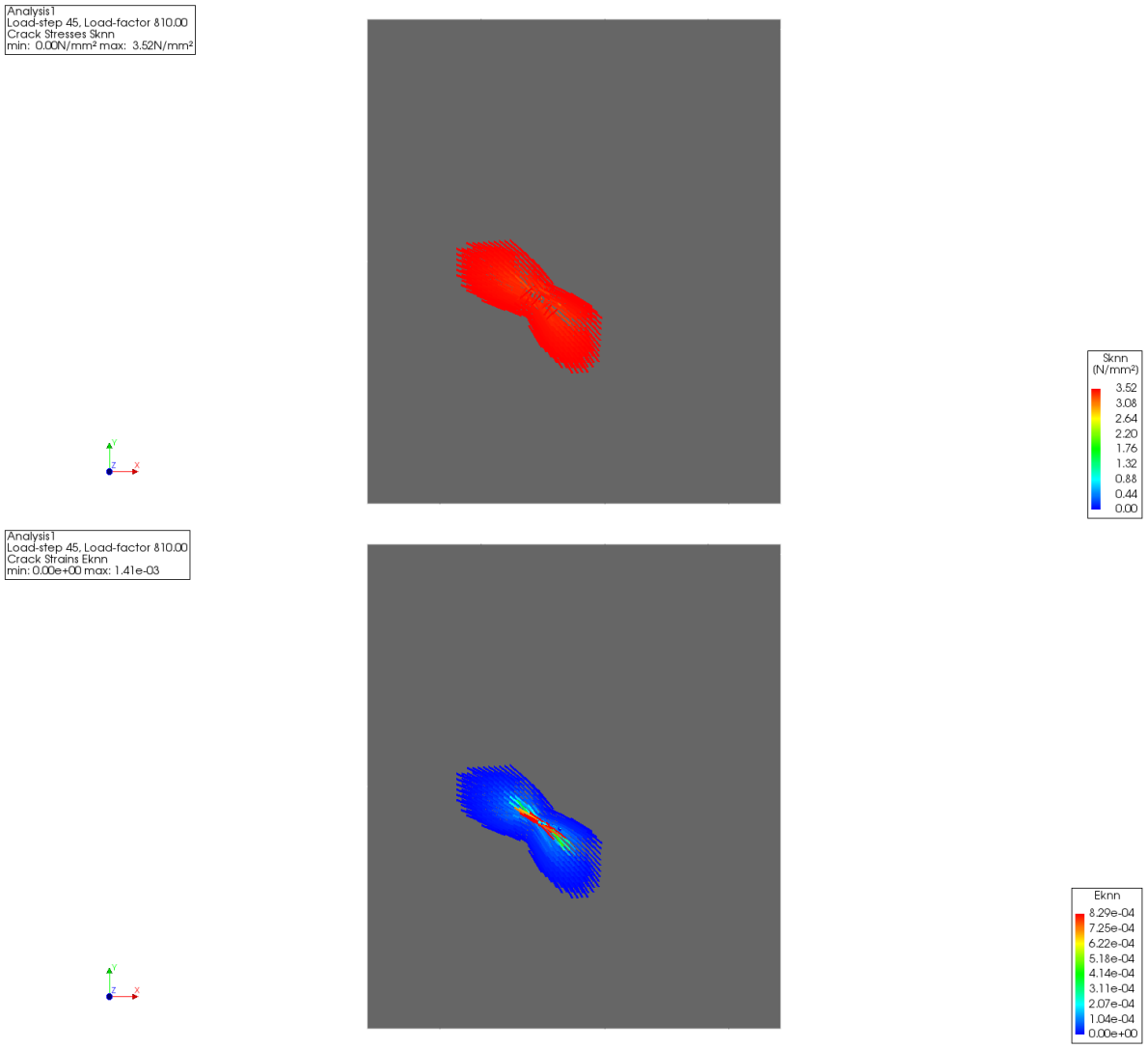

Figure 4.31: *Crack stress and strain of top surface at load 663.8 kN (almost equivalent to the calculated capacity)*

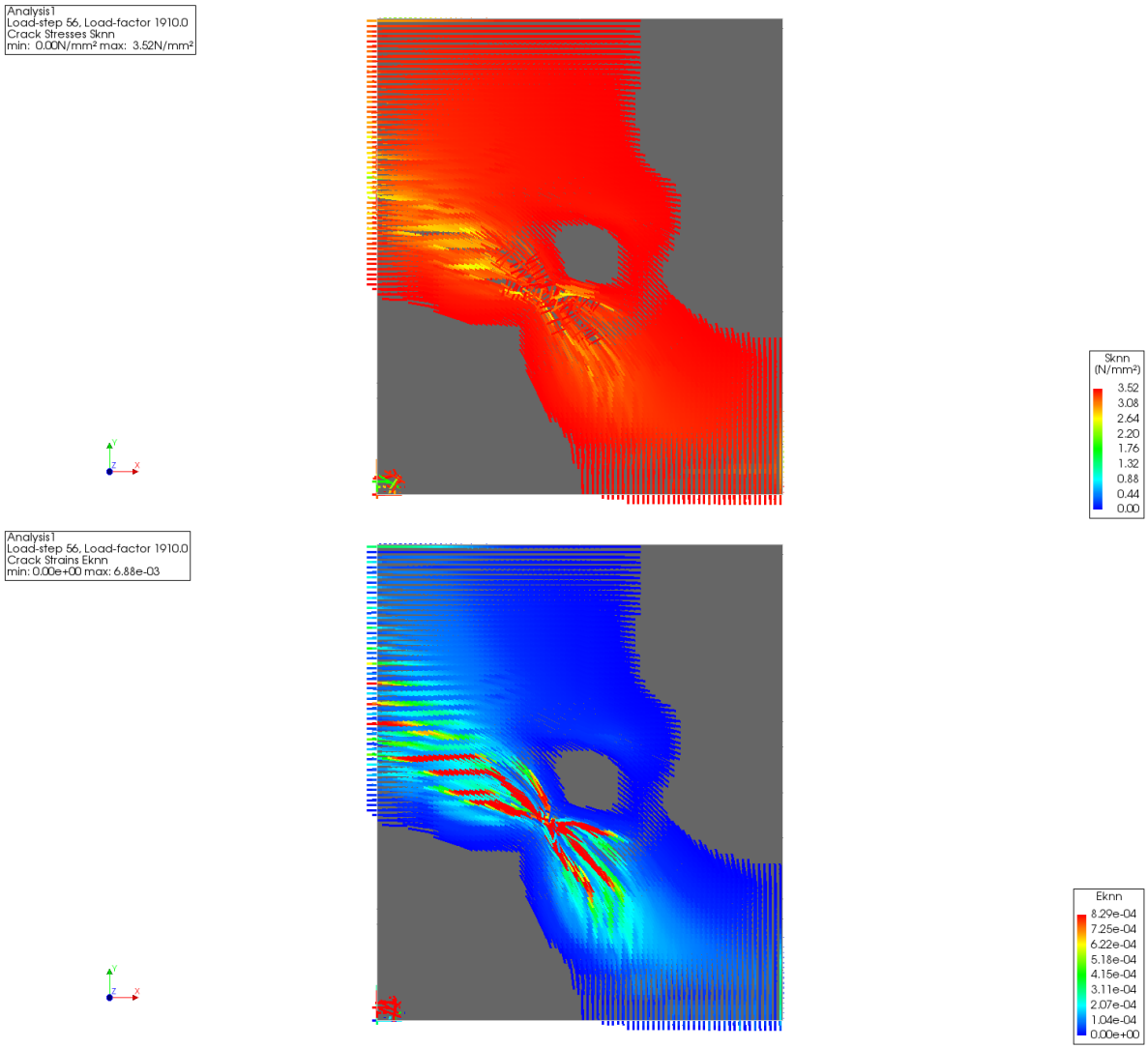

Figure 4.32: *Crack stress and strain of top surface at load 1152.6* kN *(Failure load)*

4.3.2.3 Crack evaluation

The performed finite element analysis shows a failure in the centre of the slab. This failure is characterized with a significant number of radial cracks in the bottom surface that emanate from the centre, which represent the positive yield lines, and circular cracks in the top surface, which represents the positive yield lines. This failure pattern (Figure 4.33) has a configuration similar to the “fan pattern”, described in 2.7.3.2. Additionally, the crack development of pile-supported slab subjected to point load can be seen in (appendix A.3).

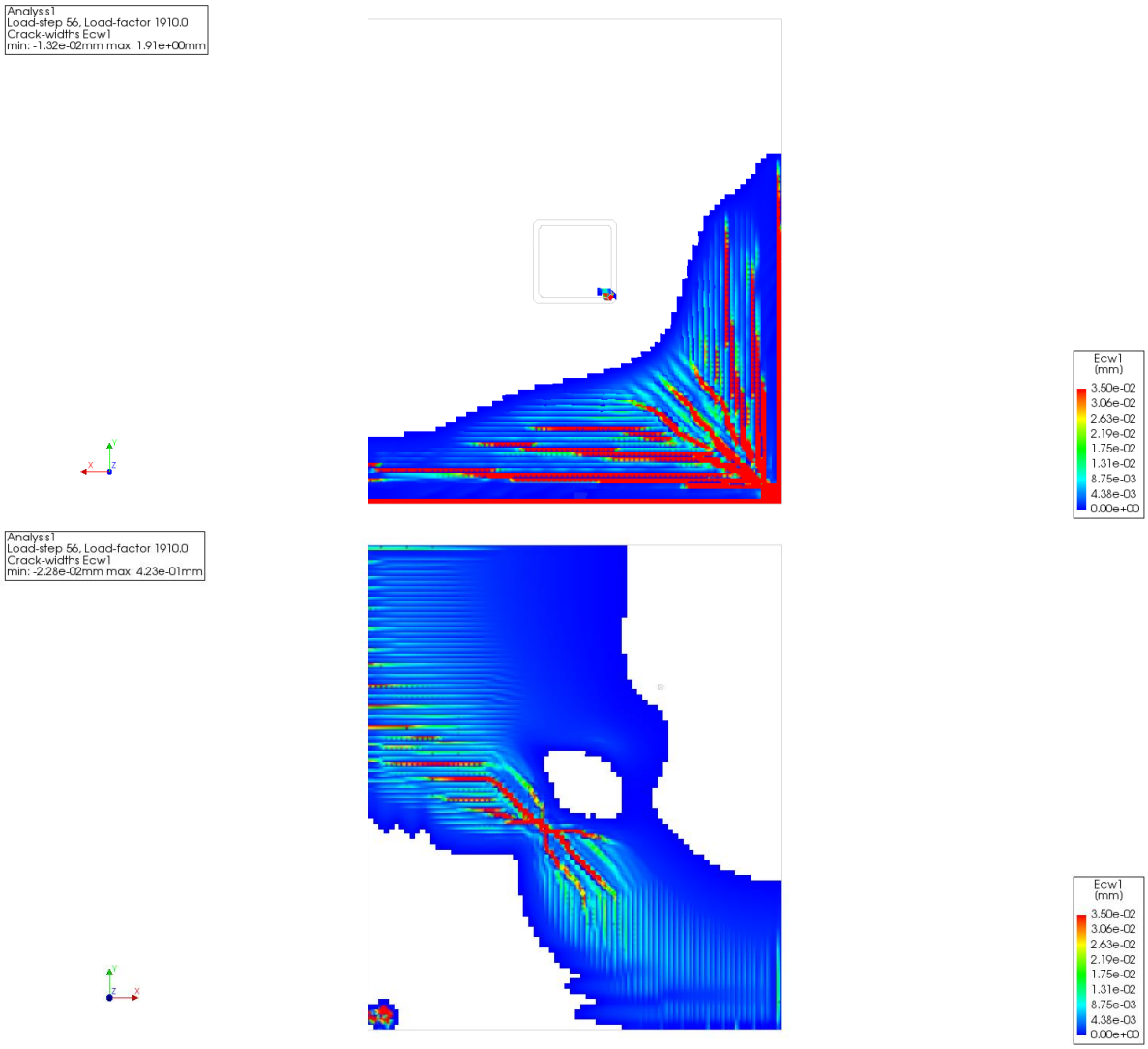

Figure 4.33: *Crack pattern for bottom surface (left) and top surface (right) of the slab under point load*

Table 4.8 shows how the crack width grows in different stages when the slab is subjected to point load.

Table 4.8: *Deflection and crack width in several stages for slab under point load*

Stage	Deflection [mm]	Crack width at top [mm]	Crack width at bottom [mm]
At stage of first crack in the bottom surface	0.90	-	0.000494
At stage of first crack in the top surface	4.14	0.00135	0.41
At stage of calculated capacity	1.99	0.13	0.72
At stage of failure	21.02	0.42	1.91

5 Conclusion

5.1 Notched beam

The notched beam was modelled to verify the material response of SFRC, i.e. the notched beam model was a tool to achieve a good fitting between the experimental data and simulated data. Thus, it can be concluded from the results of the notched beam that the AIA is a good representative for the tensile response of SFRC. On the other hand, it is known that the use of the smeared crack approach is easier and more practical in application than the use of the discrete crack approach since there is no need to define the location of the crack or assign a special material. But in case of the notched beam model, the presence of the notch forces the crack to initiate over the notch, which gives a pre-definition of the crack location. Hence, in the notched beam model, it can be concluded that there is not a big difference between the smeared crack or the discrete crack approach, but the implementation of smeared crack approach could be easier.

5.2 Round panel

The main aim of modelling the round panel was to investigate the effect of support friction on its structural behaviour. It can be concluded from the results that the presence of any kind of friction between the round panel and its continuous support results in an increase of the post-cracking capacity, due to friction forces (restraining) and this may not then reflect the actual post-cracking capacity. Hence, in the round panel test, it is recommended to have a frictionless contact zone between the round panel and its continuous support, since the presence of frictional contact zone results in restraining the round panel thus overestimating the post-cracking capacity due to arching action. Several choices are available to model the round panel test, and the selected choice could affect the computation time as well as the result. The use of two-dimensional elements led to a slightly increase of the post-cracking capacity of the round panel at smaller deflections, but the use of two-dimensional elements reduced the computation time, significantly. Moreover, the results displayed that the effect of mesh order is almost negligible in both cases, two-dimensional elements and three-dimensional elements.
Hence, it is recommended to use two-dimensional elements to model the round panel if the purpose is to investigate the structural behaviour, whereas to investigate the crack pattern and crack width, three-dimensional elements are recommended.

5.3 Pile supported slab

The main aim of modelling the pile-supported slab was to investigate the effect of arching action phenomenon. It can be concluded from the results that the arching action phenomenon may play a significant role in determining the capacity of a pile-supported slab if it is laterally restrained (interior panel). Furthermore, in comparison to the calculated load resistance based on YLT and pure bending, the results of FEA, which considered the arching action effect, showed a load resistance increase of 322 per cent in case of uniformly distributed load and 172 per cent in case of point load. This increase is mainly due to the arching action phenomenon and other reasons such as the implementation of drop panel in FEA. Up to now, there is no clear approach to include the effect of arching action, which is a favourable effect, in the design. Therefore, it is recommended to include the effect of arching action in deriving future design approaches, since that would lead to a more economical design.

5.4 Suggestion for future research

Steel fibres enhance the ductility of concrete and improve the flexural behaviour, which has been investigated in this thesis. On the other hand, other benefits can be achieved by using steel fibres such as increasing the shear punching strength. Several studies have pointed out that the use of steel fibres could enhance shear strength in all reinforced concrete structures, and this enhancement could increase the shear strength up to 20 per cent. Hence, it would be interesting to examine the effect of fibre reinforcement on punching.

Moreover, several factors could impact the structural behaviour of SFRC such as fibre content, fibre geometry, water/binder ratio, concrete strength etc. In this master's thesis, only one SFRC mix has been used, and the fibre content was 0.5 per cent with a geometry of end-hook and a configuration of double bend. Hence, many factors have not been investigated, and one of these factors is the fibre content. It would be beneficial to use FE software to examine the effect of different fibre contents and investigate how the needed material behaviour can be achieved by keeping the fibre content as low as possible. In other words, it is preferable to have a flexural behaviour of deflection hardening (multiple cracks can be formed), which depends on the fibre content as well as the structural element geometry. For a certain geometry, the deflection hardening behaviour can be achieved by different fibre contents, hence the lowest fibre content that shows the needed deflection hardening behaviour is the most suitable choice.

Furthermore, creep and shrinkage are important factors that could affect the load-bearing capacity, serviceability and durability of pile-supported slabs since these two factors have a considerable effect on crack development. Therefore, it would be valuable to implement a non-linear finite element analysis to investigate cracking in pile-supported slabs due to creep and shrinkage and to which extent the use of steel fibre could enhance the creep and shrinkage behaviour of pile-supported slabs.

References

Abid, A. & Franzén, K. B., 2011. *Design of Fibre Reinforced Concrete Beams and Slabs,* Gothenburg, Sweden: Chalmers University of Technology / Department of Civil and Environmental Engineering.

ACI, 2004. *Report on Design and Construction of Steel Fiber-Reinforced Concrete Elevated Slabs,* New York, USA: American Concrete Institute.

ASTM C1550-12a, 2012. *Standard Test Method for Flexural Toughness of Fiber Reinforced Concrete (Using Centrally Loaded Round Panel),* West Conshohocken, PA, USA: ASTM International.

Beeby, A. W. & Fathibitaraf, F., 2001. Membrane effect in the reinforced concrete frames - a proposal for change in the design of frames structures. *Engineering Structures,* 23(1), pp. 82-93.

Belletti, B. & Vitulli, F., 2014. Compressive membrane action in confined RC and SFRC circular slabs. Issue 2005, pp. 807-818.

Bernard, E. S., 2000. Behaviour of round steel fibre reinforced concrete panels under point loads. *Materials and Structures/Matériaux et Constructions,* Volume 33, pp. 181-188.

Berrocal, C. G., 2017. *Corrosion of steel bars in fibre reinforced concrete: Corrosion mechanisms and structural performance,* Gothenburg, Sweden: Chalmers University of Technology / Department of Civil and Environmental Engineering.

Bjøntegaard, Ø., 2010. *Energy absorption capacity for SFRC. Effect of panel prod. technique, fibre content and friction in round panel tests with continuous steel support (Series 8 and 9),* Oslo, Norway: Statens vegvesen.

Blanco, A. et al., 2013. Application of constitutive models in European codes to RC-FRC. *Construction and Building Materials, ELSEVIER,* 40(March), pp. 246-259.

Burgers, R., 2006. *Non-linear FEM modelling of steel fibre reinforced concrete for the analysis of tunnel segments in the thrust jack phase,* Delft, Netherlands: Delft University of Technology / Faculty of Civil Engineering and Geosciences.

Cen, W. J., Wang, H. & Sun, Y. J., 2018. Laboratory investigation of shear behavior of high-density polyethylene geomembrane interfaces. *Polymers,* 10(7), pp. 0-14.

Criswell, M., 1974. Static and Dynamic Response of Reinforced Concrete Slab-Column Connections. *ACI,* Volume 42, pp. 721-746.

DBV, 2001. *Merkblatt Stahlfaserbeton,* Fassung, Germany: Deutsche Beton Vereins.

Desayi, P. & Kulkarni, A. B., 1977. Membrane action, deflections and cracking of two-way reinforced concrete slabs. *Matériaux et Constructions,* 10(5), pp. 303-312.

Destrée, X., 2004. Structural Application of Steel Fibre as Only Reinforcing in Free Suspended Elevated Slabs: Conditions-Design-Examples. *6th RILEM Symposium on Fibre-Reinforced Concretes (FRC)- BEFIB 2004,* pp. 1073-1082.

Destrée, X., 2006. Concrete Free Suspended Elevated Slabs Reinforced with Only Steel Fibers: Full Scale Testing Results and Conclusions - Design Examples. *RILEM Proceedings PRO49,* pp. 287-294.

Di Prisco, M., Colombo, M. & Dozio, D., 2013. Fibre-reinforced concrete in fib Model Code 2010: Principles, models and test validation. *Structural Concrete,* 14(4), pp. 342-361.

Ebelechukwu, O. C., Johnson, B. O., Michael, A. I. & Fidelis, A. T., 2018. Comparison of Some Iterative Methods of Solving Nonlinear Equations. *International Journal of Theoretical and Applied Mathematics,* 4(2), pp. 22-28.

EHE-08, 2008. *Code on Structural Concrete, Articles and Annexes,* Madrid, Spain: Spanish code on structural concrete.

EN 14651, B., 2005. Test method for metallic fibered concrete - Measuring the flexural tensile strength (limit of proportionality (LOP), residual). *British Standards Institute,* Volume 3, pp. 1-17.

EN 14889-1, 2006. Fibres for concrete - Part 1: Steel fibres. Definition, specifications and conformity. *CEN European Committee for Standardization, Brussels.,* Ref. No. EN 14889-1:2006: E(August).

EN 14889-2, 2006. Fibres for concrete - Part 2: Polymer fibres - Definition, specification and conformity. *CEN European Committee for Standardization, Brussels,* Ref. No. EN 14889-2:2006: E(August).

Ericsson, S. & Farahaninia, K., 2010. *Punching Shear in Reinforced Concrete Slabs Supported on Edge Steel Columns,* Gothenburg, Sweden: Chalmers University of Technology / Department of Civil and Environmental Engineering.

Eriksson, I. & Karlsson, N., 2016. *Non-Linear Assessment of a Concrete Bridge Slab Loaded to Failure,* Stockholm, Sweden: KTH Royal Institute of Technology.

Fall, D., 2014. *Steel Fibres in Reinforced Concrete Structures of Complex Shapes,* Gothenburg, Sweden: Chalmers University of Technology / Department of Civil and Environmental Engineering.

Fall, D. et al., 2012. *Non-linear Finite Element Analysis of Steel Fibre Reinforced Beams with Conventional Reinforcement.* Gothenburg, Sweden, Chalmers University of Technology.

Fall, D., Rempling, R. & Lundgren, K., 2013. Experiments on Fibre Reinforced Concrete Two-way Slabs. *Fibre Concrete 2013,* pp. 1-10.

fib, 2013. *fib Model Code for Concrete Structures 2010, Fédération Internationale du Béton,* Lausanne, Switzerland: Ernst & Sohn.

Gorst, J. S., Williamson, S. J., Pallett, P. F. & Clark, L. A., 2003. *Research Report 071: Friction in temporary works,* Birmingham, UK: HSE.

H. Falkner, U. G., 1999. Pile supported reinforced or prestressed SFRC ground slabs. *Third International RILEM Workshop on High Performance Fiber Reinforced Cement Composites,* Issue Mainz, Germany, pp. 595-602.

Hedebratt, J., 2012. *Industrial Fibre Concrete Floors, Experiences and tests on pile-supported slabs,* Stockholm, Sweden: KTH Royal Institute of Technology.

Hedebratt, J. & Silfwerbrand, J. L., 2004. An Innovative Approach to the Design of Pile Supported SFRC Slabs. *RILEM Symposium on Fibre Reinforced Concrete,* pp. 945-954.

Hillerborg, A., 1980. Analysis of fracture by means of the fictitious crack model, particularly for fibre reinforced concrete. *International journal of cement composites,* 2(4), pp. 177-184.

Hillerborg, A., Modéer, M. & Petersson, P. E., 1976. Analysis of crack formation and crack growth in concrete by means of fracture mechanics and finite elements. *Cement and Concrete Research,* 6(6), pp. 773-781.

Hsueh, P.-K., 1966. *Yield-line theory for concrete slabs,* Kansas, USA: Kansas State University / Department of Civil Engineering.

Irani, F. & Abadi, B. M., 2013. *Finite element analysis of conventional and fiber reinforced concrete slabs,* Gothenburg, Sweden: Chalmers University of Technology / Department of Civil and Environmental Engineering.

Jansson, A., 2008. *Fibres in reinforced concrete structures - analysis, experiments and design,* Gothenburg, Sweden: Chalmers University of Technology / Department of Civil and Environmental Engineering.

Jepsen, M. S., Damkilde, L. & Löfgren, I., 2016. A fully general and adaptive inverse analysis method for cementitious materials. *Materials and Structures/Materiaux et Constructions,* 49(10), pp. 4335-4348.

Jepsen, M. S., Damkilde, L., Lövgren, I. & Berrocal, C., 2018. Adaptive inverse analysis (AIA) applied and verified on various fiber reinforced concrete composites. *Materials and Structures/Materiaux et Constructions,* 51(3), pp. 1-11.

Jirásek, M. & Bauer, M., 2012. Numerical aspects of the crack band approach. *Computers and Structures,* Volume 110-111, pp. 60-78.

Johansen, K. W., 1972. *Yield-line formulae for slabs,* London, UK: Cement and Concrete Association.

Kasper, T. et al., 2014. *Design Guideline for Structural Applications of Steel Fibre Reinforced,* Denmark: SFRC consortium.

Kaur, P. & Talwar, M., 2017. Different types of Fibres used in FRC. *International Journal of Advanced Research in Computer Science,* 8(May), pp. 380-383.

Kennedy, G. & Goodchild, C., 2004. *Practical Yield Line Design: An introduction to the practical use of Yield Line Theory in the design of flat slabs, raft foundations and refurbishment.* London, UK: The Concrete centre.

Lee, S.-C., Oh, J.-H. & Cho, J.-Y., 2015. Compressive behavior of fiber-reinforced concrete with end-hooked steel fibers. *Materials,* 8(4), pp. 1442-1458.

Löfgren, I., 2005. *Fibre-reinforced Concrete for Industrial Construction- a fracture mechanics approach to material testing and structural analysis,* Gothenburg, Sweden: Chalmers University of Technology / Department of Civil and Environmental Engineering.

Maalej, M., Li, V. C. & Members, A., 1995. Flexural Strength of Fiber Cementitious Composites. pp. 390-406.

Maekawa, K., Okamura, H. & Pimanmas, A., 2003. *Non-Linear Mechanics of Reinforced Concrete.* 1st ed. London, UK: Taylor and Francis Group.

Malm, R., 2015. *Non-Linear Analyses of Concrete Beams with Abaqus,* Stockholm, Sweden: KTH Royal Institute of Technology.

Milne, I. R. & R.O. Karihaloo, B., 2003. Comprehensive Structural Integrity. *Elsevier,* Volume 1-10, p. 529.

Naaman, A. E., 2003. Engineered Steel Fibers with Optimal Properties for Reinforcement of Cement Composites. *Journal of Advanced Concrete Technology,* 1(3), pp. 241-252.

Neves, R. D. & Fernandes de Almeida, J. C., 2005. Compressive behaviour of steel fibre reinforced concrete. Structural Concrete. 6(1), pp. 1-8.

Nilsson, U., 2001. Load Bearing Capacity of Steel Fibre Reinforced Shotcrete Linings. *Workshop Proceeding From a Nordic Miniseminar,* Issue June, pp. 93-102.

Oikonomou-Mpegetis, S., 2013. *Behaviour and Design of Steel Fibre Reinforced Concrete Slabs,* London, UK: Imperial College London / Department of Civil and Environmental Engineering / Structural Engineering Research Group.

Plos, M., 1996. *Finite Element Analyis of Concrete Structures.* 1st ed. Gothenburg,Sweden: Department of Structural Engineering, Chalmers University of Technology.

RILEM-TC-162-TDF, 2002. Test and design methods for steel fibre reinforced concrete. Design of steel fibre reinforced concrete using the σ-w method: principles and applications. *Materials and Structures,* 35(5), pp. 262-278.

RILEM-TC-162-TDF, 2003. Test and design methods for steel fibre reinforced concrete sigma-epsilon-design method. *Materials and Structrues,* 36(262), pp. 560-567.

Rots, J., 1998. *Computational Modeling of Concrete Fracture,* Delft, Netherlands: Delft University of Technology / Civil Engineering and Geosciences.

Shu, J. et al., 2015. Development of modelling strategies for two-way RC slabs. *ELSEVIER*, Volume 101, pp. 439-449.

Silfwerbrand, J., 2017. Load tests on industrial steel fibre concrete floors. *XXIII Nordic Concrete Research Symposium,* pp. 53-56.

Soranakom, C. & Mobasher, B., 2015. Flexural Design of Fiber-Reinforced Concrete Flexural Design of Fiber-Reinforced Concrete. *ACI Materials Journal ,* Issue September 2009, pp. 461-469.

Soranakom, C., Mobasher, B. & Destree, X., 2007. Numerical simulation of FRC round panel tests and full-scale elevated slabs. *ACI Special Publication,* 248(October 2014), pp. 31-40.

Stephen, S. J., Raphael, B., Gettu, R. & Jose, S., 2019. Determination of the tensile constitutive relations of fiber reinforced concrete using inverse analysis. *Construction and Building Materials,* Volume 195, pp. 405-414.
The concrete society, 2013. *Concrete*
Industrial Ground Floors" A Guide to Design and Construction, 4th edition, London: The Concrete Society.

Thorenfeldt, E., Tomaszewicz, A. & Jensen, J. J., 1987. *Mechanical properties of high-strength concrete and applications in design.* Stavanger, Norway, Conference on Utilization of High-Strength Concrete.

Tlemat, H., Pilakoutas, K. & Neocleous, K., 2006. Modelling of SFRC using inverse finite element analysis. *Materials and Structures,* 39(286), pp. 221-233.

TNO DIANA, 2017. *Finite Element Analysis, User's Manual Release 10.2,* Delft, Netherlands: Available at: tnodiana.com.

TNO DIANA, 2018. *Nonlinear Analysis of a Concrete Slab under Cyclic Transverse Load,* Delft, Netherlands: TNO DIANA.

TNO DIANA, 2019. *Bending Test on a Fiber-Reinforced Concrete Notched Beam,* Delft, Netherlands: TNO DIANA.

TNO DIANA, 2019. *DIANA FEA.* [Online] Available at: https://dianafea.com/index.php/faq-tangent-normal-stiffness [Accessed 2019].

Vandervalle, M., 1991. Dramix Tunnelling the World, with 7 reference projects. *Zwevegem: NV Bekaert.*

Vecchio, F. & Collins, M., 1993. Compression response of cracked reinforced concrete. *Journal of structural engineering,* Volume 119, pp. 3590-3610.

Venkateshwaran, A. & Tan, K. H., 2018. Arching Action in Steel Fiber-Reinforced Concrete Flat Slabs. *ACI Structural Journal,* 115(6), pp. 1765-1776.

Zandi, K., Kettilb, P. & Lundgren, K., 2007. Modeling the Structural Behavior of Frost-damaged Reinforced Concrete Structures. *International Journal of Operations and Production Management,* 27(1), pp. 90-107.

Østergaard, L., 2003. *Early Age Fracture Mechanics and Cracking of Concrete: Experiments and Modelling,* Lyngby, Denmark: Technical University of Denmark (DTU). BYG-Rapport, No. R-070.

Appendix A Crack development

A.1 Crack development of round panel

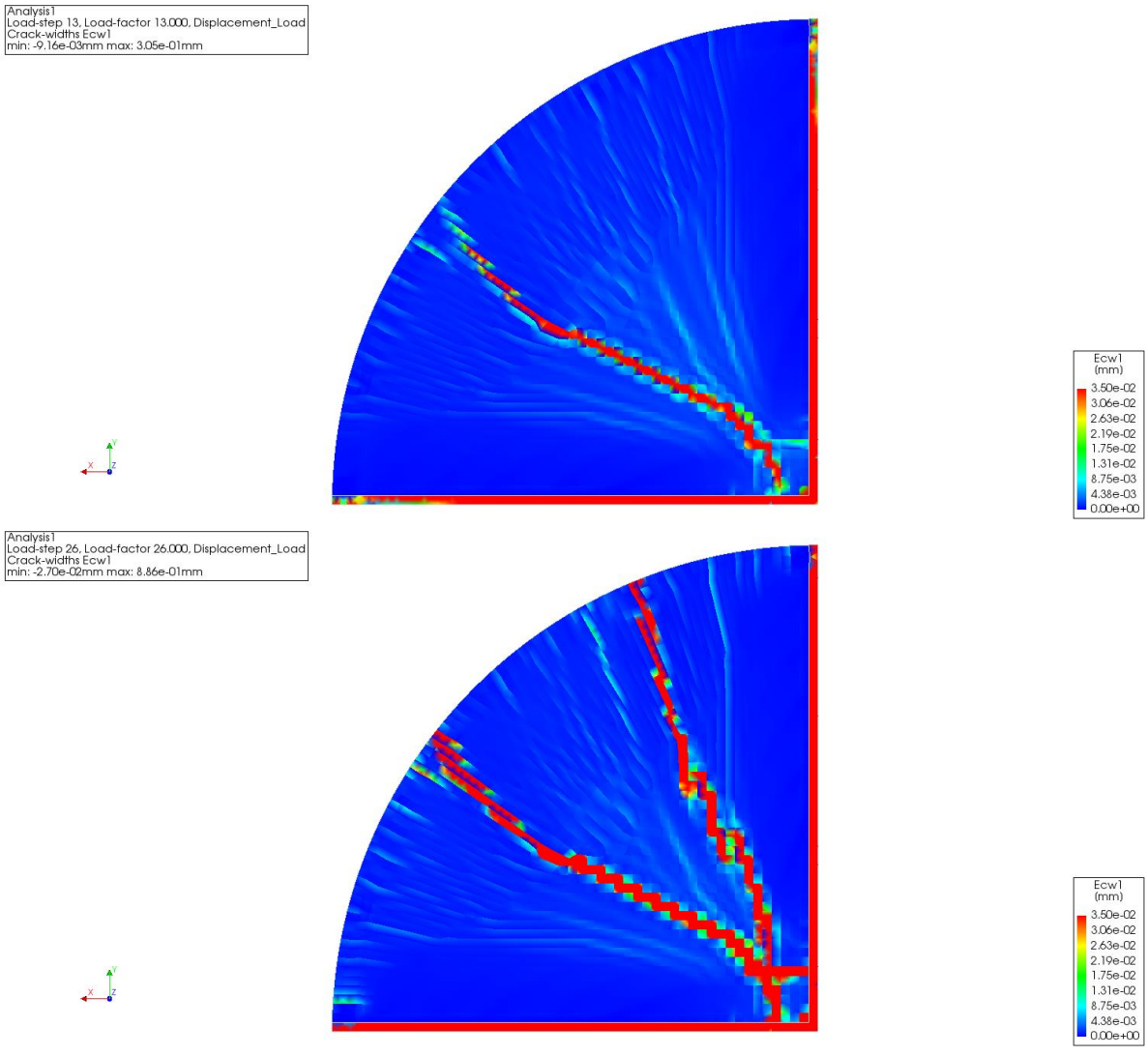

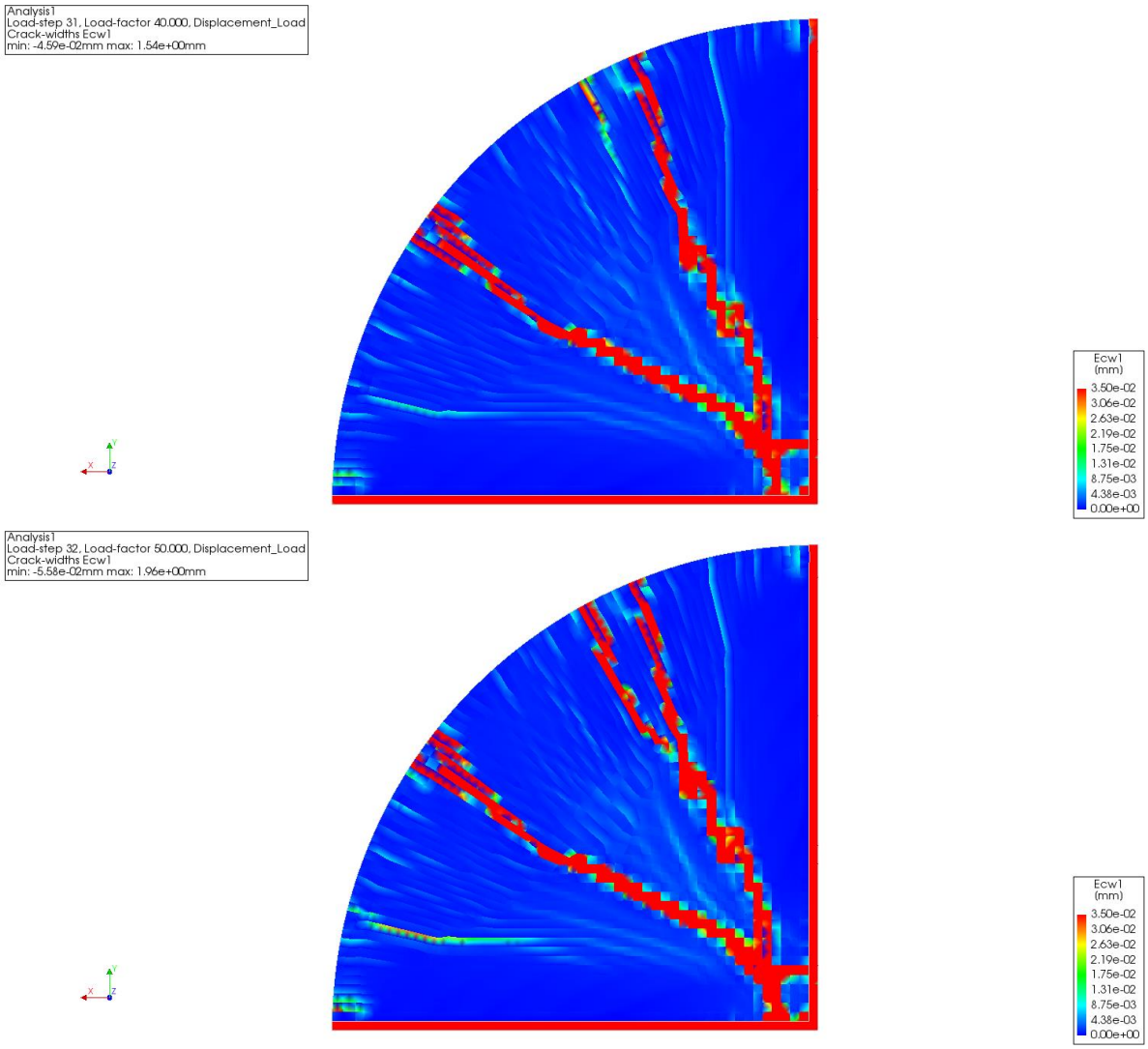
Analysis1
Load-step 31, Load-factor 40.000, Displacement_Load
Crack-widths Ecw1
min: -4.59e-02mm max: 1.54e+00mm
Ecw1
(mm)
3.50e-02
3.06e-02
2.63e-02
2.19e-02
1.75e-02
1.31e-02
8.75e-03
4.38e-03
0.00e+00
Analysis1
Load-step 32, Load-factor 50.000, Displacement_Load
Crack-widths Ecw1
min: -5.58e-02mm max: 1.96e+00mm
Ecw1
(mm)
3.50e-02
3.06e-02
2.63e-02
2.19e-02
1.75e-02
1.31e-02
8.75e-03
4.38e-03
0.00e+00

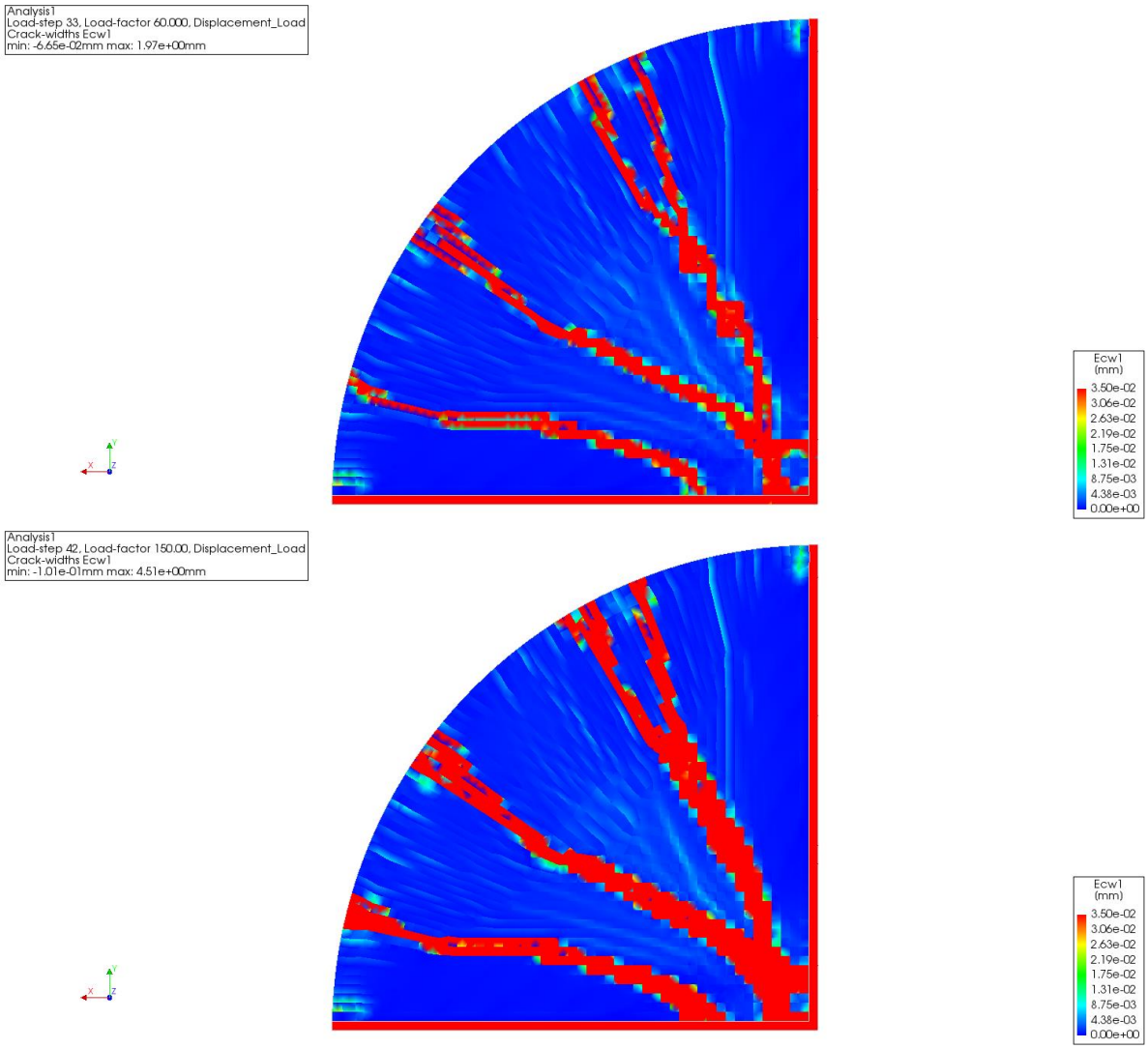

Figure A.1: *Crack development in round panel with frictionless contact zone*

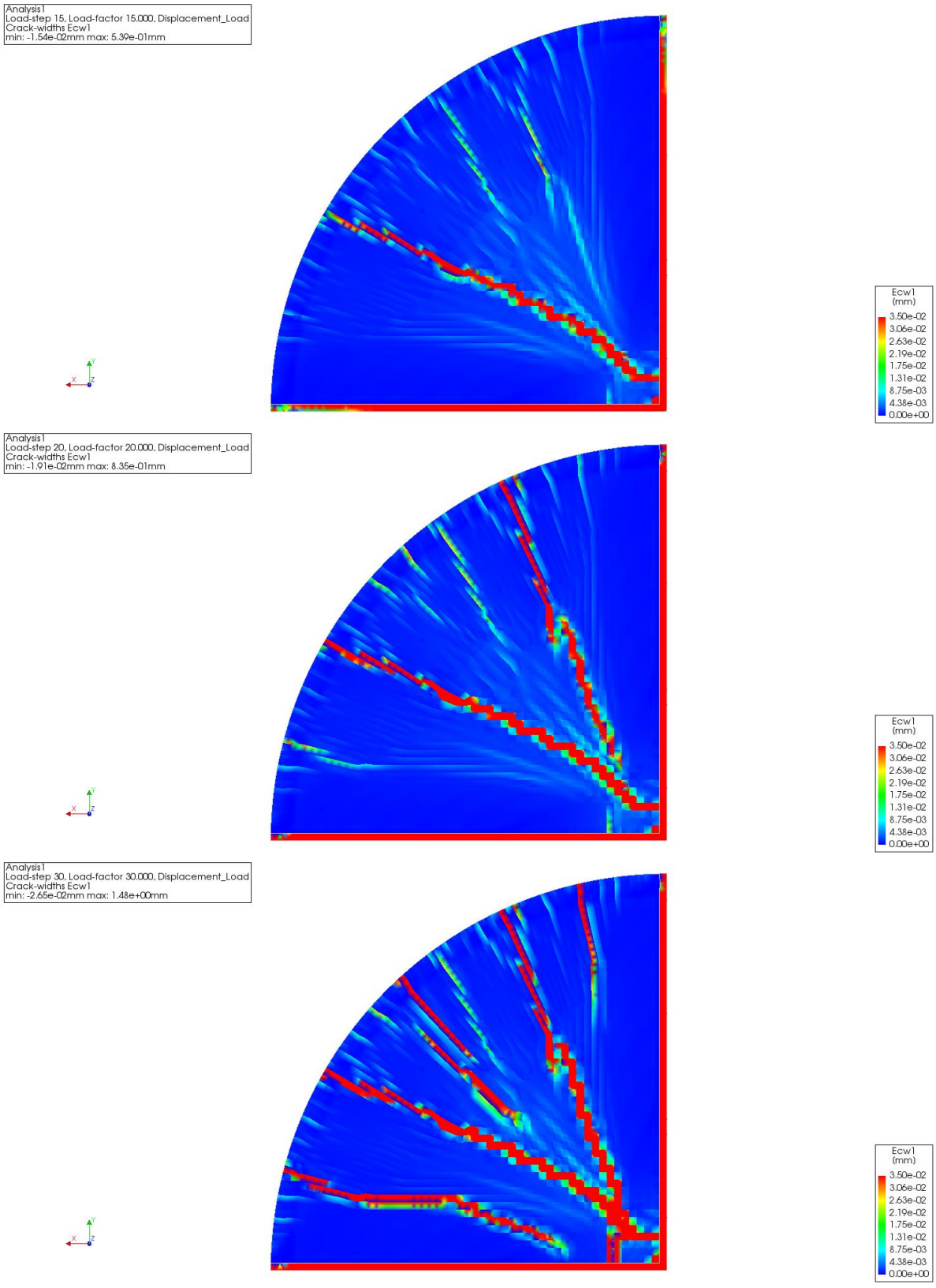
Analysis1
Load-step 15, Load-factor 15.000, Displacement_Load
Crack-widths Ecw1
min: -1.54e-02mm max: 5.39e-01mm
Ecw1
(mm)
3.50e-02
3.06e-02
2.63e-02
2.19e-02
1.75e-02
1.31e-02
8.75e-03
4.38e-03
0.00e+00
Analysis1
Load-step 20, Load-factor 20.000, Displacement_Load
Crack-widths Ecw1
min: -1.91e-02mm max: 8.35e-01mm
Ecw1
(mm)
3.50e-02
3.06e-02
2.63e-02
2.19e-02
1.75e-02
1.31e-02
8.75e-03
4.38e-03
0.00e+00
Analysis1
Load-step 30, Load-factor 30.000, Displacement_Load
Crack-widths Ecw1
min: -2.65e-02mm max: 1.48e+00mm
Ecw1
(mm)
3.50e-02
3.06e-02
2.63e-02
2.19e-02
1.75e-02
1.31e-02
8.75e-03
4.38e-03
0.00e+00

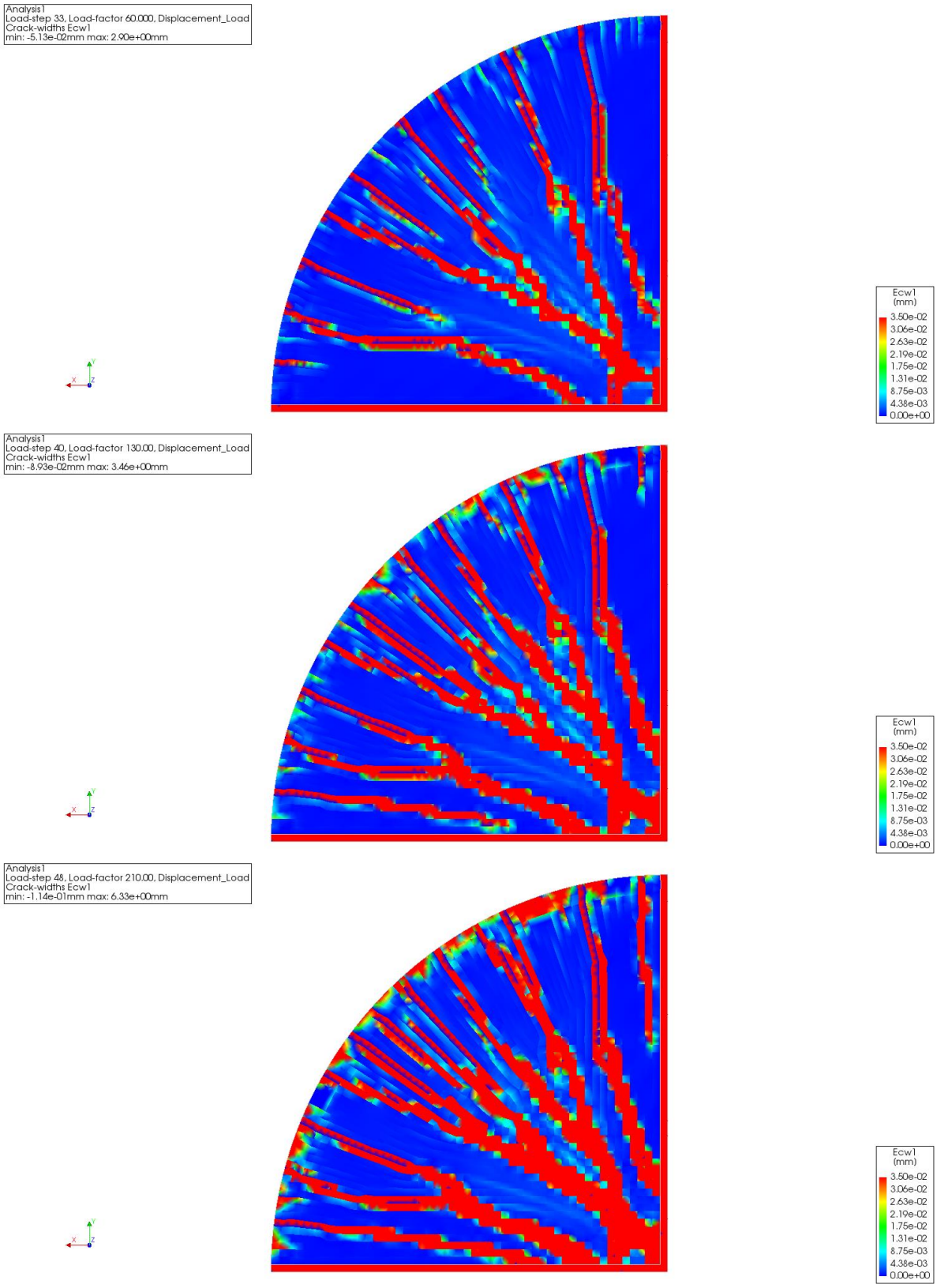

Figure A.2: *Crack development in round panel with frictional contact zone (friction coefficient of 0.1)*

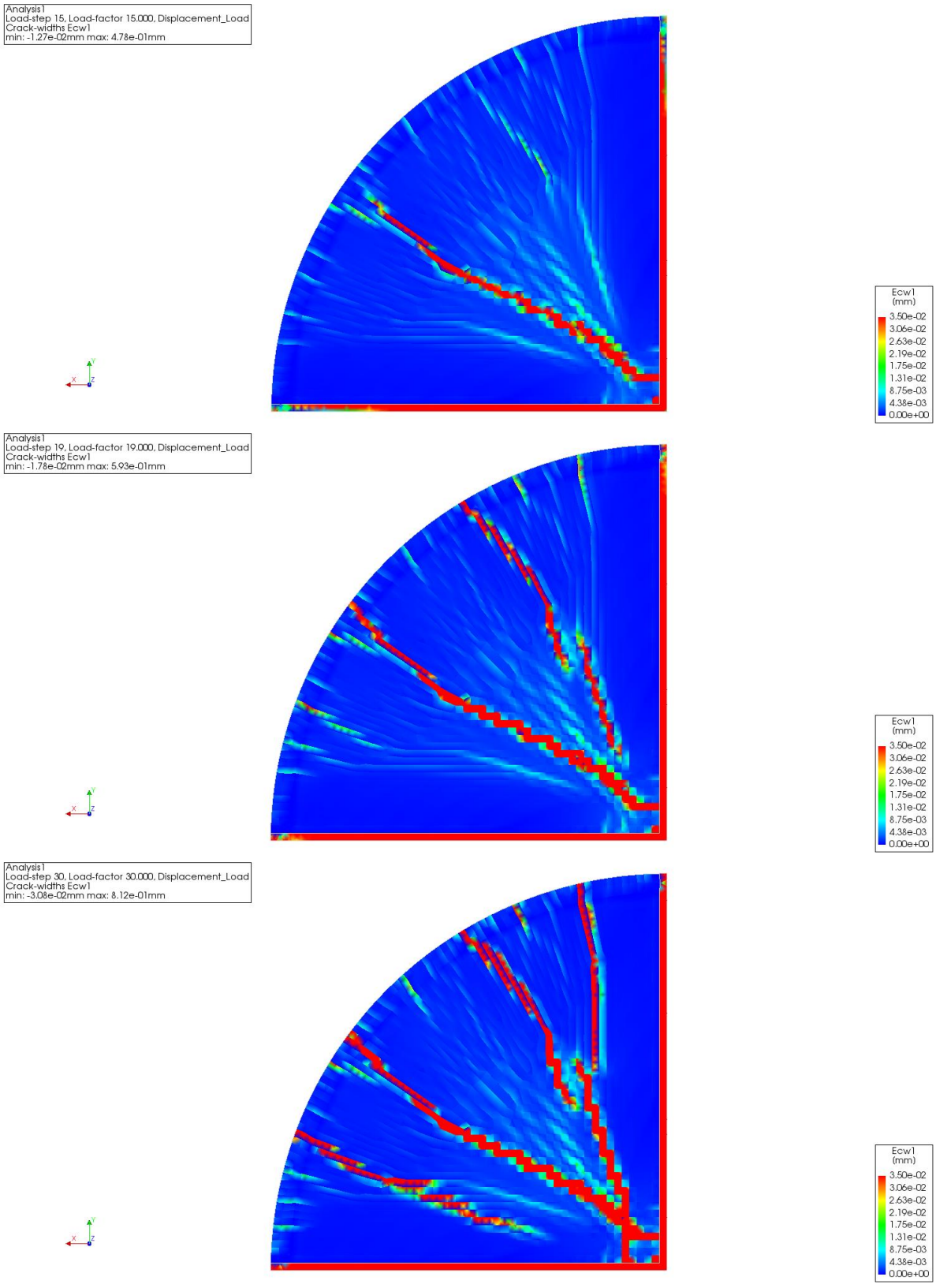
Analysis1
Load-step 15, Load-factor 15.000, Displacement_Load
Crack-widths Ecw1
min: -1.27e-02mm max: 4.78e-01mm
Ecw1
(mm)
3.50e-02
3.06e-02
2.63e-02
2.19e-02
1.75e-02
1.31e-02
8.75e-03
4.38e-03
0.00e+00
Analysis1
Load-step 19, Load-factor 19.000, Displacement_Load
Crack-widths Ecw1
min: -1.78e-02mm max: 5.93e-01mm
Ecw1
(mm)
3.50e-02
3.06e-02
2.63e-02
2.19e-02
1.75e-02
1.31e-02
8.75e-03
4.38e-03
0.00e+00
Analysis1
Load-step 30, Load-factor 30.000, Displacement_Load
Crack-widths Ecw1
min: -3.08e-02mm max: 8.12e-01mm
Ecw1
(mm)
3.50e-02
3.06e-02
2.63e-02
2.19e-02
1.75e-02
1.31e-02
8.75e-03
4.38e-03
0.00e+00

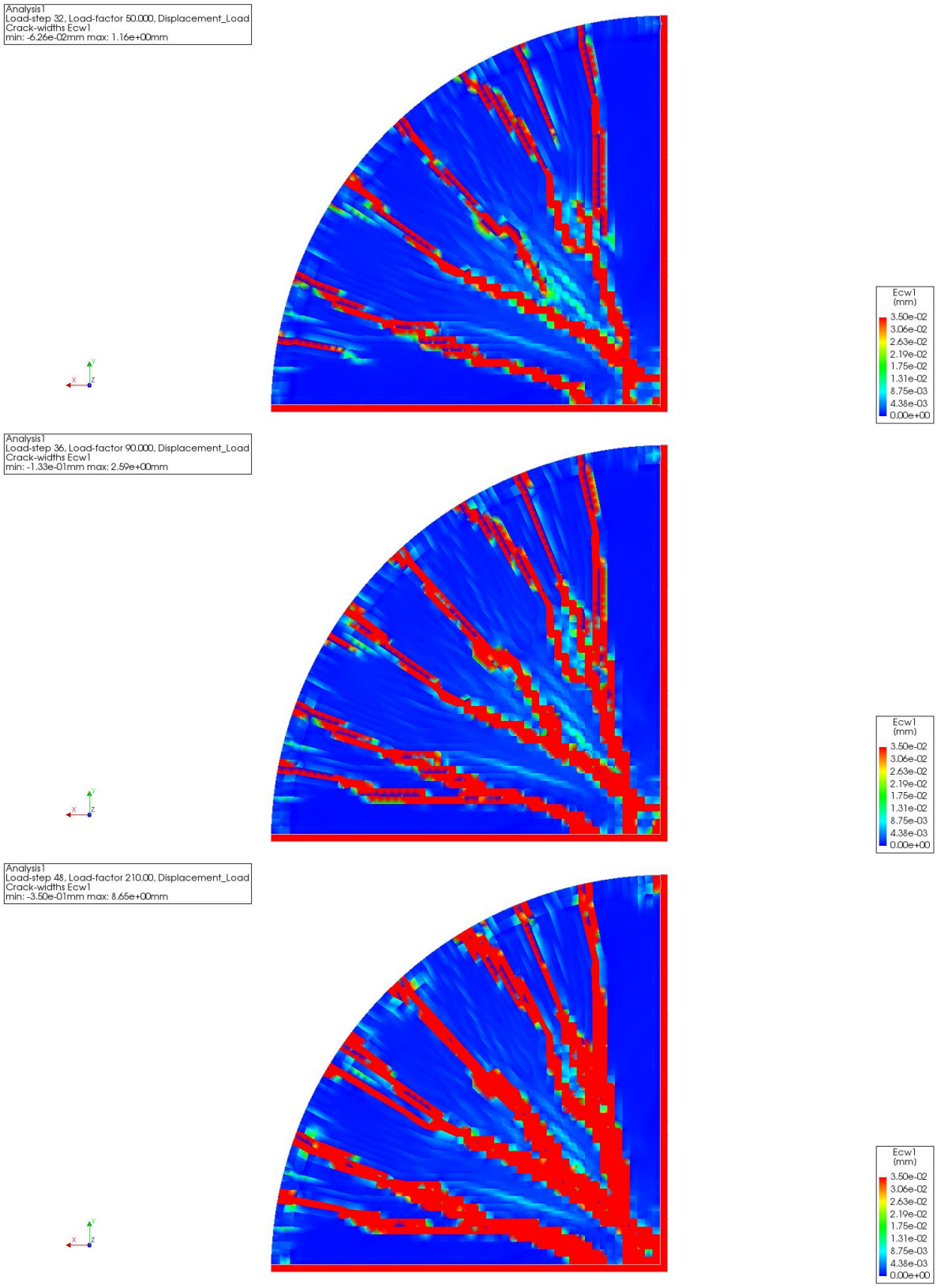

Figure A.3: *Crack development in round panel with frictional contact zone (friction coefficient of 0.4)*

Analysis1
Load-step 15, Load-factor 15.000, Displacement_Load
Crack-widths Ecw1
min: -1.81e-02mm max: 3.61e-01mm

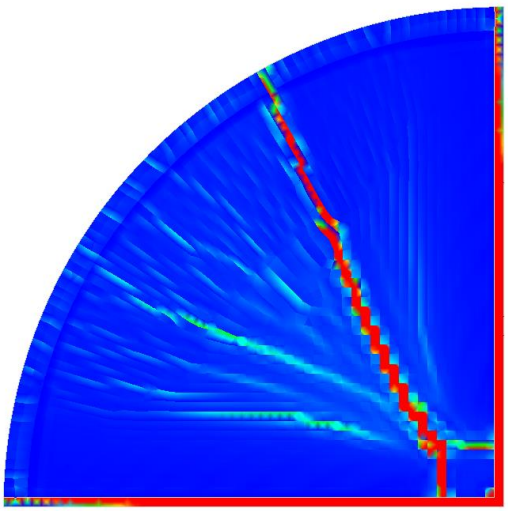

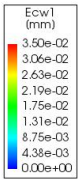

Analysis1
Load-step 23, Load-factor 23.000, Displacement_Load
Crack-widths Ecw1
min: -2.07e-02mm max: 4.84e-01mm

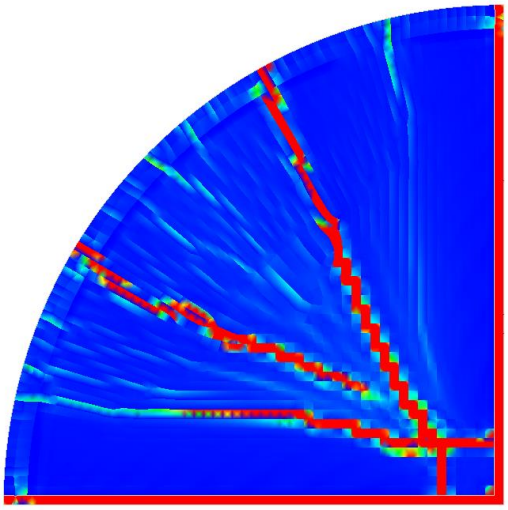

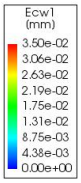

Analysis1
Load-step 30, Load-factor 30.000, Displacement_Load
Crack-widths Ecw1
min: -3.25e-02mm max: 6.97e-01mm

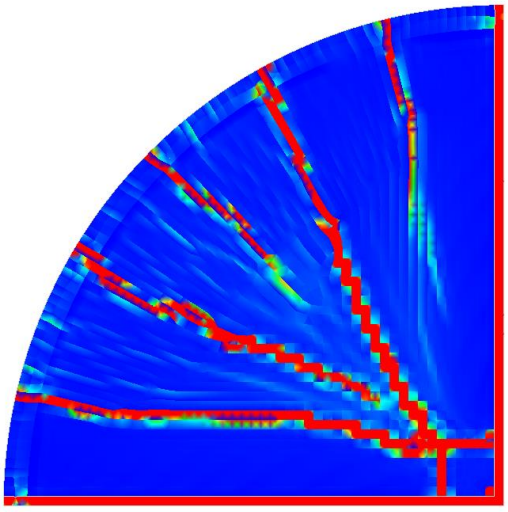

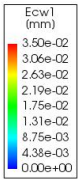

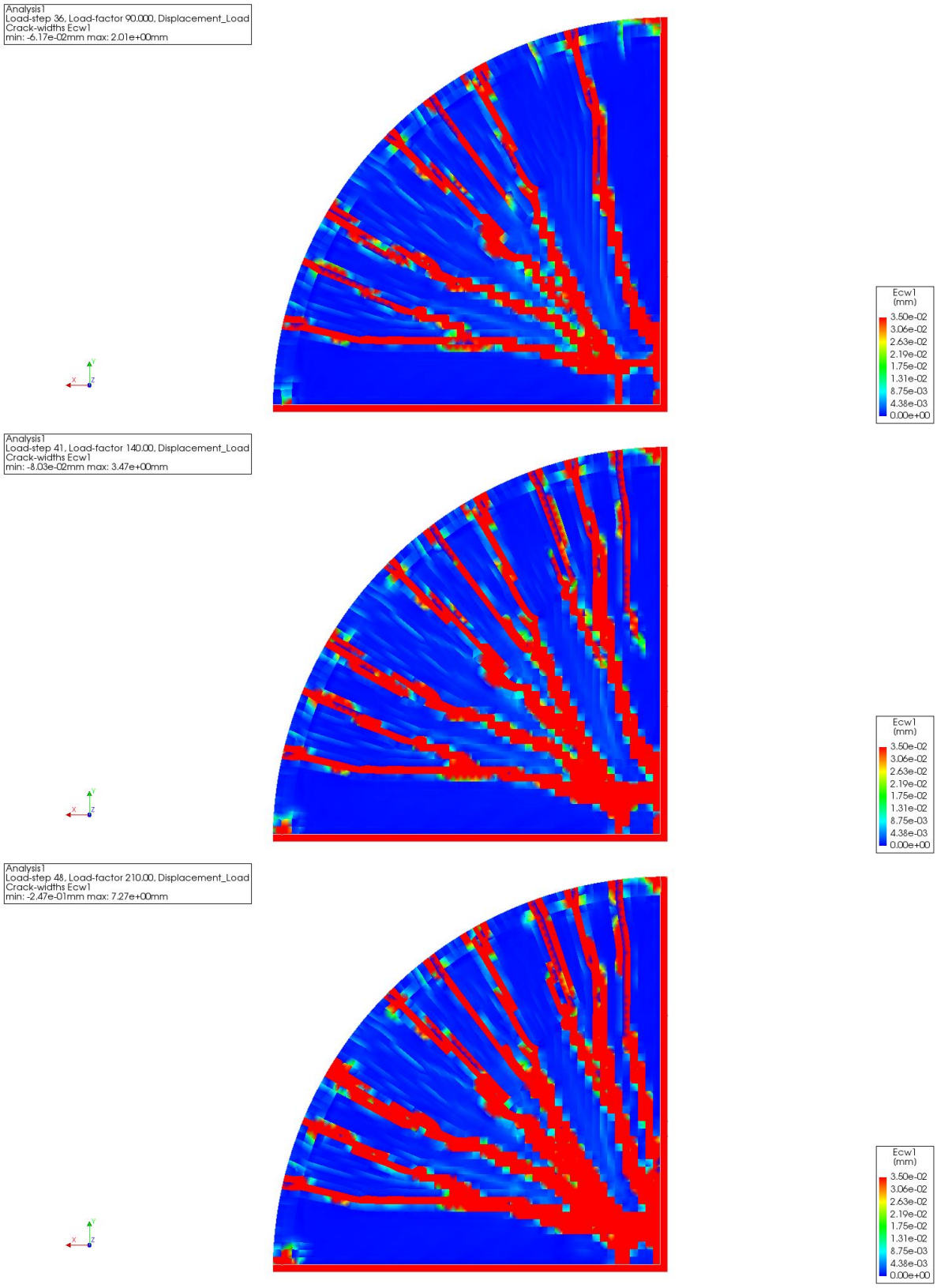

Figure A.4: *Crack development in round panel with frictional contact zone (friction coefficient of 0.8)*

A.2 Crack development of slab subjected to uniformly distributed load

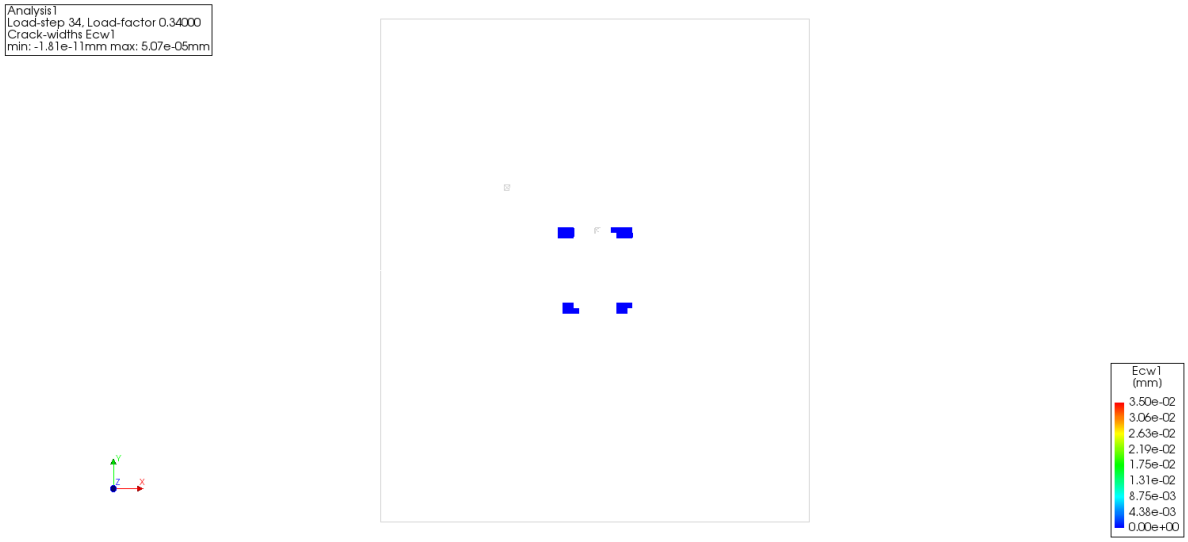

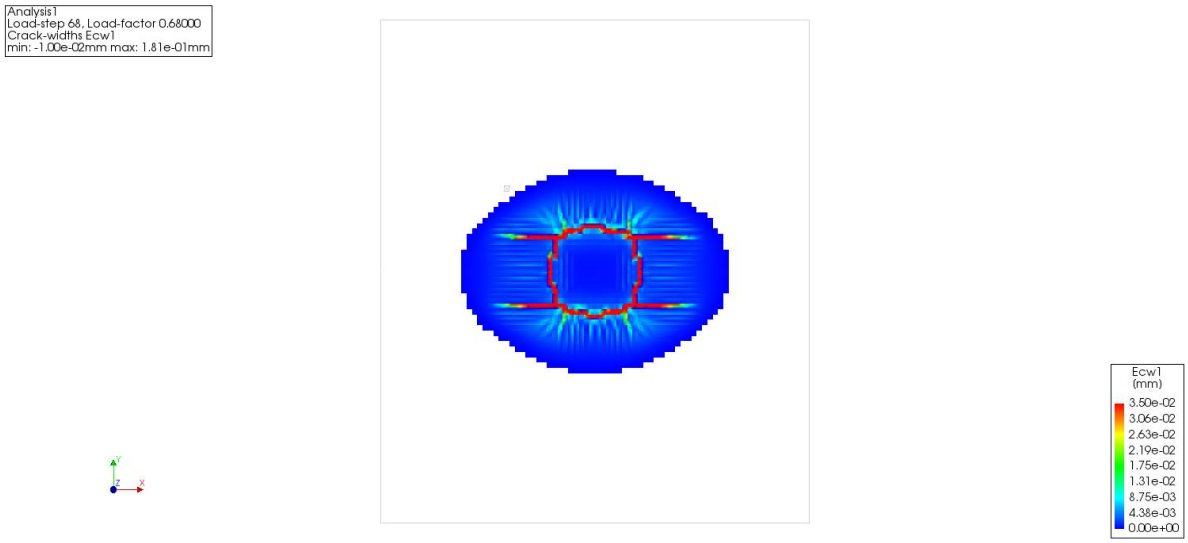

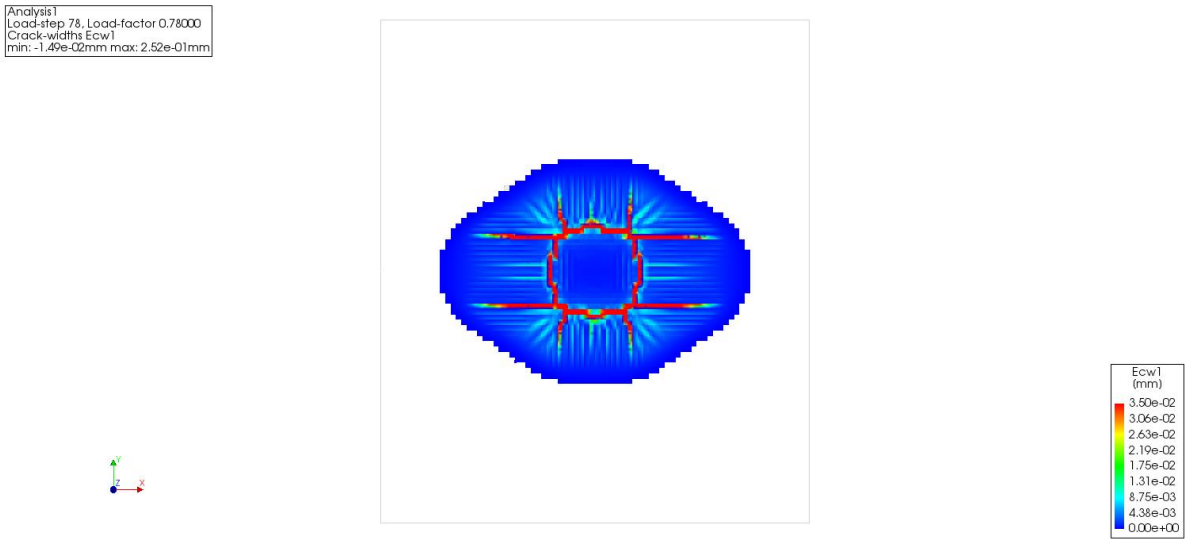

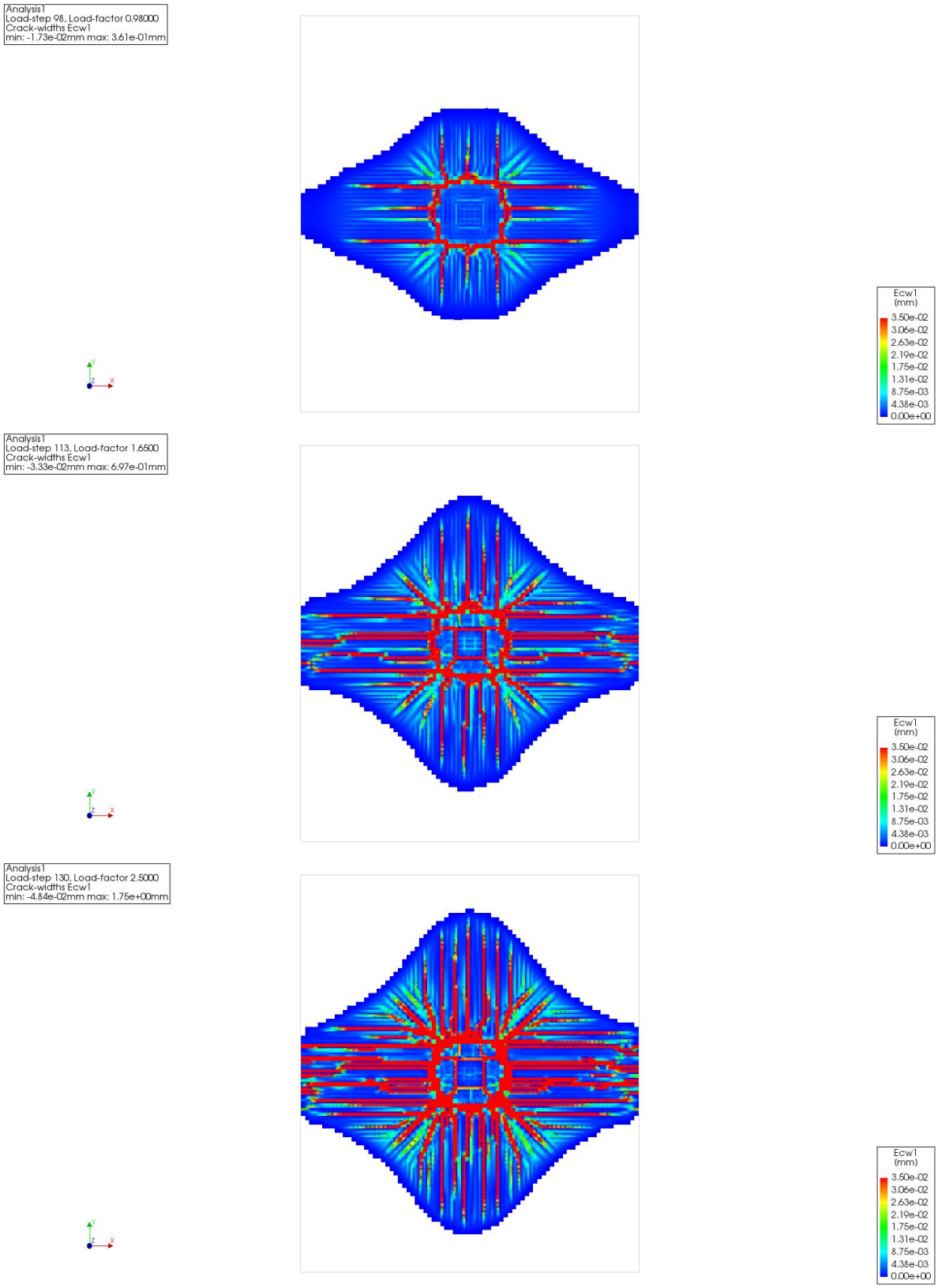

Figure A.5: *Crack development of slab subjected to uniformly distributed load (top surface)*

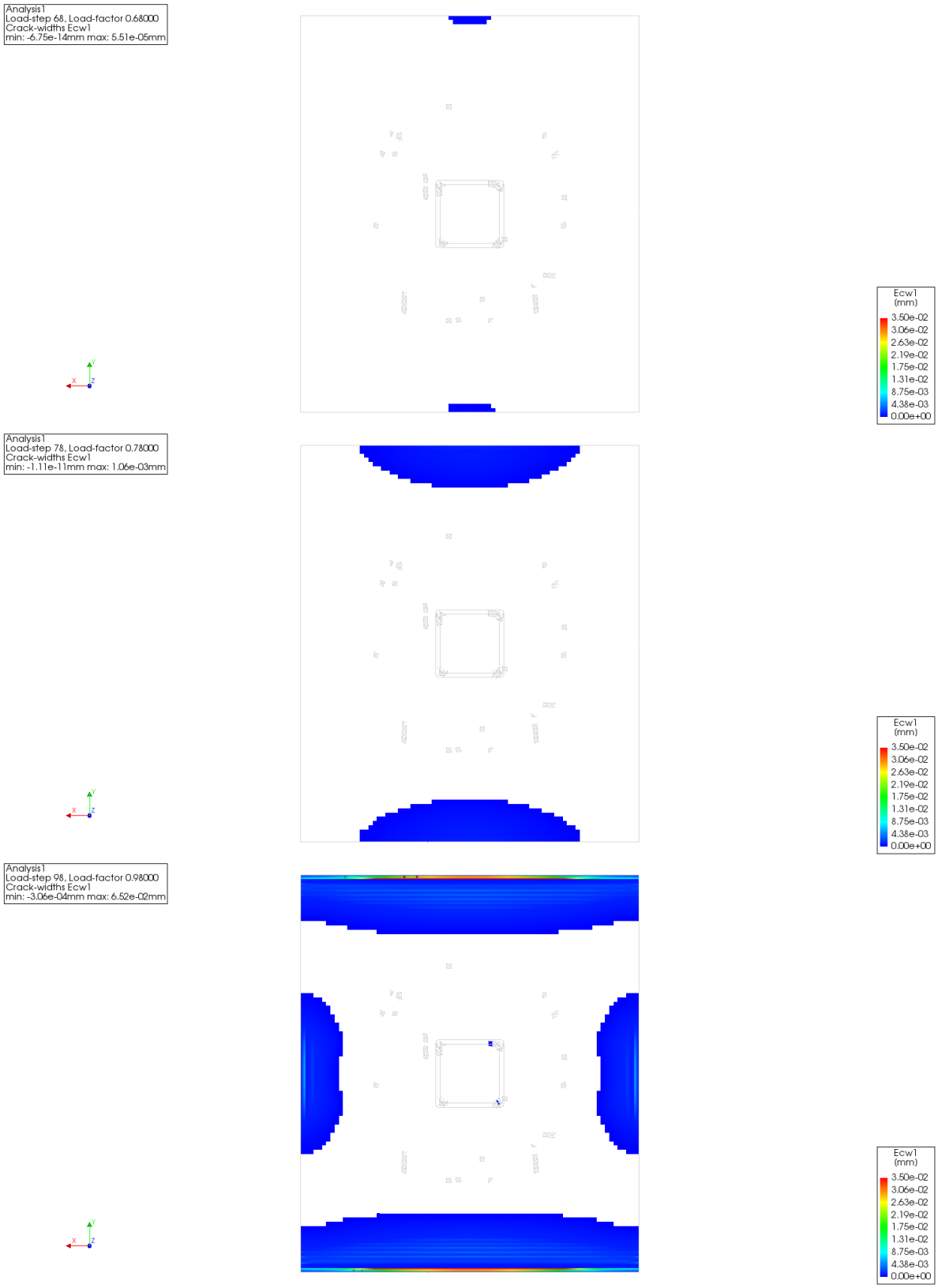
Analysis1
Load-step 68, Load-factor 0.68000
Crack-widths Ecw1
min: -6.75e-14mm max: 5.51e-05mm
Ecw1
(mm)
3.50e-02
3.06e-02
2.63e-02
2.19e-02
1.75e-02
1.31e-02
8.75e-03
4.38e-03
0.00e+00
Analysis1
Load-step 78, Load-factor 0.78000
Crack-widths Ecw1
min: -1.11e-11mm max: 1.06e-03mm
Ecw1
(mm)
3.50e-02
3.06e-02
2.63e-02
2.19e-02
1.75e-02
1.31e-02
8.75e-03
4.38e-03
0.00e+00
Analysis1
Load-step 98, Load-factor 0.98000
Crack-widths Ecw1
min: -3.06e-04mm max: 6.52e-02mm
Ecw1
(mm)
3.50e-02
3.06e-02
2.63e-02
2.19e-02
1.75e-02
1.31e-02
8.75e-03
4.38e-03
0.00e+00

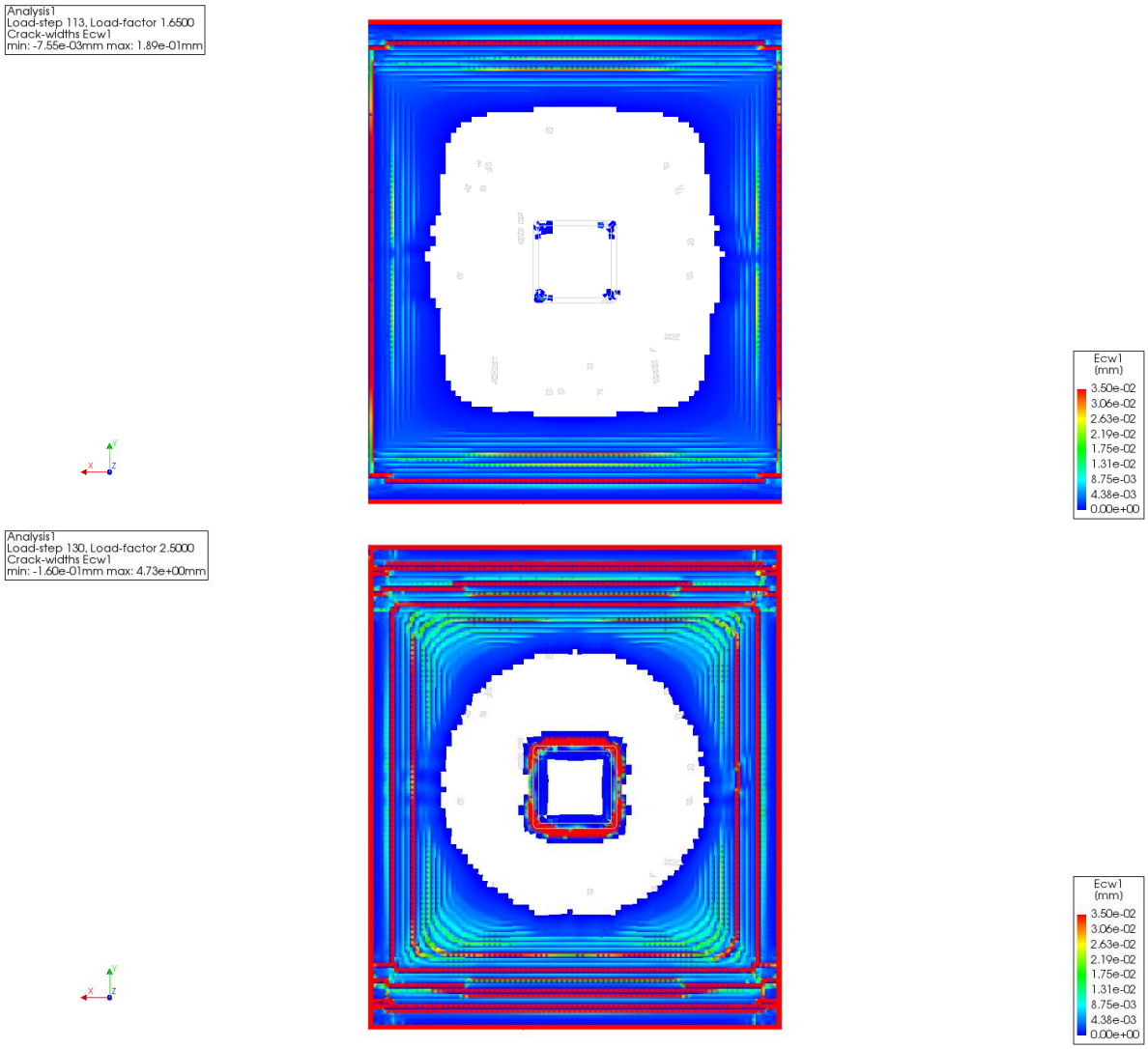

Figure A.6: *Crack development of slab subjected to uniformly distributed load (bottom surface)*

A.3 Crack development of slab subjected to point load

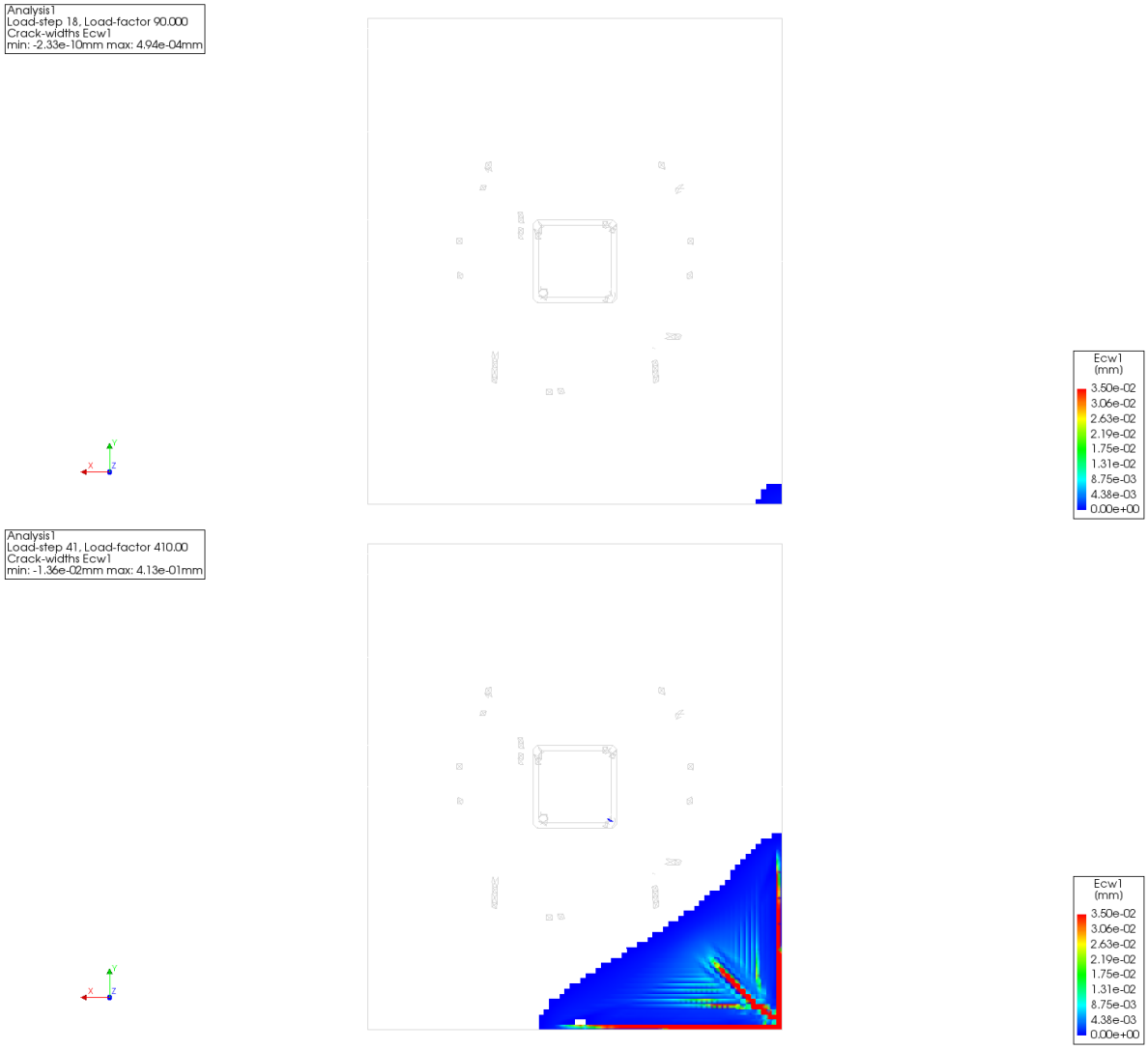

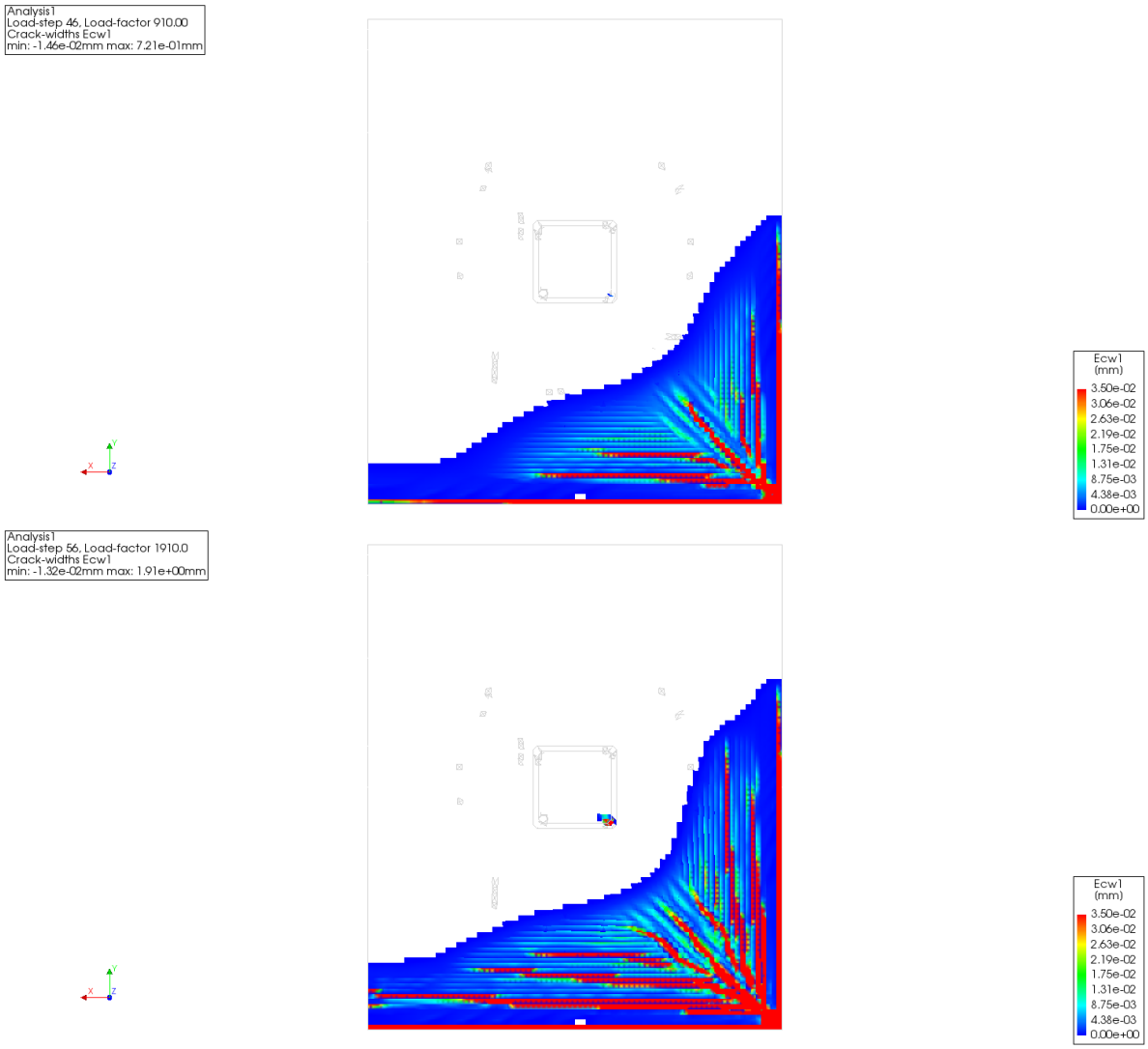

Figure A.7: *Crack development of slab subjected to point load (bottom surface)*

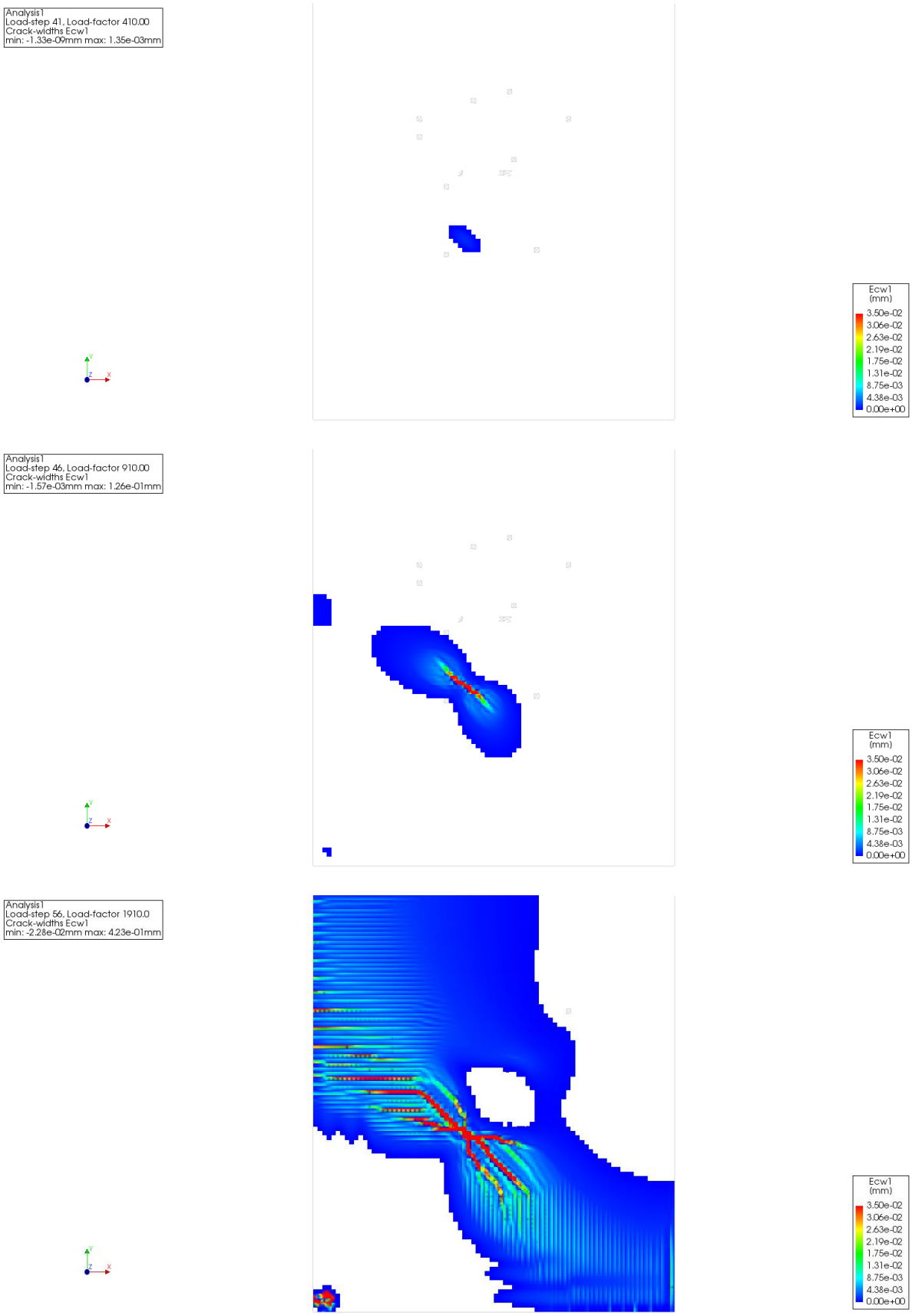

Figure A.8: *Crack development of slab subjected to point load (top surface)*

Appendix B Hand Calculation of Post-cracking Capacity

B.1 Hand calculation of post-cracking capacity of round panel

In order to calculate the post-cracking capacity of the studied round panel, the moment capacity must be evaluated. In this master's thesis, a simplified model based on the rigid-plastic model, according to (fib, 2013) was used to evaluate the moment capacity of the round panel.
By considering the geometry of the studied round panel, the radius is1025 mm (centre of the continuous support) and the height is 200 mm. As described in 2.5.3.3, the post-cracking strength can be evaluated by dividing $f_{R3} = 5.88$ MPa by 3. This results in having $f_{FTu} = 1.96$ MPa
The moment capacity can be evaluated by applying equation (2.5.6), which results in having $M_{p,RP} = 40.21$ kN. m.

By applying equation (2.6.7) the post-cracking capacity can be evaluated, where $a = 150$ mm.

$$P_{ult.RP} = \frac{2\pi\, M_{p,RP}}{1 - \frac{2a}{3R}} = 279.82 \text{ kN}$$

B.2 Hand calculation of capacity of slab subjected to uniformly distributed load

By the same approach for the round panel, the moment capacity can be evaluated:

$$M^{+}_{Py,SD} = M^{-}_{Py,SD} = M^{+}_{Px,SD} = M^{-}_{Px,SD} = \frac{f_{FTu}\, b\, h^2}{2}$$

First, it has been assumed that the fibres are uniformly distributed in the concrete matrix; thus, all moment capacities are equivalent. Second, one strip of one-meter width has been considered, which leads to $b = 1000$ mm. Third, the thickness of the slab has been considered to be $h = 230$ mm, which means neglecting the effect of the drop panel.

$$M^{+}_{Py,SD} = M^{-}_{Py,SD} = M^{+}_{Px,SD} = M^{-}_{Px,SD} = 51.88 \text{ kN. m}$$

By assuming that the location of the yield line is at the outside edge of the drop panel and applying the equations (2.7.13), (2.7.14), (2.7.15) and (2.7.16), the post cracking capacity can be evaluated as follows:

$$\phi_{h,SD} = \frac{M^{-}_{Px,SD}}{M^{+}_{Px,SD}} = \frac{M^{-}_{Py,SD}}{M^{+}_{Py,SD}} = 1$$

$$L_{rx} = 4000 - 400 = 3600 \text{ mm}$$

$$L_{ry} = 4700 - 400 = 4300 \text{ mm}$$

$$q_{ult,SD} = \frac{M^{+}_{Py,SD}\, 8(1+\phi_{h,SD})}{L^2_{rx}} = 64.05 \text{ kN}$$

$$q_{ult,SD} = \frac{M^{+}_{Px,SD}\, 8\left(1+\phi_{h,SD}\right)}{L^{2}_{ry}} = \ 44.89 \text{ kN} \qquad \text{(Governing)}$$

B.3 Hand calculation of capacity of slab subjected to point load

The moment capacity is dependent on the material and the section geometry, therefore it has been calculated with the same approach as B.2.

$M^{+}_{P,SP} = M^{-}_{P,SP} = 51.88 \text{ kN. m}$

By assuming that the radius of fan pattern is 4 m and applying equation (2.7.21), the post-cracking capacity can be evaluated as follows:

$\phi_{h,SP} = \ M^{-}_{P,SP} / M^{+}_{P,SP} = 1$

$a_{SP} = 150 \text{ mm}$

$R_{SP} = 4000 \text{ mm}$

$$P_{ult,SP} = \frac{M^{+}_{P,SP}\, 2\pi \left(1 + \phi_{h,SP}\right)}{\left(1 - \frac{2}{3}\, \frac{a_{SP}}{R_{SP}}\right)} = 668.7 \text{ kN}$$

Appendix C Numerical Models

The purpose of appending the codes of the numerical models is only to show how the material has been assigned as well as the implementation of non-linear analysis. Since the number of elements is enormous, several sections of the codes have been truncated. Hence, the appended codes cannot be used to analyse the models directly.

C.1 Notched beam model

Model Text File (.dat)

```
'UNITS'
LENGTH MM
FORCE N
ANGLE RAD
'DIRECTIONS'
  1   1.00000E+00   0.00000E+00   0.00000E+00
  2   0.00000E+00   1.00000E+00   0.00000E+00
  3   0.00000E+00   0.00000E+00   1.00000E+00
'MODEL'
DIMENS "2D"
GRAVDI 2
GRAVAC  -9.81000E+03
'COORDINATES'
  1   5.25000E+02  -3.07761E-14   0.00000E+00
  :
  (rows deleted)
  :
3520   2.75000E+02   1.46873E+02   0.00000E+00
'MATERI'
  1 NAME   "Supports Material" (Material of steel supports and loading plate)
    MCNAME MCSTEL
    MATMDL ISOTRO
    YOUNG    2.10000E+05 (Young's modulus of steel plates)
    POISON   1.50000E-01 (Poisson's ratio of steel plates)
    ASPECT
 10 NAME   "SFRC_MIX"
    MCNAME CONCR
    MATMDL TSCR
    YOUNG    3.55000E+04 (Young's modulus of SFRC mix)
    POISON   2.00000E-01 (Poisson's ratio of SFRC mix)
    DENSIT   2.38400E-09
    TOTCRK ROTATE (Total strain rotating crack model)
    TENCRV MULTLN
    POIRED NONE
    EPSIGT (Multilinear definition of the tensile behaviour)
          0.00000E+00   0.00000E+00   9.91549E-05   3.52000E+00
          5.04890E-03   2.05000E+00   7.73591E-03   1.65000E+00
          1.42413E-02   1.79000E+00   3.54545E-02   1.92000E+00
```

```
            8.49520E-02   2.02000E+00   1.41521E-01   2.10000E+00
            1.76876E-01   2.17000E+00   2.12231E-01   2.30000E+00
            3.53653E-01   1.80000E+00   7.07206E-01   1.40000E+00
            2.82853E+00   0.00000E+00
     COMCRV THOREN (Thorenfeldt material model)
     CNFCRV NONE
     COMSTR   4.91000E+01 (The compressive strength)
     LTHORE   3.00000E+02 (The scaling parameter)
     ASPECT
5 NAME   "Linear_Elasticity" (Material model for interface elements)
     MCNAME INTERF
     MATMDL ELASTI
     IFTYP  LIN2D
     DSNY     2.45500E+04 (Normal stiffness)
     DSSX     2.45500E+03 (Tangential stiffness)
     ASPECT
'GEOMET'
   2 NAME   "Notched_Beam"
     GCNAME SHEET
     GEOMDL MEMBRA
     THICK    1.50000E+02 (Thickness of beam in Z-direction)
   1 NAME   "Interface_Geometry"
     GCNAME LINE
     GEOMDL STLIIF
     CONFIG MEMBRA
     THICK    1.50000E+02 (Thickness of interface element in Z-direction)
'DATA'
   1 NAME   NL_SFRC
     INTEGR HIGH
     THINTE 11
'ELEMENTS'
SET  "Right_Support"
CONNECT
   1 Q8MEM  4 3 2 1
   2 Q8MEM  1 2 6 5
MATERIAL 1
GEOMETRY 2
SET  "Left_Support"
CONNECT
   3 Q8MEM  10 9 8 7
   4 Q8MEM  7 8 12 11
MATERIAL 1
GEOMETRY 2
SET  "Loading_Plate"
CONNECT
   5 Q8MEM  13 18 15 14
   6 Q8MEM  15 18 17 16
   7 T6MEM  18 13 17
MATERIAL 1
GEOMETRY 2
```

```
SET  "Notched_Beam"
CONNECT
   8 Q8MEM  400 464 463 399
   :
    (rows deleted)
   :
3362 Q8MEM  84 3520 20 19
3363 T6MEM  3520 84 37
MATERIAL 10
GEOMETRY 2
DATA 1
SET  "Interface_Left_Support"
CONNECT
3364 L8IF   26 27 7 10
3365 L8IF   25 26 11 7
MATERIAL 5
GEOMETRY 1
SET  "Interface_Right_Support"
CONNECT
3366 L8IF   23 24 1 4
3367 L8IF   22 23 5 1
MATERIAL 5
GEOMETRY 1
SET  "Interface_Loading_Plate"
CONNECT
3368 L8IF   20 21 15 14
3369 L8IF   19 20 16 15
MATERIAL 5
GEOMETRY 1
'LOADS'
CASE 1
NAME "Displacement_Load"
DEFORM
/ 13 17 / TR 2  -1.00000E-02
'SUPPOR'
NAME BC
/ 2 8 13 17 / TR 2
/ 13-18 / TR 1
'END'
```

Analysis Text File (.dcf)

```
*FILOS
 INITIA
*INPUT
*NONLIN LABEL="Structural_Nonlinear_Analysis_of_Notched_Beam"
  BEGIN EXECUT
    BEGIN LOAD
      LOADNR 1
      STEPS EXPLIC SIZES (Load step size with corresponding number of steps)
```

```
 0.100000(50) 0.500000(75) 1.00000(100) 5.00000(100) \
 10.0000(100) 50.0000(100) 75.0000(100) 100.000(1000)
   END LOAD
   BEGIN ITERAT
     MAXITE 150 (Number of iterations)
     METHOD NEWTON (Iterative method)
     LINESE OFF
     BEGIN CONVER
       DISPLA OFF
       ENERGY TOLCON 0.001 (Energy tolerance)
     END CONVER
   END ITERAT
  END EXECUT
*END
```

C.2 Round indeterminate panel model (3D)

Model Text File (.dat)

```
'UNITS'
LENGTH MM
FORCE N
ANGLE RAD
'DIRECTIONS'
  1   1.00000E+00   0.00000E+00   0.00000E+00
  2   0.00000E+00   1.00000E+00   0.00000E+00
  3   0.00000E+00   0.00000E+00   1.00000E+00
'MODEL'
DIMENS "3D"
GRAVDI 3
GRAVAC  -9.81000E+03
'COORDINATES'
  1   0.00000E+00   0.00000E+00   2.00000E+02
  :
  (rows deleted)
  :
110333   1.00008E+02   9.22719E+02   9.58997E+01
'MATERI'
  5 NAME   "Supports_Material" (The material of round support and loading plate)
    MCNAME MCSTEL
    MATMDL ISOTRO
    YOUNG    2.10000E+05
    POISON   1.50000E-01
    ASPECT
  2 NAME   "Interface_Round_Support_Material"
    MCNAME INTERF
    MATMDL FRICTI
    IFTYP  SUR3D
    DSNZ     6.58678E+03 (Normal stiffness)
    DSSX     6.58678E+02 (Tangential stiffness)
    DSSY     6.58678E+02 (Tangential stiffness)
    FRICTI
    COHESI   5.00000E-01 (Cohesive contact zone)
    OR
    COHESI   0.00000E+00 (Cohesionless contact zone)
    PHI      9.96687E-02 (Frictional contact zone with friction Coe. of 0.1)
    OR
    PHI      3.80506E-01 (Frictional contact zone with friction Coe. of 0.4)
    OR
    PHI      6.74741E-01 (Frictional contact zone with friction Coe. of 0.8)
    PSI      0.00000E+00
    ASPECT
  3 NAME   "Interface_Loading_Plate_Material"
    MCNAME INTERF
    MATMDL FRICTI
```

IFTYP SUR3D
DSNZ 6.58678E+03 **(Normal stiffness)**
DSSX 6.58678E+02 **(Tangential stiffness)**
DSSY 6.58678E+02 **(Tangential stiffness)**
FRICTI
COHESI 0.00000E+00
PHI 9.96687E-02 (**Friction Coe. (0.1) between round panel & loading plate)**
PSI 0.00000E+00
ASPECT
10 NAME "No_Tension" **(Material model for frictionless contact)**
MCNAME INTERF
MATMDL NONLIF
ASPECT
IFTYP SUR3D
DSNZ 6.58678E+03 **(Normal stiffness)**
DSSX 1.00000E-05 **(very low tangential stiffness)**
DSSY 1.00000E-05 **(very low tangential stiffness)**
IFNOTE NOTSHR **(Tension and reduction shear parameters)**
NOSHT2 0.00000E+00 0.00000E+00
NOSHTE 0.00000E+00 0.00000E+00
NOTENS 0.00000E+00 0.00000E+00
11 NAME "SFRC_Mix"
MCNAME CONCR
MATMDL TSCR
YOUNG 3.55000E+04
POISON 2.00000E-01
DENSIT 2.38400E-09
TOTCRK ROTATE
TENCRV MULTLN
POIRED NONE
EPSIGT **(Multilinear definition of the tensile behaviour)**
0.00000E+00 0.00000E+00 9.91549E-05 3.52000E+00
1.97726E-03 2.05000E+00 2.99680E-03 1.65000E+00
5.46517E-03 1.79000E+00 1.35142E-02 1.92000E+00
3.22952E-02 2.02000E+00 5.37593E-02 2.10000E+00
6.71743E-02 2.17000E+00 8.05894E-02 2.30000E+00
1.34249E-01 1.80000E+00 2.68400E-01 1.40000E+00
1.07330E+00 0.00000E+00
COMCRV THOREN
CNFCRV NONE
COMSTR 4.91000E+01
LTHORE 3.00000E+02
ASPECT
1 NAME "Symmetry_Material"
MCNAME CONCR
MATMDL TSCR
YOUNG 3.55000E+04
POISON 2.00000E-01
DENSIT 2.38400E-09
TOTCRK ROTATE

```
    TENCRV MULTLN
    POIRED NONE
    EPSIGT (Multilinear definition of the tensile behaviour)
                (It can be observed that the material is weaker, since the fracture
                 energy is half)
          0.00000E+00   0.00000E+00   9.91549E-05   3.52000E+00
          1.03821E-03   2.05000E+00   1.54798E-03   1.65000E+00
          2.78216E-03   1.79000E+00   6.80667E-03   1.92000E+00
          1.61972E-02   2.02000E+00   2.69292E-02   2.10000E+00
          3.36367E-02   2.17000E+00   4.03443E-02   2.30000E+00
          6.71743E-02   1.80000E+00   1.34249E-01   1.40000E+00
          5.36700E-01   0.00000E+00
    COMCRV THOREN (Thorenfeldt material model)
    CNFCRV NONE
    COMSTR   4.91000E+01(The compressive strength)
    LTHORE   3.00000E+02 (The scaling parameter)
    ASPECT
'GEOMET'
  1 NAME   "Round_Panel_Geometry"
    GCNAME SOLID
    GEOMDL STRSOL
  2 NAME   "Supports_Geometry"
    GCNAME SOLID
    GEOMDL STRSOL
  3 NAME   "Interface_R_S_Geometry"
    GCNAME SHEET
    GEOMDL STPLIF
    XAXIS    1.00000E+00   0.00000E+00   0.00000E+00
  4 NAME   "Interface_L_P_Geometry"
    GCNAME SHEET
    GEOMDL STPLIF
    XAXIS    1.00000E+00   0.00000E+00   0.00000E+00
'DATA'
  1 NAME   NL_SFRC
    INTEGR HIGH
'ELEMENTS'
SET  "Loading_Plate"
CONNECT
  1 CHX60  53 510 161 509 52 238 6 229 496 552 531 246 120 553 177 554 113 530 51 475
  :
  (rows deleted)
  :
188 CTE30  206 669 200 779 218 778 786 793 796 172
MATERIAL 5
GEOMETRY 2
SET  "Round_Support"
CONNECT
189 CHX60  842 2028 838 2029 931 2038 1254 2037 2027 1864 2043 2947 1251 2528 1012
2044 1255 2948 1517 2949
:
```

(rows deleted)
:
736 CTE30 1512 3647 1448 2834 1156 3509 3510 3502 3373 1514
MATERIAL 5
GEOMETRY 2
SET "Round_Panel"
CONNECT
 742 CHX60 7104 36960 7275 36959 7110 36352 7106 35393 42998 43010 43001 42995
:
(rows deleted)
:
27494 CTE30 29277 108030 10039 94488 27538 108031 108267 106504 110293 10075
MATERIAL 11
GEOMETRY 1
DATA 1
SET "Interface_Loading_Plate"
CONNECT
27495 CQ48I 3932 39096 3933 39097 3934 39098 3935 39099 71 284 69 283 86 286 88 285
:
(rows deleted)
:
27550 CT36I 3963 39152 3937 39190 3964 39144 74 340 73 377 72 330
MATERIAL 3
GEOMETRY 4
SET "Interface_Round_Support"
CONNECT
27551 CQ48I 3665 30431 3664 40190 3845 40191 3846 40192 922 1938 923 2607 1498
2609 1499 2608
:
(rows deleted)
:
27724 CT36I 3916 40446 3930 40445 3931 40447 1477 2863 1420 2862 1482 2865
MATERIAL 2 (Frictional Contact Zone)
OR
MATERIAL 10 (Frictionless Contact Zone)
GEOMETRY 3
SET "Symmetry_Elements"
CONNECT
 737 CHX60 4076 30587 3974 30731 4173 35392 7106 36148 40189 30275 42943 42995
4738 40137 4262 42838 9958 42996 10081 42997
:
(rows deleted)
:
26662 CTE30 4688 49132 12080 104693 12741 107294 106331 106334 109002 29905
MATERIAL 1
GEOMETRY 1
DATA 1
'LOADS'
CASE 1
NAME "Displacement_Load"

DEFORM **(Prescribed deformation)**
/ 2 ... (numbers deleted) ... 414-507 / TR 3 -1.00000E-01
'SUPPOR'
NAME BC
/ 1-3 ... (numbers deleted) ... 39193-40189 / TR 1
/ 1-3 ... (numbers deleted) ... 39193-40189 / RO 2
/ 1-15 ... (numbers deleted) ... 41998-42994 / RO 3
/ 2 ... (numbers deleted) ... 1947-2027 / TR 3
/ 1 4-13 ... (numbers deleted) ... 41998-42994 / TR 2
/ 1 4-13 ... (numbers deleted) ... 41998-42994 / RO 1
'END'

Analysis Text File (.dcf)

```
*FILOS
 INITIA
*INPUT
*NONLIN LABEL=" Structural_Nonlinear_Analysis_of_Round_Panel_3D "
  BEGIN EXECUT
    LOAD STEPS EXPLIC SIZES 1.00000(30) 10.0000(400)
    BEGIN ITERAT
      MAXITE 300 (Number of iterations)
      METHOD NEWTON (Iterative method)
      BEGIN CONVER
        DISPLA OFF
        ENERGY
      END CONVER
    END ITERAT
  END EXECUT
*END
```

C.3 Pile-supported slab subjected to uniformly distributed load

Model Text File (.dat)

```
'UNITS'
LENGTH MM
FORCE N
ANGLE RAD
'DIRECTIONS'
  1   1.00000E+00   0.00000E+00   0.00000E+00
  2   0.00000E+00   1.00000E+00   0.00000E+00
  3   0.00000E+00   0.00000E+00   1.00000E+00
'MODEL'
DIMENS "3D"
GRAVDI 3
GRAVAC  -9.81000E+03
'COORDINATES'
  1   4.35000E+03   4.38536E+03  -4.56579E-12
  :
  (rows deleted)
  :
180691   4.77090E+03   3.88802E+03   1.72470E+02
'MATERI'
2 NAME   "Pile_Material" (concrete of pile)
    MCNAME CONCR
    MATMDL LEI
    YOUNG    3.52200E+04 (Young's modulus of pile concrete)
    POISON   2.00000E-01 (Poisson's ratio of pile concrete)
    ASPECT
  3 NAME   "Interface_Pile_Floor_Material" (Material of interface elements
                                            between pile and floor)
    MCNAME INTERF
    MATMDL FRICEL
    IFTYP  SUR3D
    DSNZ     7.38227E+02 (Normal stiffness)
    DSSX     7.38227E+01 (Tangential stiffness)
    DSSY     7.38227E+01 (Tangential stiffness)
    FRICEL
    PHI      3.06654E-01 (Friction coefficient)
    COHESI   1.83000E-03 (Cohesion)
    ASPECT
  1 NAME   "SFRC_Mix"
    MCNAME CONCR
    MATMDL TSCR
    YOUNG    3.55000E+04
    POISON   2.00000E-01
    TOTCRK ROTATE
    TENCRV MULTLN
    POIRED NONE
    EPSIGT (Multilinear definition of the tensile behaviour)
```

```
          0.00000E+00   0.00000E+00   9.91549E-05   3.52000E+00
            8.29866E-04   2.05000E+00   1.22654E-03   1.65000E+00
            2.18690E-03   1.79000E+00   5.31852E-03   1.92000E+00
            1.26256E-02   2.02000E+00   2.09766E-02   2.10000E+00
            2.61960E-02   2.17000E+00   3.14154E-02   2.30000E+00
            5.22928E-02   1.80000E+00   1.04486E-01   1.40000E+00
            4.17649E-01   0.00000E+00
    COMCRV THOREN
    CNFCRV NONE
    COMSTR   4.91000E+01
    LTHORE   3.00000E+02
    ASPECT
  4 NAME   "Symmetry_Material"
    MCNAME CONCR
    MATMDL TSCR
    YOUNG    3.55000E+04
    POISON   2.00000E-01
    TOTCRK ROTATE
    TENCRV MULTLN
    POIRED NONE
    EPSIGT (Multilinear definition of the tensile behaviour for symmetry
            elements)
          0.00000E+00   0.00000E+00   9.91549E-05   3.52000E+00
          4.64511E-04   2.05000E+00   6.62847E-04   1.65000E+00
          1.14303E-03   1.79000E+00   2.70884E-03   1.92000E+00
          6.36240E-03   2.02000E+00   1.05379E-02   2.10000E+00
          1.31476E-02   2.17000E+00   1.57573E-02   2.30000E+00
          2.61960E-02   1.80000E+00   5.22928E-02   1.40000E+00
          2.08874E-01   0.00000E+00
    COMCRV THOREN
    CNFCRV NONE
    COMSTR   4.91000E+01
    LTHORE   3.00000E+02
    ASPECT
'GEOMET'
  1 NAME   "Floor_Geometry"
    GCNAME SOLID
    GEOMDL STRSOL
  2 NAME   "Piles-Geometry"
    GCNAME SOLID
    GEOMDL STRSOL
  3 NAME   "Interface_Geometry"
    GCNAME SHEET
    GEOMDL STPLIF
'DATA'
  1 NAME   "NL_Floor_SFRC"
    INTEGR HIGH
'ELEMENTS'
SET  "Pile"
CONNECT
```

```
1 CHX60  72 1256 409 1412 407 1217 71 564 654 1513 1514 655 59 1037 186 833
  :
  (rows deleted)
  :
225 CTP45  12 525 11 1388 394 1467 527 526 1658 7 521 3 1051 199 966
MATERIAL 2
GEOMETRY 2
SET  "Floor"
CONNECT
 251 CHX60  3015 50579 3180 50578 3016 50118 3014 50384 81763 81814 81766 81740
18914 81815 18931 81816 18915 81768 18906 81765
:
(rows deleted)
:
39829 CTE30 18566 177992 41974 175767 46576 178243 179936 180668 180667 18516
MATERIAL 1
GEOMETRY 1
DATA 1
SET  "Pile_Interface"
CONNECT
39830 CQ48I 1766 79682 1767 79683 1768 79684 1769 79685 144 662 142 661 116 664
118 663
:
(rows deleted)
:
40054 CT36I 1713 48633 1715 80057 1960 80068 2 530 6 1035 174 1048
MATERIAL 3
GEOMETRY 3
SET  "Symmetry_Elements"
CONNECT
 226 CHX60  18102 80182 2795 48847 1972 48713 1995 80183 81739 50117 48545 81658
18906 81740 3014 50116 2711 81737 18101 81741
:
(rows deleted)
:
13969 CHX60 18288 80600 18287 80599 18283 80591 18284 80601 121785 121772
121744
          121768 32061 121788 32058 121774 32050 121771 32057 121789
MATERIAL 4
GEOMETRY 1
DATA 1
'LOADS'
CASE 1
NAME " Uniformly_Distributed_Load "
ELEMEN
/ 226 ... (numbers deleted) ...8920 /
    FACE   KSI2
    FORCE   -5.07875E-02
    DIRECT 3
/ 252 ... (numbers deleted) ...6739 /
```

```
    FACE   ETA1
    FORCE   -5.07875E-02
    DIRECT 3
/ 234... (numbers deleted) ... 13761 /
    FACE   ZETA1
    FORCE   -5.07875E-02
    DIRECT 3
/ 227... (numbers deleted) ... 8921 /
    FACE   KSI2
    FORCE   -5.07875E-02
    DIRECT 3
/ 232 ... (numbers deleted) ... 8991 /
    FACE   ETA1
    FORCE   -5.07875E-02
    DIRECT 3
/ 253... (numbers deleted) ...  -13764 /
    FACE   ZETA1
    FORCE   -5.07875E-02
    DIRECT 3
COMBIN
  1 1   1.00000E+00
'SUPPOR'
NAME BC
/ 1-1708... (numbers deleted) ... 80182-81022 / TR 1
/ 1-1708... (numbers deleted) ... 81023-81737 / TR 2
/ 1-1708 / TR 3
/ 1-1708 ... (numbers deleted) ...80182-81737 / RO 3
/ 1969-1977 ... (numbers deleted) ... 80182-81022 / RO 2
/ 1969 ... (numbers deleted) ... 81023-81737 / RO 1
'END'
```

Analysis Text File (.dcf)

```
*FILOS
 INITIA
*INPUT
*NONLIN LABEL="Structural_Nonlinear_Analysis_of_Slab_Dist_Load"
  BEGIN EXECUT
    BEGIN LOAD
      LOADNR 1
      STEPS EXPLIC SIZES 0.0100000(100) 0.0500000(250)
    END LOAD
    BEGIN ITERAT
      MAXITE 500 (Number of iterations)
      METHOD NEWTON (Iterative method)
      BEGIN CONVER
        DISPLA OFF
        ENERGY
      END CONVER
    END ITERAT
```

```
  END EXECUT
*END
```

C.4 Pile-supported slab subjected to point load

Model Text File (.dat)

```
'UNITS'
LENGTH MM
FORCE N
ANGLE RAD
'DIRECTIONS'
  1   1.00000E+00   0.00000E+00   0.00000E+00
  2   0.00000E+00   1.00000E+00   0.00000E+00
  3   0.00000E+00   0.00000E+00   1.00000E+00
'MODEL'
DIMENS "3D"
GRAVDI 3
GRAVAC  -9.81000E+03
'COORDINATES'
  1   2.15000E+03   2.35000E+03   3.30000E+02
  :
  (rows deleted)
  :
180571   4.83208E+03   5.59986E+03   1.43611E+02
'MATERI'
  2 NAME   "Pile_Material"
    MCNAME CONCR
    MATMDL LEI
    YOUNG    3.52200E+04
    POISON   2.00000E-01
    ASPECT
  3 NAME   "Interface_Pile_Floor_Material" (Material of interface elements
                                            between pile and floor)
    MCNAME INTERF
    MATMDL FRICEL
    IFTYP  SUR3D
    DSNZ     7.37419E+02
    DSSX     7.37419E+01
    DSSY     7.37419E+01
    FRICEL
    PHI      3.06654E-01
    COHESI   1.83000E-03
    ASPECT
  1 NAME   "SFRC_Mix"
    MCNAME CONCR
    MATMDL TSCR
    YOUNG    3.55000E+04
    POISON   2.00000E-01
    DENSIT   2.38400E-09
    TOTCRK ROTATE
    TENCRV MULTLN
    POIRED NONE
```

```
  EPSIGT (Multilinear definition of the tensile behaviour)
        0.00000E+00   0.00000E+00   9.91549E-05   3.52000E+00
        8.29066E-04   2.05000E+00   1.22530E-03   1.65000E+00
        2.18461E-03   1.79000E+00   5.31281E-03   1.92000E+00
        1.26119E-02   2.02000E+00   2.09538E-02   2.10000E+00
        2.61674E-02   2.17000E+00   3.13811E-02   2.30000E+00
        5.22357E-02   1.80000E+00   1.04372E-01   1.40000E+00
        4.17191E-01   0.00000E+00
  COMCRV THOREN
  CNFCRV NONE
  COMSTR   4.91000E+01
  LTHORE   3.00000E+02
  ASPECT
 4 NAME   "Interface_Point_load" (Material of interface elements between floor
                                  and loading plate)
  MCNAME INTERF
  MATMDL FRICEL
  IFTYP  SUR3D
  DSNZ     7.37419E+02
  DSSX     7.37419E+01
  DSSY     7.37419E+01
  FRICEL
  COHESI   0.00000E+00
  PHI      9.96687E-02
  ASPECT
 5 NAME   "Steel" (Loading plate material)
  MCNAME MCSTEL
  MATMDL ISOTRO
  YOUNG    2.10000E+05
  POISON   1.50000E-01
  ASPECT
 6 NAME   "Symmetry_Elements_Material"
  MCNAME CONCR
  MATMDL TSCR
  YOUNG    3.55000E+04
  POISON   2.00000E-01
  DENSIT   2.38400E-09
  TOTCRK ROTATE
  TENCRV MULTLN
  POIRED NONE
  EPSIGT (Multilinear definition of the tensile behaviour for symmetry
          elements)
        0.00000E+00   0.00000E+00   9.91549E-05   3.52000E+00
        4.64110E-04   2.05000E+00   6.62229E-04   1.65000E+00
        1.14189E-03   1.79000E+00   2.70598E-03   1.92000E+00
        6.35553E-03   2.02000E+00   1.05265E-02   2.10000E+00
        1.31333E-02   2.17000E+00   1.57401E-02   2.30000E+00
        2.61674E-02   1.80000E+00   5.22357E-02   1.40000E+00
        2.08645E-01   0.00000E+00
  COMCRV THOREN
```

```
    CNFCRV NONE
    COMSTR   4.91000E+01
    LTHORE   3.00000E+02
    ASPECT
'GEOMET'
  1 NAME   "Floor_Geometry"
    GCNAME SOLID
    GEOMDL STRSOL
  2 NAME   "Piles-Geometry"
    GCNAME SOLID
    GEOMDL STRSOL
  3 NAME   "Interface_Geometry"
    GCNAME SHEET
    GEOMDL STPLIF
  4 NAME   "Steel"
    GCNAME SOLID
    GEOMDL STRSOL
'DATA'
  1 NAME   "NL_Floor_SFRC"
    INTEGR HIGH
'ELEMENTS'
SET  "Pile"
CONNECT
  1 CHX60  168 1352 505 1508 503 1313 167 660 750 1609 1610 751 155 1133 282 929
284 824 156 634
  :
  (rows deleted)
  :
225 CTP45  108 621 107 1484 490 1563 623 622 1754 103 617 99 1147 295 1062
MATERIAL 2
GEOMETRY 2
SET  "Floor"
CONNECT
 251 CHX60  1874 66995 1876 66996 1877 66997 1875 66991 81881 81834 81807 81831
18942 81882 18926 81835 18917 81832 18925 81883
:
(rows deleted)
:
39699 CTE30 18783 179519 47978 170016 47979 179517 179797 180554 179529 44897
MATERIAL 1
GEOMETRY 1
DATA 1
SET  "Point_Load"
CONNECT
39700 CHX60 29 81 21 38 6 43 20 82 93 65 47 64 25 69 13 51 2 50 12 70
:
(rows deleted)
:
39708 CHX60 8 37 24 92 32 90 17 44 60 68 96 61 4 56 16 80 28 78 9 57
MATERIAL 5
```

```
GEOMETRY 4
SET  "Point_Load_Interface"
CONNECT
39709 CQ48I 6 38 21 81 29 82 20 43 1814 48583 1819 66989 1874 66990 1820 48578
:
(rows deleted)
:
39717 CQ48I 32 92 24 37 8 44 17 90 1877 67000 1870 48535 1817 48824 1873 66998
MATERIAL 4
GEOMETRY 3
SET  "Pile_Interface"
CONNECT
39718 CQ48I 1878 79737 1879 79738 1880 79739 1881 79740 240 758 238 757 212 760
214 759
:
(rows deleted)
:
39942 CT36I 1809 48610 1811 80112 2072 80123 98 626 102 1131 270 1144
MATERIAL 3
GEOMETRY 3
SET  "Symmetry_Elements"
CONNECT
226 CHX60  18198 80237 1873 48824 1817 48690 2127 80238 81806 66998 48535 81713
18917 81807 1877 67000 1870 81792 18197 81808
:
(rows deleted)
:
13969 CHX60 17418 78644 17417 78643 17324 78457 17325 78645 121843 121821
121832 121855 32070 121846 32064 121835 32067 121859 32073 121858
MATERIAL 6
GEOMETRY 1
DATA 1
'LOADS'
CASE 1
NAME P_L
DEFORM
/ 1-4 9-16 25-28 48-59 69-80 / TR 3  -1.00000E-02
COMBIN
   1 1   1.00000E+00
'SUPPOR'
NAME BC
/ 3 ... (numbers deleted) ... 80237-81077 / TR 1
/ 1 ... (numbers deleted) ... 97-1804 / TR 3
/ 1 ... (numbers deleted) ...80237-81792 / RO 3
/ 3 ... (numbers deleted) ...80237-81077 / RO 2
/ 1 ... (numbers deleted) ...81078-81792 / RO 1
'END'
```

Analysis Text File (.dcf)

```
*FILOS
 INITIA
*INPUT
*NONLIN LABEL="Structural_Nonlinear_Analysis_of_Slab_Point_Load "
  BEGIN EXECUT
    BEGIN LOAD
      LOADNR 1
      STEPS EXPLIC SIZES 1.00000(10) 10.0000(30) 100.000(500)
    END LOAD
    BEGIN ITERAT
      MAXITE 500 (Number of iterations)
      METHOD NEWTON (Iterative method)
      BEGIN CONVER
        DISPLA OFF
        ENERGY
      END CONVER
    END ITERAT
  END EXECUT
*END
```